

University of California
Santa Barbara

Heterogeneous Integration of Mid-infrared Lasers on Silicon

A dissertation submitted in partial satisfaction
of the requirements for the degree

Doctor of Philosophy
in
Electrical and Computer Engineering

by

Alexander Weber Spott

Committee in charge:

Professor John Bowers, Chair
Professor Larry Coldren
Dr. Jerry Meyer
Professor Jon Schuller

June 2018

The Dissertation of Alexander Weber Spott is approved.

Professor Larry Coldren

Dr. Jerry Meyer

Professor Jon Schuller

Professor John Bowers, Committee Chair

May 2018

Heterogeneous Integration of Mid-infrared Lasers on Silicon

Copyright © 2018

by

Alexander Weber Spott

To Mom, Dad, Andrew, and Alex

Acknowledgements

This dissertation was formed at the intersection of several specialized fields of research. None of this work would have been possible without leveraging the relative expertise from experts in each of these areas. I feel very fortunate to be at the center of such a collaboration where I have had the opportunity to work with so many impressive scientists and engineers.

I first need to thank Professor John Bowers. It is difficult to fully acknowledge John in just a few sentences. I would not have been able to pursue these projects without the seemingly limitless resources and opportunities that John has made available to me. I truly appreciate the combination of guidance and autonomy he has provided. I could not have hoped to find myself in a better environment for graduate school.

I would also like to thank the rest of my committee. Dr. Jerry Meyer has been a great mentor and a direct connection to the mid-infrared semiconductor laser community. I've enjoyed running ideas back and forth with him over the years. I owe Professor Larry Coldren for teaching me the foundation of everything I know about lasers. Professor Jon Schuller taught me to look closely at the interesting physics happening at the intersection of light and matter.

I would like to thank Dr. Michael Davenport for humoring my constant stream of questions for the first four years or so of my PhD. I can only imagine how many extra fabrication runs my projects would have taken if Mike hadn't already solved so many of the biggest processing challenges. Somehow every conversation with Mike was educational, especially the ones which had nothing to do with research.

Eric Stanton worked alongside me on this project and has been a fantastic office-mate and colleague. Beginning with our screening exam study sessions, technical discussions with Eric always helped consolidate my understanding.

I could write another several pages on all of the great experiences I've had with the rest of the Bowers Group. Thank you Tin for all of the interesting discussions, Jock for all of the support in the first few years of my PhD, and Alan for wandering around Japan with me in search of bao and toro. I have learned something from and enjoyed spending time with each of the rest of you: Chong, Jared, Jared, Minh, Lin, Tony, Nick, Molly, Tin, Martijn, Paulo, Aditya, Warren, Akhilesh, Justin, Jenny, Andy, Robert, Chao, Jinxi, Kaiyan, Emmett, Sudha, Geza, Aditya, Andreas, Weiqiang, Daewhan, Chen, Yating, Valerio, Songtao, Roger, MJ. The group admins, Ceanna and Tina, both saved me a tremendous amount of time and somehow repeatedly kept me from missing paperwork deadlines.

The team at the US Naval Research Lab has been like a second lab group to me. Dr. Igor Vurgaftman provided extraordinary technical expertise on ICLs. William Bewley, Charles Merritt, Chadwick Canedy, Mijin Kim, and Chul Soo Kim have not only each contributed their own expertise to my projects, but performed a share of the work themselves, growing the ICL laser material and performing laser measurements.

I also appreciate the support from our collaborators at the University of Wisconsin: Dan Botez, Luke Mawst, and Jeremy Kirch. Professor Botez repeatedly gave me extremely complicated answers to what I thought were simple questions about QCLs.

Much of the processing in this thesis was done by Jon Peters. Jon's impressive efficiency and dedication in the cleanroom is the only reason it was possible to complete more than one of these process runs during my PhD. Alfredo Torres did some of the more difficult process development for the ICL fabrication.

The Nanofab staff are fundamental to any fabrication-heavy thesis. Thank you Tom, Brian, Aidan, Don, Demis, Tony, Mike, Mike, Luis, Ning, Biljana, Bill, and Brian. Tom Reynolds has also been a mentor for both technical and non-technical advice over the years.

I began my silicon photonics research career at the University of Washington in Seattle under the guidance of Drs. Michael Hochberg and Tom Baehr-Jones. I appreciate the opportunities, mentorship, and experiences they gave me at such an early stage in my career.

And of course my parent's support got me here in the first place. Thank you for helping me make the right career decisions and putting up with me through so many years of school. My brother, Dr. Andrew Spott, has perhaps had the largest impact on my career throughout my life. Andrew has encouraged me during every part of my education and pushed me to get involved in physics and research during my undergraduate studies. Both Andrew and his fiancée Alejandra helped keep me somewhat sane during my PhD.

And finally, I somehow managed to meet my amazing girlfriend Alex in the middle of all of this. Alex has been an incredible support and has put up with more discussion of lasers than she ever thought was possible (or reasonable). She is an inspiration to me as an eloquent scientist and teacher herself, and is the reason some of my slides and figures look nice.

Curriculum Vitæ

Alexander Weber Spott

Education

- 2018 Ph.D. in Electrical and Computer Engineering, University of California, Santa Barbara.
- 2015 M.S. in Electrical and Computer Engineering, University of California, Santa Barbara.
- 2011 B.S. in Physics, Minor in Mathematics, University of Washington, Seattle.

Patents

1. I. Vurgaftman, J. R. Meyer, M. J. Heck, J. Bovington, **A. Spott**, and E. J. Stanton, “Ultra-Broadband Photonic Integrated Circuit Platform and Ultra-Broadband Photonic Integrated Circuit,” Patent No.: US 9,612,398 B2, filed Oct. 17, 2014, allowed Jan. 30, 2017, issued Apr. 4, 2017.

Journal Publications

1. E. J. Stanton, **A. Spott**, J. Peters, M. L. Davenport, A. Malik, N. Volet, J. Liu, C. D. Merritt, W. W. Bewley, I. Vurgaftman, C. S. Kim, J. R. Meyer, and J. E. Bowers, “Multi-spectral quantum cascade lasers on silicon with integrated multiplexers,” *APL Photonics* **In Review** (2018).
2. **A. Spott**, E. J. Stanton, A. Torres, M. Davenport, C. L. Canedy, I. Vurgaftman, M. Kim, C. S. Kim, C. D. Merritt, W. W. Bewley, J. R. Meyer, and J. E. Bowers, “Interband Cascade Lasers on Silicon,” *Optica* **In Review** (2018).
3. A. Malik, E. J. Stanton, J. Liu, **A. Spott**, and J. E. Bowers, “High Performance 7×8 Ge-on-Si Arrayed Waveguide Gratings for the Midinfrared,” *IEEE Journal of Selected Topics in Quantum Electronics* **24**, 1–8 (2018).
4. **A. Spott**, E. J. Stanton, N. Volet, J. D. Peters, J. R. Meyer, and J. E. Bowers, “Heterogeneous Integration for Mid-infrared Silicon Photonics,” *IEEE Journal of Selected Topics in Quantum Electronics* **23**, 1–10 (2017).
5. N. Volet, **A. Spott**, E. J. Stanton, M. L. Davenport, L. Chang, J. D. Peters, T. C. Briles, I. Vurgaftman, J. R. Meyer, and J. E. Bowers, “Semiconductor optical amplifiers at 2.0- μ m wavelength on silicon,” *Laser & Photonics Reviews* **11**, 1600165 (2017).
6. E. J. Stanton, **A. Spott**, M. L. Davenport, N. Volet, and J. E. Bowers, “Low-loss arrayed waveguide grating at 760nm,” *Optics Letters* **41**, 1785–1788 (2016).

7. T. Komljenovic, M. L. Davenport, J. Hulme, A. Y. Liu, C. T. Santis, **A. Spott**, S. Srinivasan, E. J. Stanton, C. Zhang, and J. E. Bowers, “Heterogeneous Silicon Photonic Integrated Circuits,” *Journal of Lightwave Technology* **34**, 20–35 (2015).
8. **A. Spott**, J. Peters, M. L. Davenport, E. J. Stanton, C. Zhang, C. Merritt, W. Bewley, I. Vurgaftman, C. S. Kim, J. R. Meyer, J. Kirch, L. Mawst, D. Botez, and J. Bowers, “Heterogeneously Integrated Distributed Feedback Quantum Cascade Lasers on Silicon,” *Photonics* **3**, 35 (2016).
9. **A. Spott**, J. Peters, M. L. Davenport, E. J. Stanton, C. D. Merritt, W. W. Bewley, I. Vurgaftman, C. S. Kim, J. R. Meyer, J. Kirch, L. J. Mawst, D. Botez, and J. E. Bowers, “Quantum cascade laser on silicon,” *Optica* **3**, 545–551 (2016).
10. E. J. Stanton, M. J. R. Heck, J. Bovington, **A. Spott**, and J. E. Bowers, “Multi-octave spectral beam combiner on ultra-broadband photonic integrated circuit platform,” *Optics Express* **23**, 11272–11283 (2015).
11. **A. Spott**, M. L. Davenport, J. Peters, J. Bovington, M. J. R. Heck, E. J. Stanton, I. Vurgaftman, J. R. Meyer, and J. Bowers, “Heterogeneously integrated 2.0 μm CW hybrid silicon lasers at room temperature,” *Optics Letters* **40**, 1480–1483 (2015).
12. **A. Spott**, T. Baehr-Jones, R. Ding, Y. Liu, R. Bojko, T. O’Malley, A. Pomerene, C. Hill, W. Reinhardt, and M. Hochberg, “Photolithographically fabricated low-loss asymmetric silicon slot waveguides,” *Optics Express* **19**, 10950–10958 (2011).
13. R. Ding, T. Baehr-Jones, W.-J. Kim, B. Boyko, R. Bojko, **A. Spott**, A. Pomerene, C. Hill, W. Reinhardt, and M. Hochberg, “Low-loss asymmetric strip-loaded slot waveguides in silicon-on-insulator,” *Applied physics letters* **98**, 233303 (2011).
14. R. Ding, T. Baehr-Jones, W.-J. Kim, **A. Spott**, M. Fournier, J.-M. Fedeli, S. Huang, J. Luo, A. K. Y. Jen, L. Dalton, and M. Hochberg, “Sub-Volt Silicon-Organic Electro-optic Modulator With 500 MHz Bandwidth,” *Journal of Lightwave Technology* **29**, 1112–1117 (2011).
15. **A. Spott**, Y. Liu, T. Baehr-Jones, R. Ilic, and M. Hochberg, “Silicon waveguides and ring resonators at 5.5 μm ,” *Applied physics letters* **97**, 213501 (2010).
16. T. Baehr-Jones, **A. Spott**, R. Ilic, A. Spott, B. Penkov, W. Asher, and M. Hochberg, “Silicon-on-sapphire integrated waveguides for the mid-infrared,” *Optics Express* **18**, 12127–12135 (2010).

Conference Publications

1. E. J. Stanton, **A. Spott**, J. D. Peters, M. L. Davenport, N. Volet, A. Malik, J. Liu, C. D. Merritt, W. W. Bewley, I. Vurgaftman, C. S. Kim, J. R. Meyer, and J. E. Bowers, “Quantum cascade multi-spectral laser with integrated beam combiner on silicon,” in *Conference on Lasers and Electro-Optics (CLEO)*, STh1B.7 (2018).
2. A. Malik, E. J. Stanton, J. Liu, **A. Spott**, and J. E. Bowers, “Ge-on-Si wavelength division multiplexing components near 4.7 μm ,” in *Conference on Lasers and Electro-Optics (CLEO)*, JW2A.39 (2018).

3. C. C. Evans, **A. Spott**, C. D. Merritt, W. W. Bewley, I. Vurgaftman, C. S. Kim, J. R. Meyer, J. M. Hensley, J. E. Bowers, and M. B. Frish, “Gas Sensing Using Heterogeneously Integrated Quantum Cascade Lasers on Silicon,” in Conference on Lasers and Electro-Optics (CLEO), STu3N.1 (2018).
4. C. D. Merritt, W. W. Bewley, C. L. Canedy, C. S. Kim, I. Vurgaftman, J. R. Meyer, **A. Spott**, J. Peters, E. J. Stanton, M. L. Davenport, A. Torres, J. E. Bowers, J. D. Kirch, L. J. Mawst, and D. Botez, “Development of quantum and interband cascade lasers on silicon (Conference Presentation),” Proc. SPIE 10536, Smart Photonic and Optoelectronic Integrated Circuits XX, 1053606 (2018).
5. **A. Spott (post-deadline)**, E. J. Stanton, A. Torres, M. L. Davenport, C. L. Canedy, I. Vurgaftman, M. Kim, C. S. Kim, C. D. Merritt, W. W. Bewley, J. R. Meyer, and J. E. Bowers., “Interband cascade laser on silicon,” 2017 IEEE Photonics Conference (IPC) Part II, pp. 1–2 (2017).
6. **A. Spott (invited)**, J. Peters, M. L. Davenport, E. J. Stanton, C. Zhang, W. W. Bewley, C. D. Merritt, I. Vurgaftman, C. S. Kim, J. R. Meyer, J. Kirch, L. J. Mawst, D. Botez, and J. E. Bowers, “Quantum cascade lasers on silicon,” Proc. SPIE. 10123, Novel In-Plane Semiconductor Lasers XVI, 101230I (2017).
7. E. J. Stanton (invited), **A. Spott**, N. Volet, M. L. Davenport, and J. E. Bowers, “High-brightness lasers on silicon by beam combining,” Proc. SPIE. 10108, Silicon Photonics XII, 101080K (2017).
8. N. Volet, E. J. Stanton, M. L. Davenport, **A. Spott**, L. Chang, and J. E. Bowers, “Refined procedure for gain measurement in Fabry-Perot semiconductor lasers,” 2016 IEEE Photonics Conference (IPC), (2016).
9. **A. Spott**, J. Peters, M. L. Davenport, E. J. Stanton, C. Zhang, W. W. Bewley, C. D. Merritt, I. Vurgaftman, C. S. Kim, J. R. Meyer, J. Kirch, L. J. Mawst, D. Botez, and J. E. Bowers, “Distributed Feedback Quantum Cascade Lasers on Silicon,” Int. Semicond. Laser Conf. (ISLC), Kobe, Japan, (2016).
10. **A. Spott (invited)**, J. Peters, M. L. Davenport, E. J. Stanton, C. Zhang, C. D. Merritt, W. W. Bewley, I. Vurgaftman, C. S. Kim, J. R. Meyer, J. Kirch, L. J. Mawst, D. Botez, and J. E. Bowers, “Quantum Cascade Laser Integrated on Silicon,” International Quantum Cascade Laser School and Workshop (IQCLSW), Cambridge, UK, (2016).
11. **A. Spott**, J. Peters, M. L. Davenport, E. J. Stanton, C. D. Merritt, W. W. Bewley, I. Vurgaftman, J. R. Meyer, J. Kirch, L. J. Mawst, D. Botez, and J. E. Bowers, “Quantum Cascade Laser on Silicon at 4.8 μm ,” Conference on Lasers and Electro-Optics (CLEO), (2016).
12. E. J. Stanton, **A. Spott**, M. L. Davenport, N. Volet, and J. E. Bowers, “Arrayed waveguide grating near 760 nm wavelength for integrated spectral beam combining applications,” Conference on Lasers and Electro-Optics (CLEO), (2016).

13. N. Volet, **A. Spott**, E. J. Stanton, M. L. Davenport, J. Peters, J. Meyer, and J. E. Bowers, "Semiconductor optical amplifiers at 2.0- μm wavelength heterogeneously integrated on silicon," Conference on Lasers and Electro-Optics (CLEO), (2016).
14. J. E Bowers (invited), T. Komljenovic, M. Davenport, J. Hulme, A. Y Liu, C. T Santis, **A. Spott**, S. Srinivasan, E. J Stanton, C. Zhang, "Recent advances in silicon photonic integrated circuits," Proc. SPIE. 9774, Next-Generation Optical Communication: Components, Sub-Systems, and Systems V, 977402 (2016).
15. E. J. Stanton, M. J. Heck, J. Bovington, **A. Spott**, and J. E. Bowers, "Ultra-broadband Spectral Beam Combiner," Conference on Lasers and Electro-Optics (CLEO), (2015).
16. **A. Spott (post-deadline)**, M. L. Davenport, J. Peters, J. T. Bovington, M. J. Heck, J. E. Bowers, "A CW Mid-infrared Hybrid Silicon Laser at Room Temperature," 2014 IEEE Photonics Conference (IPC), (2014).
17. J. E. Bowers, E. J. Stanton, M. J. Heck, **A. Spott**, M. L. Davenport, A. Y. Liu, and J. T. Bovington, J. R. Meyer, C. L. Canedy, J. Abell, C. D. Merritt, W. W. Bewley, C. S. Kim, and I. Vurgaftman, "Technology for Multispectral Infrared Laser Integration on Silicon," IEEE Summer Topicals Meeting, Montreal, Quebec, Canada, (2014).
18. R. Ding, T. Baehr-Jones, W.-J. Kim, B. Boyko, R. Bojko, **A. Spott**, A. Pomerene, C. Hill, W. Reinhardt, M. Hochberg, "Asymmetric strip-loaded slot waveguides and its applications in silicon-polymer hybrid electro-optic modulators," IEEE Photonics Conference (PHO), (2011).
19. A. Ayazi, T. Baehr-Jones, R. Ding, M. Gould, W.-J. Kim, **A. Spott**, S. Huang, J. Luo, B. Boyko, R. Bojko, A. KY Jen, L. Dalton, M. Hochberg, "Towards a low-loss, ultra-low drive voltage silicon-polymer hybrid electro-optic modulator," Group IV Photonics (GFP), (2011).
20. **A. Spott (invited)**, R. Ding, T. Baehr-Jones, W.-J. Kim, X. Xiong, R. Bojko, J.-M. Fedeli, M. Fournier, and M. Hochberg, "Photolithographic fabrication of slot waveguides," Proc. SPIE. 7927, Advanced Fabrication Technologies for Micro/Nano Optics and Photonics IV, 792704 (2011).
21. **A. Spott (invited)**, Y. Liu, T. Baehr-Jones, R. Ilic, and M. Hochberg, "Mid-infrared photonics in silicon," Proc. SPIE. 7917, Nonlinear Frequency Generation and Conversion: Materials, Devices, and Applications X, 79171B (2011).
22. Y. Liu, **A. Spott**, T. Baehr-Jones, R. Ilic, and M. Hochberg, "Silicon waveguides and ring resonators at 5.5 μm ," in Group IV Photonics (GFP), (2010).

Abstract

Heterogeneous Integration of Mid-infrared Lasers on Silicon

by

Alexander Weber Spott

The mid-infrared spectral region, $\sim 2\text{--}20\ \mu\text{m}$, is of interest for numerous sensing, medical, industrial, and military applications. The rovibrational transition energies of many important molecules fall within this region, making mid-infrared light particularly suitable for gas sensing or material identification. Mid-infrared chemical bond spectroscopy of the earth's atmosphere and planetary bodies helps improve our understanding of greenhouse gases, pollutants, and biochemical compositions. Defense technologies, including scene illumination and infrared counter-measures, benefit from high-power mid-infrared light sources. The atmospheric transmission windows in the $\sim 3\text{--}5\ \mu\text{m}$ and $\sim 8\text{--}13\ \mu\text{m}$ ranges can extend infrared technologies to longer distances for remote explosive detection, thermal imaging, and free-space communications.

Silicon photonic integration promises to address many of these applications on an integrated, low-cost platform. For example, a diverse portfolio of photonic sensors can potentially be integrated on a single silicon chip. Resonators, multiplexers, modulators, phase shifters, frequency combs, detectors, and various other optical devices operating at wavelengths throughout the mid-infrared have already been demonstrated on silicon photonic waveguiding platforms. Heterogeneous integration, where III-V material layers are transferred above silicon waveguides by wafer- or die-bonding, has previously been applied to construct near-infrared lasers on silicon, however, prior to 2014 no mid-infrared laser source integrated on silicon had been reported.

This thesis presents the heterogeneous silicon/III-V integration of mid-infrared InP-

based type-I diode lasers for $\lambda \approx 2.0 \mu\text{m}$, InP-based quantum cascade lasers (QCLs) for $\lambda \approx 4.8 \mu\text{m}$, and GaSb-based interband cascade lasers (ICLs) for $\lambda \approx 3.7 \mu\text{m}$. These Fabry-Perot and distributed feedback (DFB) lasers function above room temperature, are integrated on silicon substrates, and couple mid-infrared light into silicon waveguides. The design considerations, fabrication processes, and performance of each set of lasers are discussed in detail.

Contents

Curriculum Vitae	viii
Abstract	xii
List of Figures	xvi
1 Introduction	1
1.1 The Mid-Infrared	1
1.2 Applications of Mid-Infrared Light	2
Sensing, Detection, and Identification	3
1.3 Mid-Infrared Semiconductor Lasers	5
Diode Band-to-Band Lasers	6
Quantum Cascade Lasers	7
Interband Cascade Lasers	9
1.4 Mid-Infrared Photonic Integration	10
Silicon Photonic Mid-Infrared Waveguiding Platforms	10
Mid-Infrared Waveguides and Passive Devices on Silicon	14
Mid-Infrared Active Devices on Silicon	16
Monolithic Integration	19
1.5 Conclusion	20
2 Heterogeneously Integrated Lasers	21
2.1 Background	21
Heterogeneous Integration of Active Elements on Silicon	21
2.2 Laser Design and Fabrication Overview	22
2.3 Conclusion	27
3 Mid-Infrared Diode Lasers and Amplifiers on Silicon	28
3.1 Fabry-Perot 2.0 μm Lasers Integrated on SOI	29
Design	29
Fabrication	32
Results	35

3.2	Semiconductor Optical Amplifiers for 2.0 μm	40
3.3	Conclusion and Summary	42
4	Quantum Cascade Lasers on Silicon	43
4.1	SONOI, SOI, and SON Platform	44
4.2	Fabry-Perot QCLs on SONOI	45
	Laser Design	45
	Fabrication	50
	Results	52
4.3	Distributed Feedback QCLs on SONOI	59
	Laser Designs	60
	Grating Designs	61
	Grating Fabrication	62
	Results	64
4.4	QCL Thermal Analysis	72
4.5	Conclusion and Summary	75
5	Interband Cascade Lasers on Silicon	77
5.1	Fabry-Perot ICLs on SOI	79
	Design	79
	Fabrication	83
	Results	87
5.2	Conclusion and Summary	97
6	III-V Tapers	101
6.1	Three-Section Lasers With Tapers	101
6.2	Taper Design	105
6.3	FDTD Taper Analysis	107
6.4	Conclusion and Summary	110
7	Applications	112
7.1	Power Scaling and Beam Combining	112
	Summary	116
7.2	Gas Sensors	116
	Summary	118
8	Conclusions	119
8.1	Review	119
8.2	Prospects	122
	Bibliography	123

List of Figures

1.1	The electromagnetic spectrum.	2
1.2	Molecular transition intensities within the mid-infrared for various gases.	4
1.3	(a) Strong transition line intensities of CO ₂ within the mid-infrared. (b) Much weaker transition line intensities of CO ₂ within the near-infrared. .	5
1.4	(a) Silicon-on-nitride-on-insulator (SONOI) waveguide platform supporting both nitride-on-insulator (NOI) and silicon-on-nitride (SON) waveguides. (b) Germanium-on-silicon-on-insulator waveguide platform supporting both germanium-on-silicon (GOS) and silicon-on-insulator (SOI) waveguides.	13
2.1	Three-dimensional schematic of a gain element above a silicon waveguide as part of a heterogeneously integrated laser. The III-V layers taper at both ends of the mesa to efficiently transfer light from the hybrid III-V/Si active region to passive silicon waveguides. Polished facets or integrated reflectors such as DBR mirrors can form a laser cavity. ©2017 IEEE . . .	23
2.2	A 3D schematic of (a) a silicon waveguide with a shallow surface DFB grating which lies underneath the III-V mesa of a heterogeneously integrated laser and (b) a heterogeneously integrated DFB laser.	24
2.3	A schematic view of tunable laser design with integrated external cavity. Tuners are yellow (two phase sections and two rings for wide tuning), and SOAs are dark orange (SOA1 is the laser active section, and SOA2 is used as an ON/OFF switch or to control the level of feedback). The monitor photodiode (MPD) in blue is used to measure the laser output power for adjustment of laser parameters. [1] ©2015 IEEE	25
2.4	Active region design options for heterogeneously integrated lasers. (a) A wide III-V mesa above a narrow Si waveguide. Dark areas represent high resistivity regions formed by proton implantation on both sides of a central current channel. (b) A narrow III-V mesa above a narrow Si waveguide. (c) A narrow III-V upper cladding with a wide III-V lower cladding and active region. Alternatively, the narrow upper cladding can be only partially etched. ©2017 IEEE	25

2.5	Generalized process flow of a heterogeneously integrated III-V element with a silicon waveguide. (a) Silicon processing including waveguide and grating etching. (b) Bond III-V layers and remove substrate. (c) Etch III-V mesa, stopping within bottom contact layers. (d) Deposit metal for bottom and top electrodes. (e) Optional: proton implantation to define a current channel. (f) Etch vias and deposit probe metal. ©2017 IEEE . . .	27
3.1	Cross-sectional schematic of the hybrid III-V/Si active region of a heterogeneously integrated $\lambda \approx 2.0 \mu\text{m}$ laser.	31
3.2	Simulated optical mode profiles and estimated MQW optical confinement factor of hybrid III-V/Si active region for various silicon waveguide widths of a heterogeneously integrated $\lambda \approx 2.0 \mu\text{m}$ laser.	31
3.3	Process flow of a heterogeneously integrated $\lambda \approx 2.0 \mu\text{m}$ laser: (a) Silicon waveguide and vertical channel etch. (b) III-V bonding and substrate removal. (c) Mesa dry and wet etch steps. (d) n-Metal deposition. (e) n-InP etch. (f) SiO ₂ deposition and via etch. (g) p-Metal deposition. (h) Proton implantation.	34
3.4	Optical microscope images of (a) a fully-fabricated $\lambda \approx 2.0 \mu\text{m}$ laser on silicon with a 1-mm-long III-V mesa (b) a lasers III-V taper region. . . .	34
3.5	Light intensity versus current at four temperatures for a laser with 2-mm-long mesa, 4- μm -wide current channel, and 1.5- μm -wide silicon waveguide. Inset: current versus voltage for this device at 23C.	35
3.6	Light intensity vs. drive current for the best performing devices. (a) A laser with a 1-mm-long and 6- μm -wide III-V mesa, 4- μm -wide current channel, and 1.5- μm -wide silicon waveguide. The threshold current is 59 mA. (b) A laser with a 2-mm-long and 24- μm -wide III-V mesa, 4- μm -wide current channel, and 2- μm -wide silicon waveguide. The maximum output power is 4.2 mW.	36
3.7	Histogram of the threshold current density at 20 °C for 50 heterogeneously integrated $\lambda \approx 2.0 \mu\text{m}$ of various geometries.	36
3.8	Continuous-wave (CW) single-sided output power versus drive current of a heterogeneously integrated $\lambda \approx 2.0 \mu\text{m}$ laser, showing a maximum of 8.7 mW at 20 °C.	37
3.9	Dependence of threshold current and maximum single-sided output power on silicon waveguide width for heterogeneously integrated $\lambda \approx 2.0 \mu\text{m}$ lasers with 2-mm-long III-V mesas.	38
3.10	Dependence of threshold current and maximum single-sided output power on silicon waveguide width for heterogeneously integrated $\lambda \approx 2.0 \mu\text{m}$ lasers with 1-mm-long III-V mesas.	38
3.11	Normalized optical spectra at various temperatures for a heterogeneously integrated $\lambda \approx 2.0 \mu\text{m}$ laser with a 2-mm-long III-V mesa. Peak wavelengths are indicated on the horizontal axis.	39

3.12	On-chip gain measured at 20 °C for an integrated 2- μm SOA (a) vs. the drive current for wavelengths from 2.01 μm to 2.06 μm and (b) vs. the pump wavelength for drive currents from 130 mA to 330 mA.	41
4.1	Loss due to substrate leakage for a 1.5 μm -tall and 2.0 μm -wide silicon waveguide for (a) SONOI , as a function of the buried SiO ₂ thickness and (b) SON, as a function of the buried SiN layer. (c) A FIMMWAVE simulation of the electric field intensity of the TM mode of a 1.5 μm \times 2.0 μm SONOI waveguide.	46
4.2	Optical microscope image of an integrated QCL on silicon.	46
4.3	Polished SONOI end-facet of an integrated QCL.	47
4.4	Cross-sectional schematic of an integrated QCL active region. A contour plot of the electric field component, $ E_y $, of the simulated fundamental TM optical mode is overlaid.	48
4.5	Fabrication steps of the SONOI waveguides. (a) Begin with the NOI chip. (b) Dry etch the vertical outgassing channels through the Si ₃ N ₄ and into the SiO ₂ . (c) Bond the SOI chip to the NOI chip. (d) Remove the Si substrate. (e) Remove the SiO ₂ layer with buffered HF. (f) Dry etch the vertical outgassing channels in the Si device layer for later QCL bonding. (g) Dry etch the strip waveguides.	51
4.6	Steps to fabricate the integrated QCLs on silicon. (a) Bond the QCL material to the SONOI chip. (b) Remove the InP substrate. (c) Dry etch the top InP cladding. (d) Wet etch the QCL active stages. (e) Deposit n-metal for the bottom contact. (f) Dry etch the bottom InP cladding. (g) Deposit a SiN cladding by PECVD. (h) Dry etch vias. (i) Deposit n-metal for the top contact. (j) Deposit the probe metal.	53
4.7	Single-sided pulsed optical output power and voltage versus drive current of two $\lambda \approx 4.8 \mu\text{m}$ QCLs-on-SONOI with 4 mm-long active regions and 6 μm -wide III-V mesas. The silicon waveguides of Devices A and B are 1 μm and 1.5 μm wide, respectively. The lasers were driven at 20 °C with a pulsed current source that produced 250 ns wide pulses at a 1 kHz repetition rate. Light is collected from the polished passive SONOI facet.	54
4.8	(a) Single-sided pulsed optical output power versus drive current for a $\lambda \approx 4.8 \mu\text{m}$ QCL-on-SONOI with a 4 mm-long active region, tested at temperatures from 10 °C to 60 °C. This laser (Device A) has a 6 μm wide III-V mesa and a 1.0 μm wide silicon waveguide. Light is collected from the polished passive SONOI facet. (b) Corresponding threshold current densities versus temperature. The fit yields a characteristic temperature of T ₀ 175K.	55
4.9	Emission spectra of Device B, a 4 mm-long $\lambda \approx 4.8 \mu\text{m}$ QCL integrated on SONOI. This device has a 6 μm -wide III-V mesa and a 1.5 μm -wide silicon waveguide. The laser was measured with a monochromator at 20 °C.	56

4.10	Far-field intensity of a $\lambda \approx 4.8 \mu\text{m}$ QCL integrated on SONOI with a 4 mm-long active region, as a function of the angle normal to the facet in the slow (horizontal) axis (top) and fast (vertical) axis (bottom). Solid lines indicate measurements, and dotted lines indicate simulated profiles. Measurements were taken at 20 °C and a drive current of 500 mA. This laser (Device A) had a 6 μm -wide III-V mesa and a 1.0 μm -wide silicon waveguide.	57
4.11	Pulsed single-sided output power versus drive current at 20 °C for a $\lambda \approx 4.8 \mu\text{m}$ QCL-on-SONOI with a 4 mm-long active region, before and after depositing an AR coating on a SONOI waveguide facet. This laser (Device A) had a 6 μm -wide III-V mesa and a 1.0 μm -wide silicon waveguide.	58
4.12	Cross-sectional schematics of the active regions for four different DFB QCL-on-SONOI designs. Simulated optical modes are overlaid (TM ₀₀ for Designs A, B, and D, and TM ₁₀ for Design C), and the active region transverse optical confinement factor Γ for each design is indicated.	61
4.13	A 3D schematic of (a) a SONOI waveguide with shallow surface DFB grating, which lies underneath the integrated QCL (b) a DFB QCL heterogeneously integrated with a SONOI waveguide, including III-V tapers on both sides of the laser (c) an integrated DFB QCL with one taper removed to expose a hybrid III-V/Si facet.	64
4.14	Pulsed output power and voltage vs. injection current density and current at 20 °C of an integrated $\lambda \approx 4.8 \mu\text{m}$ DFB QCL-on-SONOI of Design D with a 3 mm-long active region and III-V tapers on both sides. Light is collected from the polished passive SONOI facet. This laser had a 6 μm -wide upper InP cladding, a 24 μm -wide QCL active region, and a 1.5 μm -wide silicon waveguide.	65
4.15	Pulsed output power vs. injection current density at 20 °C for $\lambda \approx 4.8 \mu\text{m}$ DFB QCLs-on-SONOI after taper removal, with four different active region designs and various grating pitches. Light is collected from a polished hybrid Si/III-V facet.	66
4.16	Slow-axis far field profiles for a $\lambda \approx 4.8 \mu\text{m}$ DFB QCL-on-SONOI of each of four active region design. The drive currents were 200, 350, 500, and 700 mA for Designs A-D, respectively. The solid curves show the measured profiles while the dashed curves show the simulated profiles for the TM ₀₀ mode in (a), (b), and (d) and the TM ₁₀ mode in (c).	67
4.17	Normalized emission spectra at 20 °C of $\lambda \approx 4.8 \mu\text{m}$ DFB QCLs-on-SONOI with four designs, as measured with a monochromator. The spectra were obtained at currents of ~ 0.3 A for Designs A and B, 0.5 A for Design C, and 0.7 A for Design D. The legends show the DFB grating pitches of each device.	69

4.18	(a) Measured peak wavelengths as a function of DFB grating pitch for all four $\lambda \approx 4.8 \mu\text{m}$ DFB QCLs-on-SONOI of Design C, from the spectral data of Figure 4.17(c). Multiple points of the same color (a single grating pitch) represent the multiple spectral peaks for that device. The circled points represent the strongest peak for that device. The dashed lines, with a slope of $\sim 6.2 \text{ nm/nm}$ ($\approx 2 n_{eff}$), show that modes lasing at the edges of the 90 nm wide stopband track the fabricated grating pitch. As in Table 4.3, the simulated n_{eff} of the TM_{10} mode is 3.108 (b) Measured peak wavelength as a function of calculated Bragg wavelength for the strongest lasing mode of the devices shown in Figure 4.17.	70
4.19	(a) Pulsed output power for a $\lambda \approx 4.8 \mu\text{m}$ DFB QCL-on-SONOI of Design B at temperatures ranging from 10 °C to 100 °C. The III-V mesa width was 6 μm and the silicon waveguide width was 1.5 μm . (b) Corresponding threshold current density vs. temperature, which yields a characteristic temperature of $T_0=199 \text{ K}$. (c) Corresponding differential efficiency vs. temperature, which yields a characteristic temperature of $T_1=222 \text{ K}$. . .	71
4.20	(a) Temperature-dependent emission spectra for the same $\lambda \approx 4.8 \mu\text{m}$ DFB QCL-on-SONOI with a 3 mm-long active region of Design B whose temperature-dependent L-I characteristics are shown in Figure 4.19. The III-V mesa width was 6 μm and the silicon waveguide width was 1.5 μm . (b) Peak wavelength as a function of temperature.	72
4.21	2-dimensional COMSOL thermal simulations of heterogeneously integrated QCLs with 6 μm -wide QCL mesas. The simulated active region is injected with 2 A injection current biased under ideal voltage conditions at 7.75 V. All injected power is thermally dissipated and the maximum temperature is indicated. The figures on the left of (a) and (b) show a QCL ridge integrated above a SONOI waveguide, while the figures on the right of (a) and (b) show a QCL ridge integrated above a SON waveguide. For (a) the heat is extracted downward through the silicon substrate, held at 20 °C, while for (b) the heat is extracted through gold upward and through an AlN submount, held at 20 °C.	74
5.1	3D schematic of the ICL heterogeneously integrated with a silicon waveguide.	79
5.2	Cross-sectional schematic of the III-V/Si active region of an ICL-on-SOI.	80
5.3	Active region cross sections of an integrated ICL-on-Si (Device A) overlaid with contour plots of the electric field profiles $ E_x $ of the first two optical modes.	82
5.4	(a) Top-down optical microscope image of fully-fabricated ICLs integrated on silicon. (b) Scanning electron microscope (SEM) images of the III-V taper tip of a representative device. Left: before SiN encapsulation. Right: after probe metal deposition.	84

5.5	Simplified fabrication process flow for the integrated ICLs-on-SOI. Hard masks, via etches, and probe metals are not shown. (a) Beginning with an SOI wafer with 1.5 μm of silicon on top, Si waveguides are partially etched, and VOCs (not shown) are fully etched. (b) The ICL chip is flip-chip die-bonded to the Si. (c) The GaSb substrate is removed by mechanical lapping, followed by chemical etching. (d) The upper cladding, top SCH layer, and active ICL stages are etched to form a mesa above the Si waveguide. (e) The bottom SCH layer is selectively chemically-etched to reveal the bottom contact layer. (f) Ti/Pt/Au is deposited for bottom metal contacts. (g) The remaining III-V layers are etched. (h) Ti/Pt/Au is deposited for top metal contacts after SiN deposition and via etches.	85
5.6	Single-sided pulsed output power (in arbitrary units) and voltage vs. drive current at 20 $^{\circ}\text{C}$ for $\lambda \approx 3.6 \mu\text{m}$ ICLs-on-SOI with 3.1 mm-long active regions. Light was collected from a passive silicon waveguide facet. The silicon waveguides under the active region were 1 μm wide and the III-V mesas were (a) 11 μm wide (Device A) and (b) 8 μm -wide (Device B).	88
5.7	Emission spectra at 20 $^{\circ}\text{C}$ of two integrated $\lambda \approx 3.6 \mu\text{m}$ ICLs-on-SOI with 3.1 mm-long active regions. Devices A and B had 11 μm -wide and 8 μm -wide III-V mesas, respectively, and 1 μm -wide silicon waveguides. Light was collected from a passive silicon waveguide facet.	89
5.8	(a) Single-sided pulsed output power vs. drive current at 20 $^{\circ}\text{C}$ collected from a polished hybrid III-V/Si facet after taper removal of three $\lambda \approx 3.6 \mu\text{m}$ ICLs-on-SOI. (b) Voltage vs. drive current density for Devices A, B, C, and a 32 μm -wide ICL ridge fabricated on a native GaSb substrate for reference. Devices A, B, and C had 11 μm , 8 μm , and 6 μm -wide III-V mesas, respectively. Devices A and B had 1 μm -wide silicon waveguides, while Device C had a 2 μm -wide silicon waveguide.	90
5.9	Emission spectra, collected from a polished hybrid III-V/Si facet at 20 $^{\circ}\text{C}$, of three $\lambda \approx 3.6 \mu\text{m}$ ICLs-on-SOI after taper removal. Devices A, B, and C had 11 μm , 8 μm , and 6 μm -wide III-V mesas, respectively. Devices A and B had 1 μm -wide silicon waveguides, while Device C had a 2 μm -wide silicon waveguide.	92
5.10	Far field intensity as a function of the angle normal to the facet in the slow (horizontal) axis of three $\lambda \approx 3.6 \mu\text{m}$ ICLs-on-SOI, measured from polished hybrid III-V/Si facets. Solid lines indicate measured profiles and dashed lines indicate simulated TE_{10} profiles. Measurements were taken at 20 $^{\circ}\text{C}$ and a drive current of 640 mA (Devices A and C) and 700 mA (Device B). Devices A, B, and C had 11 μm , 8 μm , and 6 μm -wide III-V mesas, respectively. Devices A and B had 1 μm -wide silicon waveguides, while Device C had a 2 μm -wide silicon waveguide.	93

5.11	(a) Single-sided output power vs. drive current of a $\lambda \approx 3.6 \mu\text{m}$ ICL-on-SOI (Device A with an $11 \mu\text{m}$ -wide III-V mesa and a $1 \mu\text{m}$ -wide silicon waveguide) at temperatures ranging from $-100 \text{ }^\circ\text{C}$ to $50 \text{ }^\circ\text{C}$ after taper removal. (b) Threshold current density vs. temperature. The characteristic temperatures are separately calculated for lower temperatures -100 – $-20 \text{ }^\circ\text{C}$ (green, $T_0 = 106 \text{ K}$) and higher temperatures 0 – $50 \text{ }^\circ\text{C}$ (blue, $T_0 = 43 \text{ K}$).	95
5.12	Pulsed threshold voltage vs. temperature for a $\lambda \approx 3.6 \mu\text{m}$ ICL-on-SOI with an $11 \mu\text{m}$ -wide III-V mesa and a $1 \mu\text{m}$ -wide silicon waveguide (Device A).	97
5.13	Emission spectra measured from a polished hybrid III-V/Si facet of a $\lambda \approx 3.6 \mu\text{m}$ ICL-on-SOI with an $11 \mu\text{m}$ -wide III-V mesa and a $1 \mu\text{m}$ -wide silicon waveguide (Device A) at (a) a broad temperature range $-100 \text{ }^\circ\text{C}$ to $50 \text{ }^\circ\text{C}$ and (c) a narrow temperature range $10 \text{ }^\circ\text{C}$ to $50 \text{ }^\circ\text{C}$. (b) Peak wavelength vs. temperature of Device A.	98
6.1	Top-down schematic of the silicon waveguide and III-V mesas during the taper section of the QCLs-on-SONOI described in this dissertation. . . .	105
6.2	Contour plot of the effective index of the fundamental TM_{00} mode in the active region of a QCL-on-SONOI, as a function of the silicon waveguide and III-V mesa widths.	106
6.3	3D image of the QCL-on-SONOI taper structure simulated in FDTD. . .	107
6.4	Contour plots showing reflection (left) and loss (right) induced by the taper of a QCL-on-SONOI, according to FDTD simulations.	108
6.5	Plots showing (a) taper reflection as a function of taper tip width, (b) taper reflection as a function of taper length, (c) taper transmission as a function of taper tip width, and (d) taper transmission as a function of taper length for a QCL-on-SONOI taper.	109
6.6	Simulated transmission (a) and reflection (b) of a QCL-on-SONOI taper as a function of misalignment of the III-V taper with respect to the silicon waveguide.	110
6.7	Simulated transmission (a) and reflection (b) of a $45 \mu\text{m}$ long taper of a QCL-on-SONOI as a function of the number of QCL stages.	111
7.1	Multispectral laser architecture with multiple gain materials bonded onto a Si substrate. Each laser output is spectrally combined in multiple stages to a single output waveguide. ©2017 IEEE	113
7.2	A schematic of DFB QCLs integrated with an AWG to combine the output emission into a single waveguide.	114
7.3	(a) Light emission and voltage vs. drive current per laser for combinations of 1, 2, or 3 multispectral QCLs-on-SOI being operated at the same time. (b) Optical spectrum of light collected from the AWG output waveguide while 3 QCLs are being driven simultaneously.	115

7.4	(a) FTIR spectrum vs. injection current, showing the tuning range of a QCL-on-SONOI and its transition from single-mode to multi-mode operation. (b) CO ₂ absorption spectrum.	116
7.5	Normalized transmission through a CO ₂ flow cell (black) compared to reference data (red) from the HITRAN database that has been scaled (reduced to 23%) to match the transmission minima of the data.	118

Chapter 1

Introduction

1.1 The Mid-Infrared

Figure 1.1 depicts the electromagnetic spectrum. The infrared (IR) occupies the regime neighboring the red portion of the visible wavelengths beginning near $\lambda \approx 700$ nm and extending to the border of the terahertz regime at $\lambda \approx 100$ μm .

The infrared wavelengths are split into several smaller regions. The near-infrared (NIR) spans ~ 0.7 – 2.0 μm , the mid-infrared (MIR, mid-wave IR, or MWIR) spans ~ 2.0 – 20 μm , and the far-infrared (FIR) spans from ~ 20 μm to the Terahertz. These limits are common in integrated photonics literature and will be used throughout this dissertation, but the wavelength extents of these regimes are not consistently defined. The mid-infrared is sometimes chosen to begin at 3.0 μm and the far-infrared is sometimes chosen to begin at 15 μm . For astronomy applications, the mid-infrared region is often defined as a much wider range, 5 – 40 μm . Additional overlapping categories are also used: the short-wave infrared (SWIR), ~ 2 – 3 μm and the long-wave infrared (LWIR), ~ 7 – 20 μm .

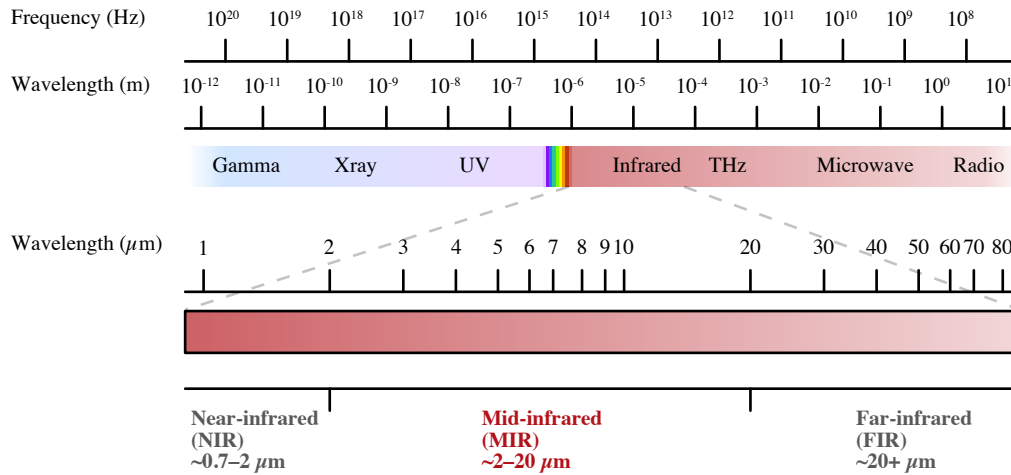


Figure 1.1: The electromagnetic spectrum.

1.2 Applications of Mid-Infrared Light

Mid-infrared light can be applied to a variety of commercial, industrial, scientific, and military technologies. Many of these applications can be placed into three categories due to specific unique attributes of mid-infrared light. First, mid-infrared light strongly interacts with many chemicals and materials, making it useful for optical sensors, detectors, and spectroscopy. Second, objects at near room- and body-temperatures (and up to ~ 1000 °C) have thermal blackbody signatures which emit strongly at mid-infrared wavelengths, which is important for thermal vision and military applications. Third, limited optical portions of the electromagnetic spectrum are able to travel long distances through the Earth's atmosphere without being strongly absorbed or scattered by aerosols or gases. Some important atmospheric transmission windows lie within the mid-infrared. Applications in each of these categories can benefit from some level of chip-scale integration.

Sensing, Detection, and Identification

Many chemicals and gases have rovibrational transition energies which correspond with the photon energies of light at mid-infrared wavelengths. Figure 1.2 shows the molecular transition intensities at mid-infrared wavelengths for several gases of interest (where the transition intensities correspond with the absorption of light). The mid-infrared is often referred to as the 'fingerprint region' because the absorption spectra in this region of different chemicals include strong and unique identifying characteristics. Figure 1.3(a) shows a group of the stronger transition line intensities of CO₂ between 2280 cm⁻¹ ($\sim 4.39 \mu\text{m}$) and 2390 cm⁻¹ ($\sim 4.18 \mu\text{m}$). Gases do typically have characteristic absorption lines outside of the mid-infrared regime, but the strength of these molecular transitions are often orders of magnitude weaker than those within the mid-infrared. For example, Figure 1.3(b) shows one of the near-infrared transition intensity features of CO₂. Note that although the grouping of transition lines is similar, the intensity of the transition lines is about 5 orders of magnitude weaker.

These absorption lines can be exploited with a variety of techniques to identify or measure the abundance of various substances. Substances can be identified by observing the optical transmission through the substance for a broad range of wavelengths within the mid-infrared, and comparing the results with the absorption signature of known materials. This technique is used for fourier-transform infrared (FT-IR) spectroscopy, where the light is spectrally measured with an FT-IR spectrometer. The strength of individual unique absorption lines, compared to a known standard, can also be measured to determine the abundance of a substance in gas phase. This technique is termed tunable diode laser absorption spectroscopy (TDLAS) when tunable semiconductor lasers are used. Gas sensors based on TDLAS are particularly well-suited for miniaturization with integrated optical devices. A demonstration which uses the lasers developed within

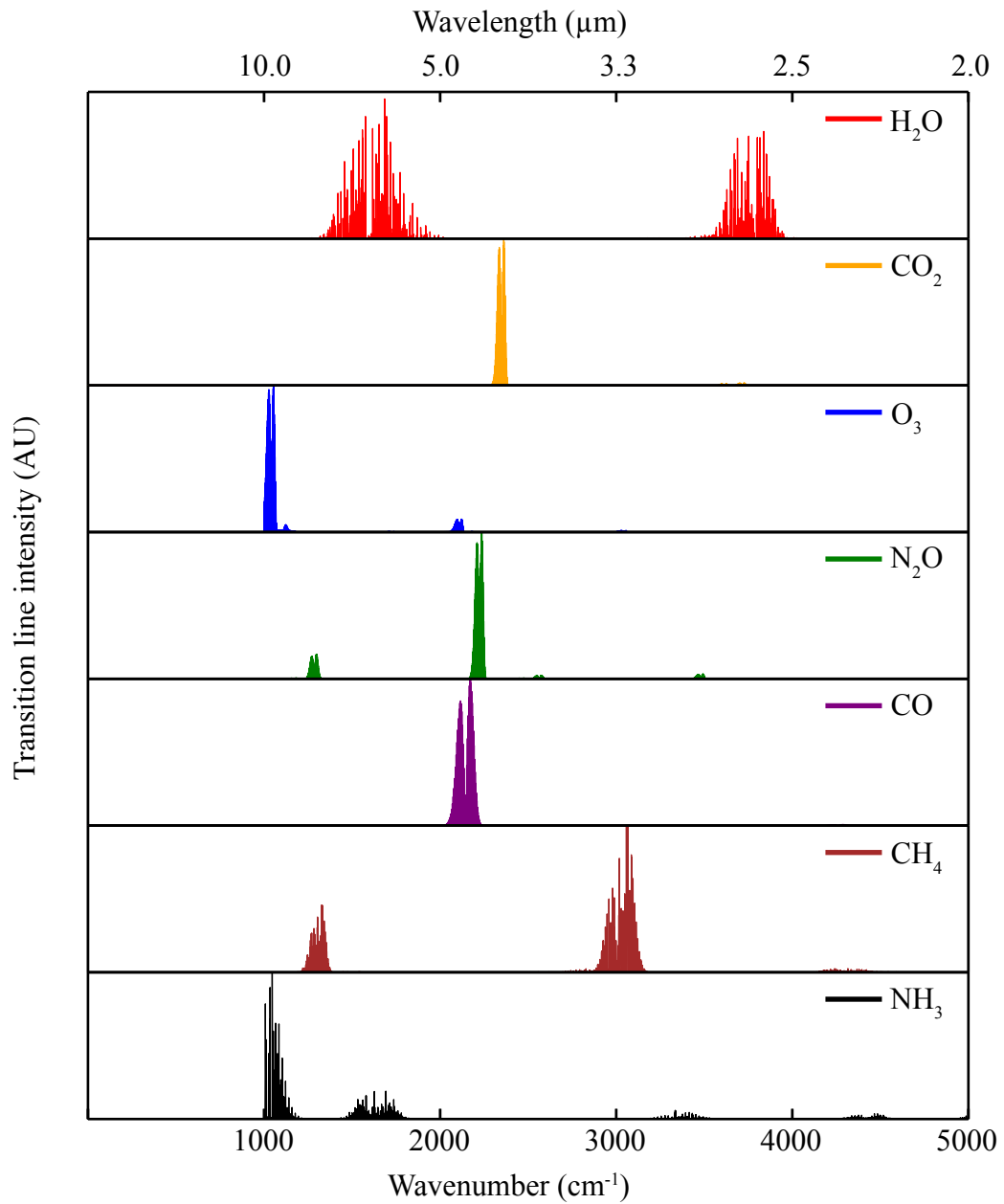


Figure 1.2: Molecular transition intensities within the mid-infrared for various gases.

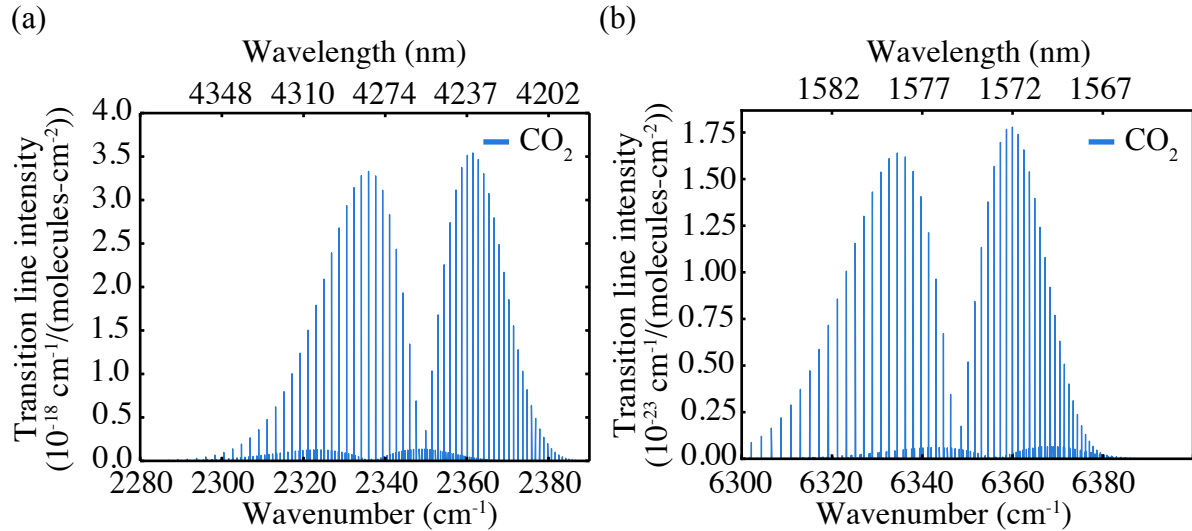


Figure 1.3: (a) Strong transition line intensities of CO₂ within the mid-infrared. (b) Much weaker transition line intensities of CO₂ within the near-infrared.

this dissertation is discussed in Chapter 7.2. Gas sensors and chemical bond spectroscopy systems are currently implemented in free-space optical systems, but significant progress has been made miniaturizing such technologies.

1.3 Mid-Infrared Semiconductor Lasers

Three primary classes of semiconductor lasers operate in the mid-infrared: diode lasers, quantum cascade lasers (QCLs), and interband cascade lasers (ICLs). Each of these technologies function with different performance across different wavelength ranges. Table 1.3 shows the current relative limits in operating wavelength, although rapid progress continues to extend these ranges. Performance metrics also vary between technologies, including wall-plug efficiency, optical power output, electrical drive power, and even optical emission polarization.

Table 1.3: Mid-infrared semiconductor laser technologies

Substrate	Technology	Wavelength range (μm)
InP	Type-I diode	NIR–2.4 [2]
InP	Type-II diode	\sim 2.0–2.6 [3]
GaSb	Type-I diode	1.9–3.7 [4, 5, 6]
GaSb	Interband cascade laser	2.9–7.0 [7]
InP, GaAs, InAs	Quantum cascade laser	3.0–20+ (and THz) [8, 9]

Diode Band-to-Band Lasers

Mid-infrared diode band-to-band emitters, which achieve gain by electron-hole recombination across a semiconductor band gap, are attractive both because of their relative simplicity (compared to cascading lasers) and the mature technological backbone provided by decades of research on shorter wavelength lasers. Mid-infrared diode lasers are primarily grown on either InP or GaSb substrates, using either direct type-I band-to-band recombination or indirect type-II band-to-band recombination. Band-to-band diode lasers particularly dominate the shorter 2–3 μm wavelengths of the mid-infrared below the lower limit of quantum cascade and interband cascade lasers.

Interband mid-infrared lasers suffer from non-radiative carrier loss from Auger recombination. The Auger recombination rate increases exponentially with decreasing band gap, E_g , (proportional to $\exp(\frac{-E_g}{kT})$) therefore becoming rapidly problematic for longer wavelengths. Compressively straining the quantum wells or careful band structure engineering have been applied to mitigate Auger recombination.

GaSb-based type-I diode lasers typically use GaInAsSb QWs with AlGa(In)AsSb barriers of varying stoichiometric composition. The best performance is achieved at wavelengths between 2–3 μm where hundreds of mW to over a Watt of continuous-wave room-temperature output power has been demonstrated [10, 11]. Room-temperature, pulsed mode operation has been achieved for up to $\lambda=3.73 \mu\text{m}$ [6]. The most notable

and best performing GaSb-based lasers using type-II interband transitions are Interband cascade lasers (ICLs) which are discussed in Section 1.3.

Type-I InP-based diodes can be extended to the mid-infrared by using In(Ga)As QWs with a composition providing a narrower band-gap. The lattice mismatch of the QWs with the InP substrate produces significant strain which results in a higher density of misfit dislocations for thicker QWs. Such dislocations provide nonradiative recombination centers which reduce the useful carrier density and limit the laser performance. Thus, the upper wavelength limit is constrained by the tolerable QW strain and thickness. Strained InAs/InGaAs triangular QWs with InGaAs barriers have been used for lasers which emit light at $\lambda \approx 2.4 \mu\text{m}$ [2]. Type-II transitions at a InGaAs/GaAsSb interface can also provide gain on an InP substrate, with a slightly longer wavelength limit of $\lambda \approx 2.6 \mu\text{m}$ [3]. As the wavelength range of QCLs begins at $\sim 3.0 \mu\text{m}$, the InP system has a wavelength gap between $\sim 2.5\text{--}3.0 \mu\text{m}$.

Quantum Cascade Lasers

Quantum cascade lasers (QCLs) [8] were first demonstrated in 1994 by Faist et al. [12]. As opposed to interband transitions used to generate gain in diode lasers and interband cascade lasers, QCLs depend on intersubband transitions of electrons between energy states within quantum wells within the conduction band. With the electron remaining in the conduction band, it can subsequently be transported by quantum tunneling through an injector region into the upper energy state of a neighboring active region quantum well, where it can undergo an additional emission transition. By cascading these injector and active regions together, QCLs recycle electrons, producing multiple photons for a single electron. QCLs typically include 30–50 stages.

Population inversion is achieved within the quantum wells by controlled tunneling

between energy states. The quantum selection rules of QCLs ensure emission in the transverse magnetic (TM) mode for in-plane lasers and prohibits vertical out-of-plane emission, such as in a vertical-cavity surface-emitting laser (VCSEL) configuration.

Because the energy between quantum well transitions in a QCL is determined by the thickness of the quantum wells rather than the band gap intrinsic to the material, the emission of QCLs can be engineered across a wide range of wavelengths. Currently QCLs have demonstrated room temperature emission from $3.0\ \mu\text{m}$ to over $20\ \mu\text{m}$ and within the terahertz regime beyond $100\ \mu\text{m}$. The emission wavelength is typically limited on the short wavelength side by the conduction band offset and on the long wavelength side by the Reststrahlen band semiconductor phonon resonances.

QCLs most commonly use the InGaAs/InAlAs/InP system grown on InP substrates or the GaAs/AlGaAs system grown on GaAs substrates. To a lesser extent, QCLs also use the AlSb/InAs grown on InAs substrates or InGaAs/AlInAsSb, InGaAs/GaAsSb or InGaAs/AlInGaAs grown on InP substrates. Epitaxial growth is performed with either metalorganic chemical vapor deposition (MOCVD) or molecular beam epitaxy (MBE). QCLs typically include 100s of layer transitions and require high precision of the thickness of each individual layer.

The Auger effect, which is otherwise a limiting factor in interband transition devices, is not relevant to intersubband emissions and therefore does not serve as a limit to QCL performance. Instead, the dominant nonradiative recombination mechanism in a QCL is optical phonon scattering. Although threshold current densities tend to be high in QCLs compared to interband lasers, very high output powers are achievable. Individual QCL emitters outputting over 5 W have been demonstrated [13].

Heat dissipation is a primary challenge with QCLs. The large number of QCL stages requires high drive voltages to reach threshold, which produce significant dissipated heat. 70–80% of the injected electrical power in a QCL turns into heat [14]. Wall plug effi-

ciencies have been demonstrated up to 27%, although the wall plug efficiency of a QCL typically is near $\sim 15\%$.

Interband Cascade Lasers

Interband cascade lasers combine the band-to-band electron-hole recombination of a diode laser with the cascaded electron recycling stages of a QCL [15]. ICLs were invented in 1994 [16] and first experimentally demonstrated in 1997 [17]. The first continuous-wave (CW), room temperature operation was reported by NRL in 2008 [18]. High-performance ICLs typically use a type-II active region design with a 'W' configuration with InAs electron quantum wells on both sides of the GaInSb hole quantum well [19]. This 'W' configuration improves the overlap of the electron and hole wave functions within the quantum well. Carriers are generated in between active stages at a semimetallic interface between InAs and GaSb where the InAs electron conduction subband overlaps the GaSb hole valence subband. Because the carriers are generated internally Both electron and hole injector regions transport carriers between the semimetallic interface of each stage to the neighboring active regions. ICLs typically function with fewer than 12 stages, compared to QCLs which typically require at least 30 stages for sufficient gain.

ICLs are typically grown on a GaSb substrate. In this material system, low-index cladding layers are formed by alternating InAs/AlSb superlattices (SLs) while GaSb is used for high-index separate confinement layers (SCLs) on both sides of the active stages. In recent years, longer wavelength ICLs have been grown on InAs substrates.

ICLs function at $\lambda=2.9\text{--}7.0\ \mu\text{m}$, with most of the research and the best performance demonstrations in the $3\text{--}4\ \mu\text{m}$ range. Because ICL ridges emit in the transverse electric (TE) polarization, VCSELs are possible. This opens the door to mid-infrared VCSELs, which would otherwise be limited to the wavelength operation range of diode lasers [20].

ICLs can generate up to 500 mW of CW power [21]. The threshold current densities of ICLs are significantly lower than those of QCLs, typically $\sim 150\text{--}300$ A/cm² for narrow-ridges, determined primarily by Auger recombination [22]. As a consequence of low threshold current densities and few active stages, the drive powers of ICLs are 1–2 orders of magnitude lower than those of QCLs. These low drive powers make ICLs attractive for sensing and detection applications which do not require Watt-level power. ICLs are particularly attractive for handheld or field-deployable sensing systems which can operate on batteries or solar power.

1.4 Mid-Infrared Photonic Integration

Silicon Photonic Mid-Infrared Waveguiding Platforms

Silicon photonic integration was only recently first applied to mid-infrared wavelengths. The limited availability of mid-infrared laser sources, lenses, polarizers, other free-space optical elements, and fibers historically increased the difficulty and cost required to couple mid-infrared light into passive silicon waveguides. Following drastically increased mid-infrared photonic component availability, and particularly monumental advances in semiconductor mid-infrared laser sources, mid-infrared silicon photonics has grown tremendously in the last decade.

Silicon-on-insulator (SOI) waveguides are the dominant silicon photonic platform for the near-infrared, providing low optical losses combined with high optical confinement. The material absorption of silicon dioxide, however, increases significantly at longer wavelengths and it was recognized early that SOI would not be ideal, or possibly be prohibitive, for mid-infrared wavelengths. Additionally, thicker silicon waveguide and underlying cladding layers would be needed to avoid lossy optical mode leakage into the

Table 1.4: Mid-infrared waveguide platforms

Platform	Waveguide	Cladding/substrate	λ range (μm) [23]
Si-on-insulator (SOI)	Si	SiO ₂ /Si	1.2–2.6 and 2.9–3.7
Si-on-sapphire (SOS)	Si	Al ₂ O ₃	1.2–4.4
Si-on-nitride (SON)	Si	SiN/Si	1.2–6.7
Si membrane	Si	Air/Si	1.2–8.0
Ge-on-Si (GOS)	Ge	Si	1.9–16.8
SiGe-on-Si (SGOS)	Si _{1-x} Ge _x	Si	1.6–12

substrate. Soref et al. proposed a number of possible alternative platform options in 2006 [23], many of which have since been experimentally investigated. The most promising waveguide configurations for use in the mid-infrared are silicon-on-insulator (SOI), suspended silicon, silicon-on-sapphire (SOS), silicon-on-nitride (SON), germanium-on-silicon (GOS), and germanium-on-insulator (GOI). Table 1.4 shows the wavelength ranges proposed for each of these platforms in [23], where a waveguide propagation loss of less than 2 dB/cm should be possible. Only platforms based upon dielectrics and semiconductors are discussed here, although chalcogenide glasses are also promising waveguide materials, transparent within the mid-infrared, which can be deposited on a silicon substrate [24, 25, 26].

The ultimate maximum wavelength operation range of each waveguide platform is limited by the intrinsic optical material losses of the core and cladding materials. The estimated operation limits in Table 1.4 and other work have been guided by thin film and bulk experiments in literature. These material losses are intrinsic properties of the materials, typically driven by vibrational modes arising from the structure of the amorphous or crystalline solids. These intrinsic properties are therefore, however, dependent on the stoichiometry and crystal structure of the material. Materials which are deposited or grown with different conditions can sometimes have drastically different absorption ranges.

SiO₂ for instance, is typically deposited as a stoichiometric, amorphous film, independent of deposition method. Although film characteristics vary, the stoichiometry and real and imaginary refractive indices have been observed to be relatively consistent for different sputter deposition conditions [27]. SiN films, on the other hand, vary in silicon and nitride content depending on the deposition conditions and method. Strong inhomogeneous broadening of the absorption line near 900 cm⁻¹ ($\sim 11.1 \mu\text{m}$) in a SiN film has been observed [27] for different sputter deposition conditions. This is particularly important for mid-infrared photonic devices because the degree of broadening impacts the upper-bound of the wavelength range which SiN is suitable for.

Because of this dependence on deposition conditions, the wavelength ranges shown in Table 1.4 should not be considered absolute. Many of the material absorption studies which include the mid-infrared wavelengths are several decades old and do not represent modern deposition techniques.

A low-loss waveguide is sometimes defined as a waveguide with propagation loss below 1 dB/cm ($\sim 0.23 \text{ cm}^{-1}$). Ideally material losses would be much lower to allow some tolerance for additional contributions to propagation loss. Some devices, like ultra-high-Q resonators, require propagation losses which are substantially lower, below 0.1 dB/cm [28, 29].

The operating wavelength range of these platforms can also be limited by losses which are not necessarily intrinsic to the material and may vary depending on deposition and fabrication techniques. These include scattering loss from random localized variations in the waveguide (e.g. waveguide sidewall and surface roughness), absorption related to impurities (e.g. deposition side-products like hydrogen), free-carrier absorption (dependent on material doping), and modal loss (e.g. waveguide bend loss or radiation loss from a poorly confined mode).

For applications requiring a broader wavelength range than that of any of these plat-

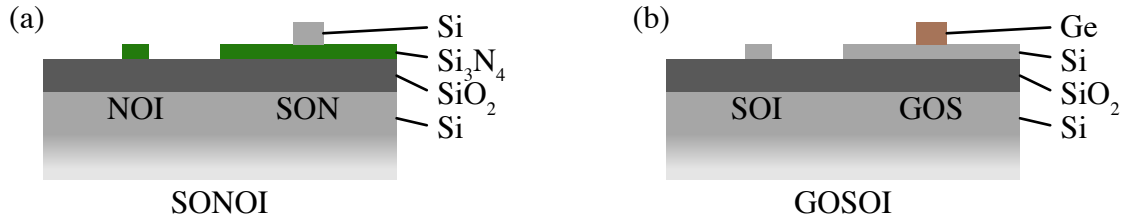


Figure 1.4: (a) Silicon-on-nitride-on-insulator (SONOI) waveguide platform supporting both nitride-on-insulator (NOI) and silicon-on-nitride (SON) waveguides. (b) Germanium-on-silicon-on-insulator waveguide platform supporting both germanium-on-silicon (GOS) and silicon-on-insulator (SOI) waveguides.

forms, a multilayer platform can be constructed. Figure 1.4 shows two options, silicon-on-nitride-on-insulator (SONOI) and germanium-on-silicon-on-insulator (GOSOI). The silicon-on-nitride-on-insulator (SONOI) platform consists of three layers on a silicon substrate: silicon on silicon nitride on silicon dioxide. In this arrangement, MIR waveguides that can potentially support light spanning $\sim 1.2\text{--}6.7\ \mu\text{m}$ are defined with a top silicon device layer and a silicon nitride under-layer. By etching off the top silicon layer, the silicon nitride can be used as a second waveguide device layer, clad by silicon dioxide, for shorter wavelengths spanning $\sim 0.35\text{--}3.5\ \mu\text{m}$. Silicon nitride waveguides have been used in the past to demonstrate the lowest on-chip waveguide losses [30, 31] and ultra-high Q resonators [28, 29] at near-infrared wavelengths. Here a single SONOI chip can operate with wavelengths spanning from the UV to the MIR. Similarly, the GOSOI platform allows the use of both SOI (for $\sim 1.2\text{--}4.4\ \mu\text{m}$) and GOS (for $\sim 1.9\text{--}16.8\ \mu\text{m}$) waveguides, which extends the GOS platform into the near-infrared. Germanium-on-silicon-on-nitride-on-insulator (GOSONOI) is also possible, for a single platform functioning from 350 nm to 16.8 μm .

Table 1.4: Low loss mid-infrared waveguides

Platform	Waveguide	Cladding	W×H ($\mu\text{m}\times\mu\text{m}$)	λ (μm)	Loss (dB/cm)
SOI	Si	SiO ₂	2.0×2.0 rib	3.39	0.6 [33]
SOS	Si	Al ₂ O ₃	1.5×0.812 rib	4.3–4.6	0.74 [34]
SGOS	Si _{1-x} Ge _x	Si	3.3×3 ridge	4.5	1 [35]
SGOS	Si _{1-x} Ge _x	Si	7.0×3 ridge	7.4	2 [35]
GOS	Ge	Si	3.0×4.3 rib	7.575	2 [36]
SON	Si	SiN	2.0×2.0 rib	3.39	5.1 [37]
NOO	SiN	SiO ₂	4.0×2.5 ridge	3.7	2.1 [38]
Si pedestal	Si	Air	8.0×5.0 ridge	3.7	2.7 [39]
GON	Ge	SiN	2.0×1.0 ridge	3.8	3.35 [40]

Mid-Infrared Waveguides and Passive Devices on Silicon

Table 1.4 shows a selection of some of the lower loss waveguide demonstrations for some of the mid-infrared material systems discussed above. This is not meant to be comprehensive, but should illustrate that <5 dB/cm loss has been achieved for most configurations, with ≤ 2 dB/cm achieved for SOI, SOS and SGOS.

Lasers in this work were constructed on both SONOI and SOI waveguides, although a comprehensive analysis of the associated passive waveguide loss has not yet been performed. Recently, an analysis of SOI waveguide loss mechanisms suggests that SOI waveguides, if properly engineered to avoid high confinement in the SiO₂ cladding, can function with <0.1 dB/cm propagation loss for $\lambda < \sim 5 \mu\text{m}$ or <1 dB/cm for $\lambda < 6 \mu\text{m}$ [32]. A number of mid-infrared waveguides and devices have been demonstrated on SOI, but most are limited to wavelengths below $\sim 3.7 \mu\text{m}$.

SOS was the first material system explored for MIR operation. The low refractive index of sapphire (Al₂O₃) allows high optical confinement in a silicon waveguide while maintaining low optical losses to at least $5 \mu\text{m}$ with no concern of mode leakage across an intermediate cladding layer. The first demonstration of mid-infrared light transmitted through a silicon waveguide was in 2010 [41] at $\lambda = 4.5 \mu\text{m}$ with 4.3 dB/cm propagation

loss. This work was followed shortly by the first ring resonators operating at a slightly longer wavelength, $\lambda=5.5 \mu\text{m}$ [42]. The SOS platform has matured significantly since 2010. In 2013, ring resonators have shown quality factors of 278,000 with 0.74 dB/cm propagation loss at $\lambda=4.3\text{--}4.6 \mu\text{m}$ [34]. Grating couplers, slot waveguides, photonic crystal cavities and waveguides, and supercontinuum generation, and other devices have now also been demonstrated [43, 44, 45, 46]. Note that SOS waveguides have been demonstrated to function above the $4.4 \mu\text{m}$ wavelength cutoff, but still with propagation losses below 2 dB/cm [47].

The GOS platform is expected to have the widest wavelength range of each of these platforms. At the lower end, the wavelength range is limited by band-to-band absorption across the $\sim 0.66\text{eV}$ band gap and is therefore unsuitable as a waveguide for the telecommunication regime. Germanium processing is CMOS-compatible and the epitaxial growth of germanium on a silicon wafer is a mature process with commercially available wafers [48]. The first demonstration of a GOS waveguide was in 2012, measuring 2.5 dB/cm at $5.8 \mu\text{m}$ wavelength [49]. Like SOS waveguides, numerous devices have now been demonstrated on GOS including AWGs, echelle gratings, thermo-optic phase shifters, all-optical modulation, etc. [50, 51, 52, 53, 54, 55]. Silicon-germanium alloys have also been investigated as an alternative waveguide to Ge in a SiGe-on-Si (SGOS) platform [56, 57]. This platform has some benefits compared to GOS waveguides because a graded $\text{Si}_{1-x}\text{Ge}_x$ index can be engineered to keep the optical mode further from the silicon (which begins to absorb around $8 \mu\text{m}$) and from the Si-Ge growth interface, where loss-inducing growth defects occur.

Mid-Infrared Active Devices on Silicon

The primary challenge for realizing a fully integrated silicon photonic platform is to make an efficient light source. Silicon has an indirect bandgap and corresponding low emission efficiency, which has limited the progress of using Si to generate light.

By wafer bonding III-V materials onto processed silicon waveguides, heterogeneously integrated III-V/Si devices can be manufactured. This approach allows III-V devices to be constructed on silicon with lithographically-limited alignment to silicon waveguides. Chapter 2 discusses the design and fabrication of heterogeneous integrated lasers in more detail, while this section overviews the most important results relevant to this dissertation.

The first electrically-pumped heterogeneously integrated laser was demonstrated on SOI in 2006 by Fang et al. [58], which operated at $\lambda=1550$ nm. Shortly after, 1310 nm lasers were also integrated on SOI [59]. Since the initial demonstrations, heterogeneous integration has progressed rapidly with new device demonstrations, design improvements, and higher levels of integration. Widely tunable, narrow-linewidth, external cavity lasers [1], high speed distributed feedback lasers [60], mode-locked lasers [61, 62], and two-dimensional beam steerers [63] have been demonstrated. Komljenovic et al. presents a review on silicon heterogeneously integrated silicon photonic circuits in [64] and Davenport et al. present a review on the design aspects of heterogeneously integrated amplifiers in [65]. Photonic integrated circuits employing heterogeneous integration have now been demonstrated with up to 426 passive and active elements for the near-infrared [66].

Heterogeneous integration allows III-V layers which were grown on separate substrates to be bonded to different areas of a silicon chip, allowing a single system to include the III-V materials best suited for each device. This multiple die bonding has been used, for example, to build an integrated triplexer which combines three III-V lasers (operating at

1.31 μm , 1.49 μm , and 1.55 μm) [67]. Broadband operation has also been achieved in a superluminescent LED by integrating multiple laser systems on the same chip [68].

Prior to 2013, heterogeneous III-V/Si integration had been almost exclusively applied to the near-infrared wavelengths near 1.55 and 1.3 μm . In 2013, ~ 1.875 μm lasers were integrated, outputting 0.62 mW from an SOI waveguide in pulsed mode at room temperature. In 2014 Bovington et al. showed 1060 nm lasers above Si_3N_4 waveguides [69]. Preliminary pulsed measurements at 10 $^\circ\text{C}$ of an integrated GaSb-based laser on silicon for $\lambda=2.38$ μm were discussed in 2014 [70], but no other reports of mid-infrared lasers on silicon were published until 2015.

Chapter 3 of this dissertation discusses the first demonstration of mid-infrared lasers on silicon operating at room temperature [71]. These lasers emit 4.2 mW CW $\lambda\approx 2.0$ μm light [72] and operated up to 35 $^\circ\text{C}$. We showed in 2017 that the same gain material can be used to construct semiconductor optical amplifiers (SOAs) on silicon (Chapter 3.2) [73]. 2.3 μm InP-based type-II Fabry-Perot lasers [74] and distributed feedback lasers [75], and an array of DFBs on silicon operating over the range $\lambda=2.28$ –2.43 μm have also now been reported using DVS-BCB bonding [76].

In 2016, we demonstrated the first QCLs integrated with silicon waveguides, for $\lambda\approx 4.8$ μm . Fabry-Perot lasers [77] emitted over 30 mW pulsed light from a silicon facet at room temperature and distributed feedback lasers [78] emitted over 200 mW pulsed light at room temperature from a hybrid III-V/Si facet with threshold current densities below 1 kA/cm^2 . These devices are discussed extensively in Chapter 4.

More recently in 2018, we also demonstrated the first GaSb-based ICLs integrated with silicon waveguides [79] for $\lambda\approx 3.6$ μm . These Fabry-Perot lasers are discussed in Chapter 5 and emitted 6.6 mW pulsed light at room temperature. Heterogeneously integrating GaSb-based devices introduces additional fabrication challenges.

Recently a transfer-printing approach was used to integrate QCLs for $\lambda=4.7$ μm above

SOS waveguides [80]. A threshold current density of 5.6 kA/cm^2 was measured with a peak pulsed power of 2 mW emit from a silicon waveguide facet. Here, pre-fabricated QCLs were transferred above a silicon waveguide and bonded with an adhesive SU-8 layer. This approach allows the QCL to be fabricated with a standard QCL process prior to bonding, but the alignment of the QCL mesa to the silicon waveguides is limited by the bonding process rather than lithographic alignment. An alternative promising transfer-printing approach which has been applied to near-infrared wavelengths is to transfer-print small coupons of III-V layer stacks rather than fully-processed devices, then fabricate active components with lithographic tolerances on silicon [81].

Heterogeneous integration has also been applied to construct mid-infrared detectors, integrated with silicon waveguides. Most of this work has been in the 2–4 μm range and includes InP-based and GaSb-based integration. In 2011, a GaInAsSb p-i-n photodiode was demonstrated for 2.29 μm operation [82]. InP-based type-II photodetectors [83] were integrated with arrayed waveguide gratings (AWGs) in 2016 [84]. Similarly, InAs_{0.91}Sb_{0.09} photodiodes [85] were integrated with AWGs on SOI for 2–3 μm wavelengths [86] and 3–4 wavelengths [87].

Some mid-infrared detectors have also been successfully demonstrated on silicon material systems by deposition or epitaxial growth, rather than wafer- or die-bonding. Most of these results have not yet been integrated with waveguides. Thermally evaporated PbTe chalcogenide films were used to build resonant-cavity photodetectors operating at $\lambda=3.5 \mu\text{m}$ with a responsivity of 100 V/W [88] and for the dual bands $\lambda=3.7 \mu\text{m}$ and $\lambda=1.6 \mu\text{m}$ [89]. GeSn-based structures have been used to extend the operation range of Ge photodetection to $\lambda=2.2 \mu\text{m}$ (chemical vapour deposited (CVD) heterostructures [90]) and $\lambda=2.3 \mu\text{m}$ (molecular beam epitaxy (MBE) grown structures [91]). Graphene on SOI enabled photodetection up to 2.75 μm integrated with waveguides [92]. III-V MBE-grown InSb photodetectors for 6.3 μm [93] and InAs/GaAs quantum dot photodetectors

for up to $\sim 8\mu\text{m}$ [94] have also been demonstrated.

Recently the first demonstration of a QCL epitaxially grown on silicon was reported [95]. This technique may help reduce the cost of individual QCLs by allowing an inexpensive silicon substrate to be used rather than an InP substrate. QCLs grown on silicon can also be used for photonic integrated circuits, either monolithically integrated on InP or heterogeneously integrated.

Monolithic Integration

Photonic integration achieved by constructing both lasers and other components on the native III-V substrates is referred to as monolithic integration within this dissertation, to distinguish the technique from heterogeneous integration. Near-infrared InP PICs for communications applications have been developed over several decades [96], but monolithic integration has only recently been applied to longer wavelengths. 2–3 μm integration of diode lasers on InP substrates is in principle most similar to techniques used for near-infrared integration, and has been used to construct widely tunable external cavity lasers [97, 98]. Integration of passive waveguides with QCLs is more challenging. Two approaches have been applied to construct passive waveguides. An InP/InGaAs/InP waveguide can be grown underneath the QCL active stages and coupled to the gain material with tapered vertical couplers [99]. Passive InGaAs waveguides, with this coupling scheme in mind, have been used to build echelle and rowland circle gratings [100, 101]. Because QCLs are unipolar devices and do not suffer from mid-infrared interband absorption, the primary loss mechanism is free-carrier absorption. By proton implanting a QCL waveguide to increase the sheet resistance of the active region layers, the propagation loss of the waveguide can be reduced. This technique was used to achieve a propagation loss of $\sim 0.33\text{ cm}^{-1}$ at $\lambda=9.6\mu\text{m}$ in an implanted passive QCL waveguide region connected to

a QCL active waveguide [102]. Finally, for a free-space sensing application not requiring a passive waveguide, a QCL for $\lambda = 6.5 \mu\text{m}$ and quantum cascade detector were constructed from the same III-V active region layers and separated by an air gap on the same chip [103].

1.5 Conclusion

Mid-infrared photonic integration has rapidly developed in the last decade. Although spread out among a handful of waveguiding platforms, all of the components necessary for fully-integrated mid-infrared systems have been demonstrated. The prospect of constructing complex mid-infrared photonic integrated circuits with integrated lasers and detectors is increasingly promising.

Chapter 2

Heterogeneously Integrated Lasers

2.1 Background

Heterogeneous Integration of Active Elements on Silicon

Heterogeneous III-V/Si integration, in the context of the semiconductor optoelectronic devices in this work, refers to the use of die- or wafer-bonding to transfer separately grown III-V crystalline semiconductor material layers onto a silicon platform. More generally, heterogeneous integration can be applied to transfer layers from differently manufactured material platforms onto a common substrate. This work uses heterogeneous integration to construct active III-V devices on SOI and SONOI waveguiding platforms.

The driving goal of heterogeneous integration is not only to construct a laser on a silicon substrate, but for the light emit by the laser to couple into silicon waveguides for use in a silicon photonic integrated circuit. Heterogeneous integration is therefore a solution to achieving an on-chip light source for silicon photonic applications.

As a more general fabrication technique, there are a few specific advantages to heterogeneous integration. First, III-V layers can be transferred from their native grown

substrates (InP, GaAs, GaSb, etc.) above the top layer on an alternative substrate. The optical, thermal, and electrical properties of the alternative substrate may be preferable to the native substrate, depending on the application. Second, the alternative substrate can be processed before bonding occurs. Features like gratings and waveguides can be introduced in between the III-V layers and the alternative substrate.

A review of heterogeneously-integrated mid-infrared devices on silicon is included in [71]. A review of previous demonstrations of these is discussed in Chapter 1.4.

2.2 Laser Design and Fabrication Overview

In principle, any active element can be heterogeneously integrated on any of the material systems described in Chapter 1.4 by bonding III-V materials above the passive device layer after the waveguide processing. Various bonding techniques have been used to effectively bond III-V layers grown on InP, GaAs, and GaSb substrates.

Wafer or die bonding can be achieved either by hydrophobic or hydrophilic bonding techniques. All of the results and designs discussed in this dissertation are achieved with low temperature hydrophilic bonding to Si, where an oxygen plasma activation is applied to the surfaces of both materials followed by an anneal [104] which is typically at 200–300 °C. Other results use a thin DVS-BCB adhesive interlayer between materials. BCB absorption is low at wavelengths up to 3- μm [70], but may increase the internal device loss for longer wavelengths.

Direct molecular hydrophilic bonding introduces a few fabrication challenges. First, the bonding process is sensitive to defects, roughness, or other topographical features on the surface of either the silicon or III-V materials. Second, the required anneal applied before the III-V substrate is removed is problematic when the thermal expansion coefficients of the III-V and silicon substrates are appreciably mismatched. For InP bonding,

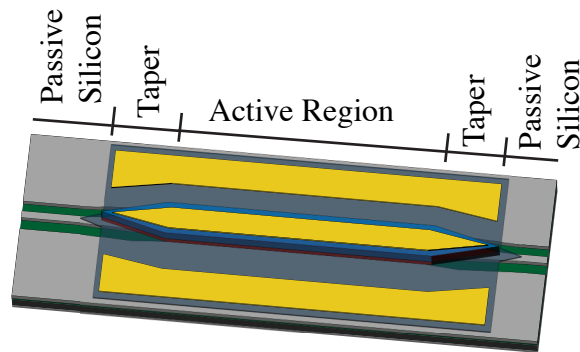


Figure 2.1: Three-dimensional schematic of a gain element above a silicon waveguide as part of a heterogeneously integrated laser. The III-V layers taper at both ends of the mesa to efficiently transfer light from the hybrid III-V/Si active region to passive silicon waveguides. Polished facets or integrated reflectors such as DBR mirrors can form a laser cavity. ©2017 IEEE

the anneal is typically limited to 300 °C. The GaSb bonding in this work uses a lower temperature anneal of 200 °C.

Figure 2.1 shows a generalized schematic of a heterogeneously integrated laser source. Here, a III-V mesa sits above a Si waveguide to form a hybrid III-V/Si active region. The III-V mesa is tapered on both sides to transfer light from the hybrid active region to passive Si waveguides on both ends. Tapering schemes can be designed with simultaneous tapering of the Si waveguide to optimize the mode coupling efficiency. Tapers are discussed in more detail in Chapter 6.

Optical feedback to form a laser cavity can be achieved in a number of ways. In the simplest case, a Fabry-Perot cavity is formed between the silicon waveguide end facets on both sides of the device. The simplicity of this scheme is favorable for the fabrication and analysis of lasers on silicon, but the isolated lasers cannot be used within an integrated circuit. Alternatively, gratings within or external to the active region can be used to achieve feedback [60, 78]. Figure 2.2(a) and (b) shows a grating on the surface of the silicon waveguide and a fabricated III-V ridge covering the grating. Feedback external to the III-V active region can also be used. A grating can be included on the surface of

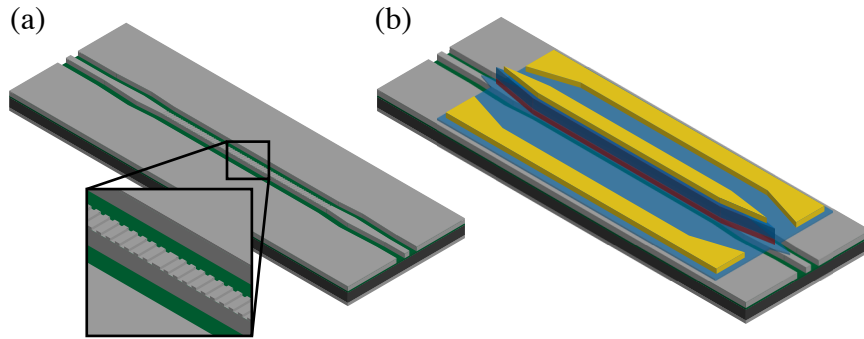


Figure 2.2: A 3D schematic of (a) a silicon waveguide with a shallow surface DFB grating which lies underneath the III-V mesa of a heterogeneously integrated laser and (b) a heterogeneously integrated DFB laser.

the passive silicon waveguide regions and used as bragg reflectors. Loop mirrors or ring mirrors can also form reflectors. Feedback elements can also be external to a laser cavity to form narrow-linewidth and broadly tunable lasers, as shown in Figure 2.3[1].

Figure 2.4 shows cross sectional schematics for three possible hybrid III-V/Si active region configurations. In all designs, a fundamental optical mode shares confinement with both the III-V layers and the Si waveguide. The Si waveguide can be either partially etched or fully etched. Both photons and electrical carriers should be confined within the active region to maximize the overlap of the optical mode with the carrier distribution. The most common design, shown in Figure 2.4(a), includes a very wide (typically near $24\text{-}\mu\text{m}$) III-V mesa which sits above a narrow Si waveguide. The optical mode is laterally confined primarily by the width of the Si waveguide, while proton implantation is implemented to form high resistivity regions which confine carriers within a narrow central current channel above the Si waveguide. A careful selection of the Si waveguide and current channel widths is required to ensure single mode operation and optimally overlap the fundamental optical mode with the injected carrier distribution in order to maximize gain and minimize losses. The potential for lasing in parasitic higher-order modes is mitigated as these modes tend to spread laterally, reducing the interaction with

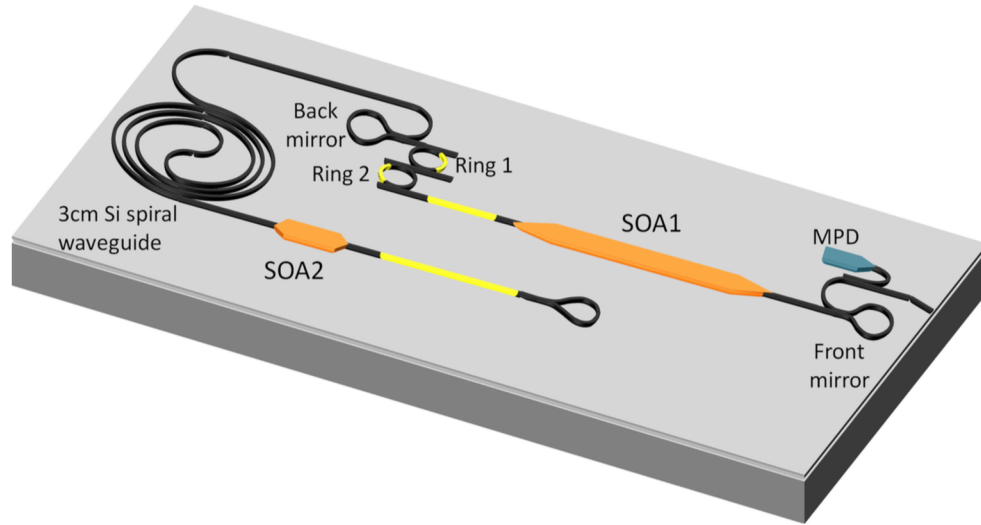


Figure 2.3: A schematic view of tunable laser design with integrated external cavity. Tuners are yellow (two phase sections and two rings for wide tuning), and SOAs are dark orange (SOA1 is the laser active section, and SOA2 is used as an ON/OFF switch or to control the level of feedback). The monitor photodiode (MPD) in blue is used to measure the laser output power for adjustment of laser parameters. [1] ©2015 IEEE

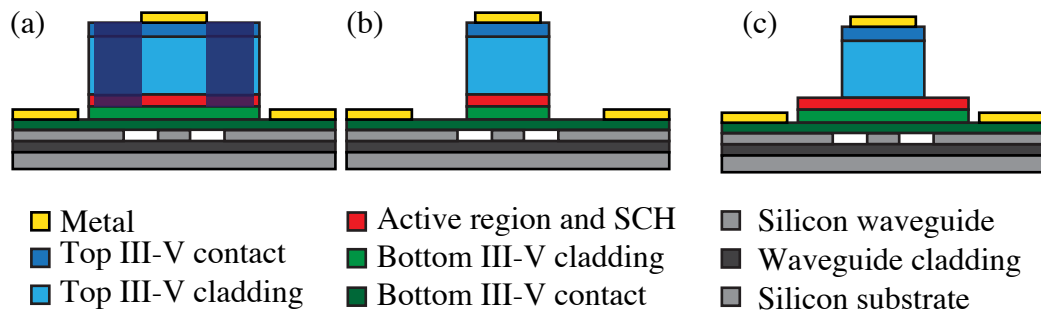


Figure 2.4: Active region design options for heterogeneously integrated lasers. (a) A wide III-V mesa above a narrow Si waveguide. Dark areas represent high resistivity regions formed by proton implantation on both sides of a central current channel. (b) A narrow III-V mesa above a narrow Si waveguide. (c) A narrow III-V upper cladding with a wide III-V lower cladding and active region. Alternatively, the narrow upper cladding can be only partially etched. ©2017 IEEE

the active region in the current channel.

In Figure 2.4(b), a narrow III-V mesa laterally confines both the current channel and the optical mode. This design more closely resembles a traditional narrow ridge laser on a native substrate, and is more suitable for lasers with upper cladding materials which are incompatible with proton implantation. A sufficiently narrow III-V mesa is required to completely cut off higher order modes, which can be difficult to achieve at shorter wavelengths. It also increases the interaction of the desired fundamental mode with the mesa sidewalls, potentially adding sidewall roughness-induced internal loss. It is possible to achieve a higher optical confinement factor with this design compared to lasers with wide III-V mesas.

Finally, the design shown in Figure 2.4(c) combines a narrow upper cladding with a wide active region. In this design a current channel is defined without proton implantation, but higher order modes still spread laterally as with the proton implanted designs. The active region and SCH layers must therefore be sufficiently thick or the narrow upper cladding should only be partially etched. This scheme has been employed primarily for the QCLs within this dissertation, with a 1510-nm thick active core.

Heterogeneously integrated lasers with an interlayer such as BCB or SiO₂ have also been constructed with no silicon waveguide within the active region.

An in-depth review of NIR heterogeneously integrated lasers and amplifiers can be found in [65].

Figure 2.5 shows a generalized process flow for an integrated III-V gain material above Si waveguides. To facilitate a short taper transition and improve coupling of the Si waveguide mode with the III-V active region, it is necessary that the lower III-V cladding and contact layers are thin. One of the primary fabrication challenges facing the heterogeneous integration of electrically-pumped active elements is etching the III-V mesa precisely down to the bottom-contact layer to deposit metal. The etch depth

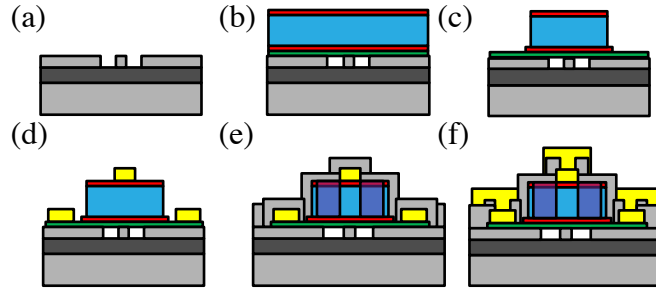


Figure 2.5: Generalized process flow of a heterogeneously integrated III-V element with a silicon waveguide. (a) Silicon processing including waveguide and grating etching. (b) Bond III-V layers and remove substrate. (c) Etch III-V mesa, stopping within bottom contact layers. (d) Deposit metal for bottom and top electrodes. (e) Optional: proton implantation to define a current channel. (f) Etch vias and deposit probe metal. ©2017 IEEE

must be uniform across the die to ensure consistency of device performance. For InP-based devices, highly selective wet etches are available and can be used to planarize the mesa etch depths, mid-process. For example, lasers with AlGaInAs quantum wells can be etched with an H_2SO_4 solution, which selectively stops on the InP bottom contact layer. Mid-infrared laser gain material compositions vary significantly depending on the wavelength and active-region technology, so precise fabrication steps and uniform control of the mesa etch depths must be optimized separately for each integration technique.

2.3 Conclusion

Heterogeneous integration, where III-V layers are bonded to silicon waveguides, is a powerful fabrication technique which enables the use of III-V active elements in silicon photonic waveguiding platforms. In principle, any active element can be heterogeneously integrated. As described in the coming Chapters of this dissertation, this integration technique can be applied to construct a variety of mid-infrared lasers on silicon.

Chapter 3

Mid-Infrared Diode Lasers and Amplifiers on Silicon

The most straightforward progression toward longer wavelengths from heterogeneously integrated near-infrared lasers is an InP-based type-I diode multiple quantum well (MQW) laser. Our first efforts therefore focused on integrating MQW diode laser material for $\lambda \approx 2.0 \mu\text{m}$. For this work, we used commercially-available epitaxial material grown at nLight [105].

This work is published in [72, 73].

UCSB: *A. Spott, M. Davenport, J. Peters, J. Bovington, M. Heck, E. Stanton, N. Volet, and J. Bowers.* A. Spott designed the fabrication process, and performed the laser characterization and facet polishing. J. Peters fabricated the lasers. N. Volet performed the amplifier characterization measurements. The team at UCSB contributed to the laser design, mask layout, fabrication process design, and data interpretation.

US Naval Research Laboratory: *C. Merritt, W. Bewley, I. Vurgaftman, C.S. Kim, and J. R. Meyer.* The team at NRL aided in the fabrication process design and

data interpretation.

3.1 Fabry-Perot 2.0 μm Lasers Integrated on SOI

Design

The III-V material was commercially grown with metalorganic chemical vapor deposition (MOCVD) on an InP substrate. The epitaxial layer stack is shown in Table 3.1 in the reverse-growth order which is the orientation after flip-chip bonding. Four InGaAs quantum wells designed for emission near 2.0 μm were used.

Some design aspects were retained from previous heterogeneously integrated near-infrared lasers. Bonding superlattice (SL) layers were formed by thin alternating layers of InGaAsP and InP. These layers are expected to prevent defects formed at the bonding interface from propagating toward the quantum wells, although this has not been experimentally explored for any of the lasers discussed in this dissertation. A 50 nm-thick InGaAs etch stop layer and a 20 nm-thick InP sacrificial layer were grown above the substrate to allow chemical removal of the substrate.

The p-doped contact, cladding, and index confinement layers were grown first to form a p-InP mesa rather than an n-InP mesa, as in previous near-infrared laser designs. This was found to be important for two primary reasons. First, in order to implement the wide-mesa proton implanted laser design 2.4(a), proton implantation of p-InP produces a higher resistivity which remains at higher anneal temperature compared to proton implantation of n-InP. Second, the p-InGaAs contacts should be on the top of the structure and highly doped, where there is negligible optical mode interaction.

Both the bottom n-InP and n-InGaAs layers were doped at 1.0×10^{18} to increase the fabrication process flexibility by allowing bottom metal deposition on either layer.

Table 3.1: Diode III-V layers

Description	Material	Thickness (nm)	Doping (cm^{-2})
Substrate	InP	–	nid
Buffer	InP	500	nid
Growth transition	InGaAsP (1.15 μm)	5	nid
Etch stop	$\text{In}_{0.53}\text{Ga}_{0.47}\text{As}$	50	nid
Transition	<i>p</i> -InGaAsP (1.15 μm)	5	1.5×10^{18}
Sacrificial	<i>p</i> -InP	20	1.5×10^{18}
Transition	<i>p</i> -InGaAsP (1.15 μm)	5	1.5×10^{18}
Top <i>p</i> -contact	<i>p</i> - $\text{In}_{0.53}\text{Ga}_{0.47}\text{As}$	200	$>1 \times 10^{19}$
Transition	<i>p</i> -InGaAsP (1.15 μm)	5	1.5×10^{18}
Top <i>p</i> -clad	<i>p</i> -InP	2400	1.5×10^{18}
Top SCH	InGaAsP (1.15 μm)	200	nid
Active core	4 QWs and 5 Barriers	78	–
Bottom SCH	InP	30	nid
Bottom clad	<i>n</i> -InGaAs	150	1.0×10^{18}
Transition	<i>n</i> -InGaAsP (1.15 μm)	5	1.0×10^{18}
Bottom <i>n</i> -contact	<i>n</i> -InP	385	1.0×10^{18}
Bonding SL	InGaAsP (1.15 μm)	7.5	nid
Bonding SL	InP	7.5	nid
Bonding SL	InGaAsP (1.15 μm)	7.5	nid
Capping layer	InGaAs	200	nid

Ultimately the *n*-InP contact was used as the bottom contact, while the *n*-InGaAs contact served as a lower cladding layer. This cladding layer was much thicker than necessary, separating the silicon waveguide from the active core. In future generations of these lasers, the bottom *n*-InGaAs layer will be removed which is expected to improved overall laser performance.

The SOI platform was applied for this work, which is still suitable for wavelengths near 2.0 μm . Figure 3.1 shows a schematic cross-section of the laser gain region, where a broad-area III-V mesa is bonded onto the silicon waveguide. The lasers were integrated above 500-nm thick, partially etched Si rib waveguides. The hybrid optical mode is laterally confined by the silicon waveguide, while a portion of the mode overlaps the III-V

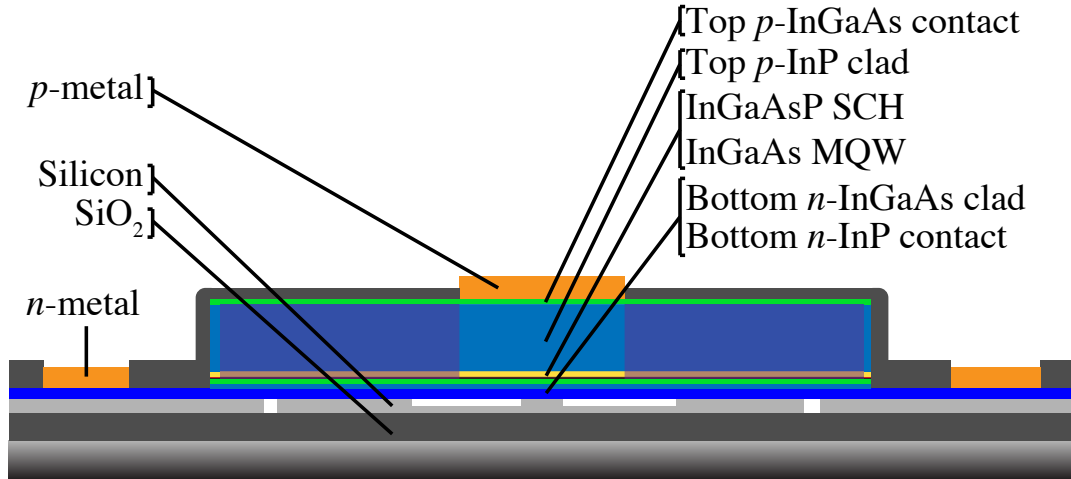


Figure 3.1: Cross-sectional schematic of the hybrid III-V/Si active region of a heterogeneously integrated $\lambda \approx 2.0 \mu\text{m}$ laser.

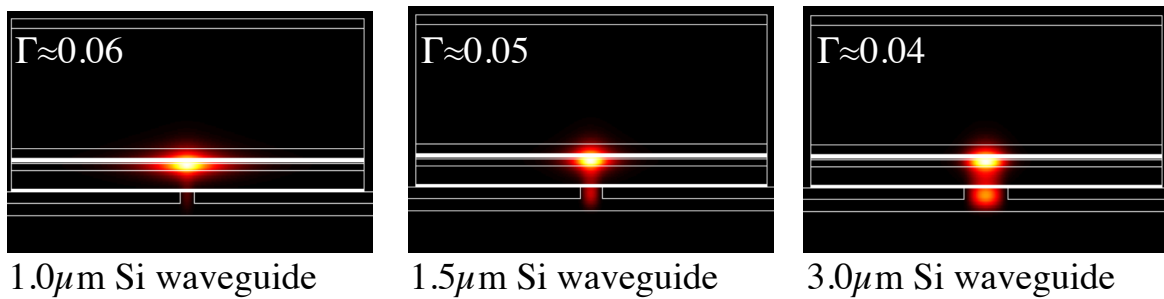


Figure 3.2: Simulated optical mode profiles and estimated MQW optical confinement factor of hybrid III-V/Si active region for various silicon waveguide widths of a heterogeneously integrated $\lambda \approx 2.0 \mu\text{m}$ laser.

multiple quantum well (MQW) active region. The confinement factor in the III-V active region depends on the silicon waveguide dimensions. Figure 3.2 shows simulated optical modes for various waveguide widths, along with corresponding estimated confinement factors in the quantum well region.

The III-V mesa is terminated on both sides by a lateral tapering of the III-V material to a point, causing the hybrid active mode to couple into a passive silicon waveguide mode. A Fabry-Perot cavity is then formed by the polished silicon facets. Figure 3.4 shows a top view of the laser layout.

The devices were designed with either 1 mm- or 2 mm- long active hybrid silicon/III-V sections. The *p*-InGaAs contact layer, cladding layers, separate confinement heterostructure (SCH) layers, and active layers were tapered over a 20 μm length, while the lower *n*-InP contact was tapered in a separate short transition. In most devices, the III-V mesa was 24 μm wide and proton implantation was used to form a current channel to prevent current spreading and ensure overlap of the carriers with the optical mode. Lasers with 2mm-long active regions had current channels ranging from 4 to 6 μm wide. Lasers with 1mm long active regions had only 4 μm -wide current channels, and some employed a narrower (4-12 μm) III-V mesa. Mesas of width 6 μm or less were not implanted.

Fabrication

Due to the longer wavelength, the III-V material stack of these devices was slightly thicker than is typical for NIR lasers. The 2.4- μm thick upper cladding was etched with a methane-hydrogen-argon (MHA) reactive ion etch (RIE) which was stopped with a laser monitor near the bottom of the InP layer. The field etch depth was then planarized with a selective HCl:H₃PO₄ (1:3) wet etch which stopped on the InGaAsP SCH layer above the active region. The remaining multiple quantum well (MQW) active region and lower

cladding layers were then etched with another MHA etch step which stopped within the bottom InP contact layer.

The III-V material was bonded to the SOI by plasma-assisted wafer bonding, followed by annealing at 300 °C for 60 minutes [106]. The InP substrate was removed by mechanical lapping and a 3:1 HCl:H₂O wet etch that stopped at a 50nm InGaAs etch stop layer. III-V mesas were defined in three steps. First, the mesas were etched with a methane-hydrogen-argon (MHA) recipe in a reactive ion etcher (RIE), and stopped near the bottom of the p-InP cladding layer. Second, in order to improve the etch-depth uniformity, an intermediate selective 1:3 HCl:H₃PO₄ wet etch step was used to remove any remaining InP and leave a level InGaAsP surface. Third, another MHA step etched through the active region and stopped in the n-InP contact layer. Pd/Ge/Pd/Au was deposited on the n-InP to form bottom contacts, and Pd/Ti/Pd/Au was deposited on the p-InGaAs to form top contacts. Current channels, seen in Figure 3.1, were formed by proton implantation with energies ranging from 10 keV to 260 keV.

Often with heterogeneously integrated lasers for 1.55 μm , the quantum wells and barriers are etched with a selective wet etch, which undercuts the active region [65]. Because the quantum wells are relatively thin, this undercut can be performed controllably, allowing a narrow taper tip to be defined for the quantum well layers. Due to the composition of the SCH and quantum wells, this customized 2.0 μm laser process featured a dry etch through the active region. The result of this

Figure 3.3 illustrates a simplified process flow diagram. A CF₄/SF₆/Ar inductively coupled plasma (ICP) dry etch defined the silicon waveguides. The actual waveguide etch depth was measured to be about 235-240 nm. To aid in bonding, vertical channels were etched through the silicon device layer to the buried oxide [107].

The fabricated dies were diced into laser bars and the silicon facets were polished but not coated. The resulting Fabry-Perot cavities contained passive silicon waveguide

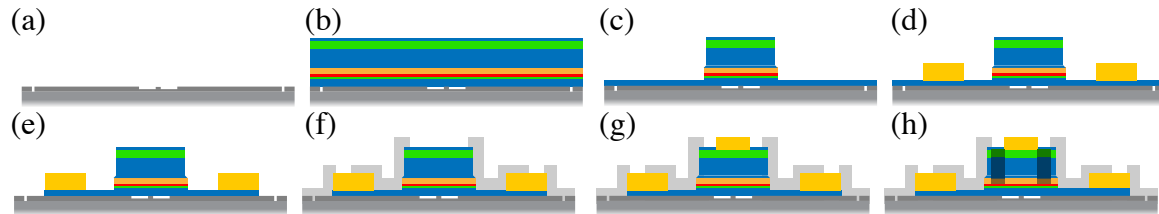


Figure 3.3: Process flow of a heterogeneously integrated $\lambda \approx 2.0 \mu\text{m}$ laser: (a) Silicon waveguide and vertical channel etch. (b) III-V bonding and substrate removal. (c) Mesa dry and wet etch steps. (d) n-Metal deposition. (e) n-InP etch. (f) SiO_2 deposition and via etch. (g) p-Metal deposition. (h) Proton implantation.

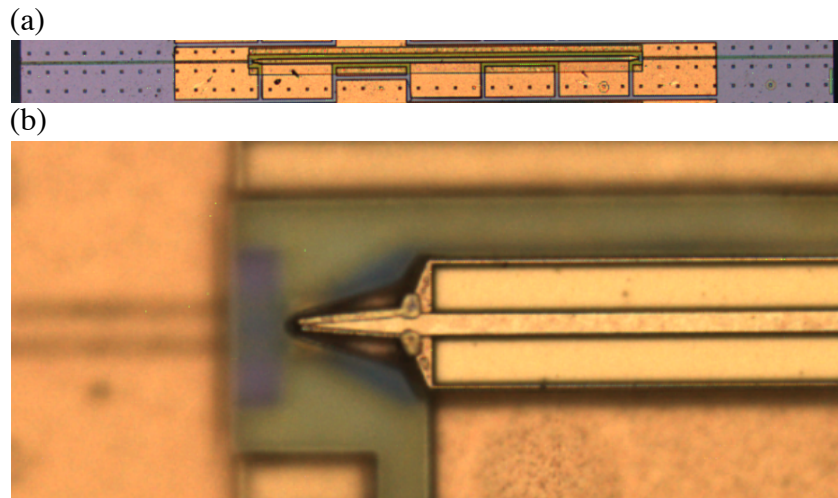


Figure 3.4: Optical microscope images of (a) a fully-fabricated $\lambda \approx 2.0 \mu\text{m}$ laser on silicon with a 1-mm-long III-V mesa (b) a lasers III-V taper region.

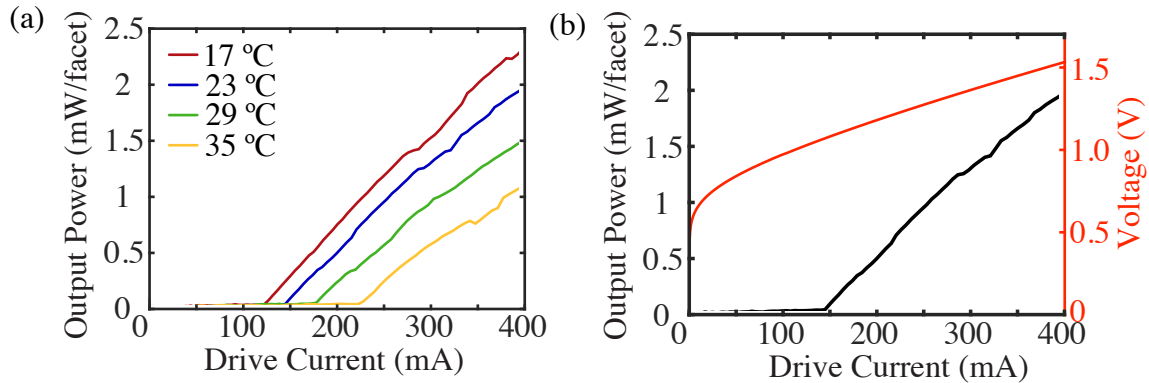


Figure 3.5: Light intensity versus current at four temperatures for a laser with 2-mm-long mesa, 4- μm -wide current channel, and 1.5- μm -wide silicon waveguide. Inset: current versus voltage for this device at 23C.

regions of length 450-650 μm on each side of the active hybrid mesas. A top-down optical microscope image of a fully-fabricated laser bar and the III-V taper can be seen in Figure 3.4.

Results

The laser bars were mounted with thermal paste on a copper block for testing. The temperature was maintained with a thermoelectric cooler and water-cooling system. An integrating sphere and Thorlabs detector (DET10D) were used to capture the light and measure the output power. The measurements were calibrated by focusing light from one device through an NA=0.85 aspherical lens directly onto the DET10D detector. Because the coupling loss could not be precisely determined, the absolute power produced by the lasers may be slightly higher than the reported values.

Initially, a total of 50 lasers were measured. Figure 3.5 shows the output power versus current characteristics for a laser with a 2mm-long mesa at four temperatures spanning 17–35 °C. Continuous wave operation was observed up to 26 °C and 35 °C for devices with 1 mm- and 2 mm-long mesas, respectively. The best performing devices, as shown in

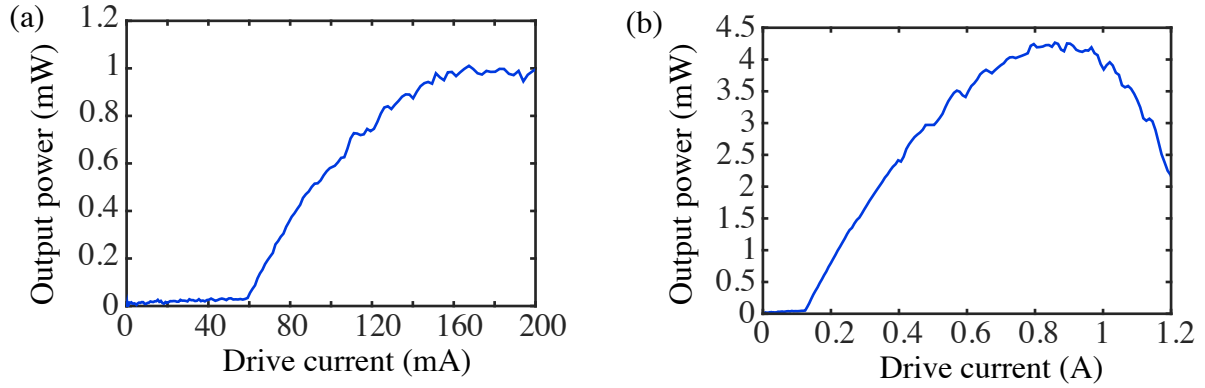


Figure 3.6: Light intensity vs. drive current for the best performing devices. (a) A laser with a 1-mm-long and $6\text{-}\mu\text{m}$ -wide III-V mesa, $4\text{-}\mu\text{m}$ -wide current channel, and $1.5\text{-}\mu\text{m}$ -wide silicon waveguide. The threshold current is 59 mA. (b) A laser with a 2-mm-long and $24\text{-}\mu\text{m}$ -wide III-V mesa, $4\text{-}\mu\text{m}$ -wide current channel, and $2\text{-}\mu\text{m}$ -wide silicon waveguide. The maximum output power is 4.2 mW.

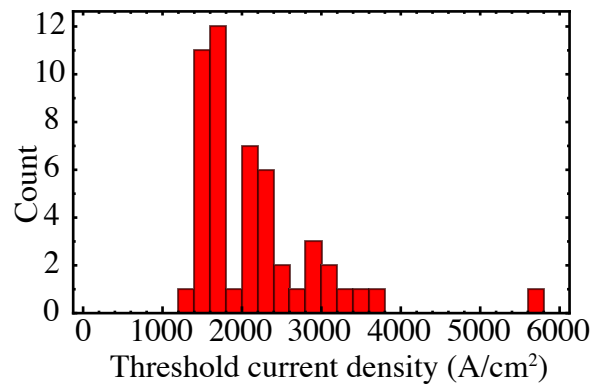


Figure 3.7: Histogram of the threshold current density at $20\text{ }^{\circ}\text{C}$ for 50 heterogeneously integrated $\lambda \approx 2.0\text{ }\mu\text{m}$ of various geometries.

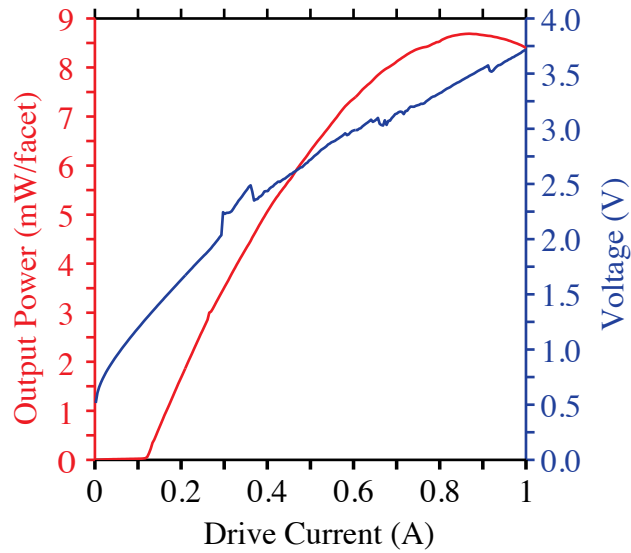


Figure 3.8: Continuous-wave (CW) single-sided output power versus drive current of a heterogeneously integrated $\lambda \approx 2.0 \mu\text{m}$ laser, showing a maximum of 8.7 mW at 20 °C.

Figure 3.6, had threshold currents as low as 59 mA and a maximum single-sided output power as high as 4.2 mW at 20 °C. The threshold current densities across all devices ranged from about 1280 A/cm² to 5710 A/cm². The histogram in Figure 3.7 shows that only 2 of the 50 devices had thresholds exceeding 3600 A/cm². Wall plug efficiencies up to 0.6% were measured.

More recent additional measurements show over 8-mW of power output from a similar device. Figure 3.8 shows the light emission vs. drive current for this laser with a 2- μm wide Si waveguide, a 24- μm wide III-V mesa, and a 5- μm wide current channel.

Figures 3.9 and 3.10 plot threshold currents and output powers vs. silicon waveguide width at 20°C for 2mm- and 1mm-long mesas, respectively. The performance variation of lasers with identical design geometries is attributed to fabrication non-uniformity. Of the lasers with 24 μm -wide mesas, those with wider silicon waveguides up to 2 μm performed best overall with lower threshold currents and higher maximum output powers. However, no further improvement was observed when the silicon waveguide width was increased

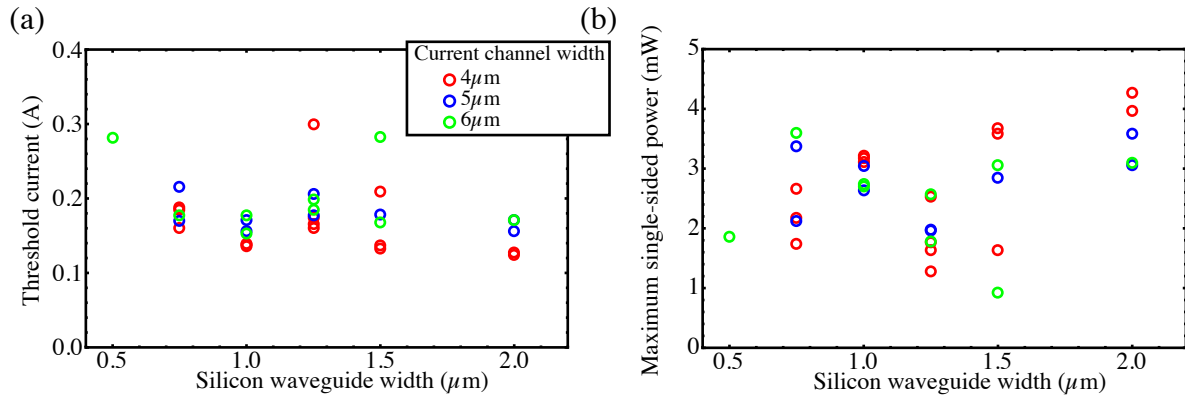


Figure 3.9: Dependence of threshold current and maximum single-sided output power on silicon waveguide width for heterogeneously integrated $\lambda \approx 2.0 \mu\text{m}$ lasers with 2-mm-long III-V mesas.

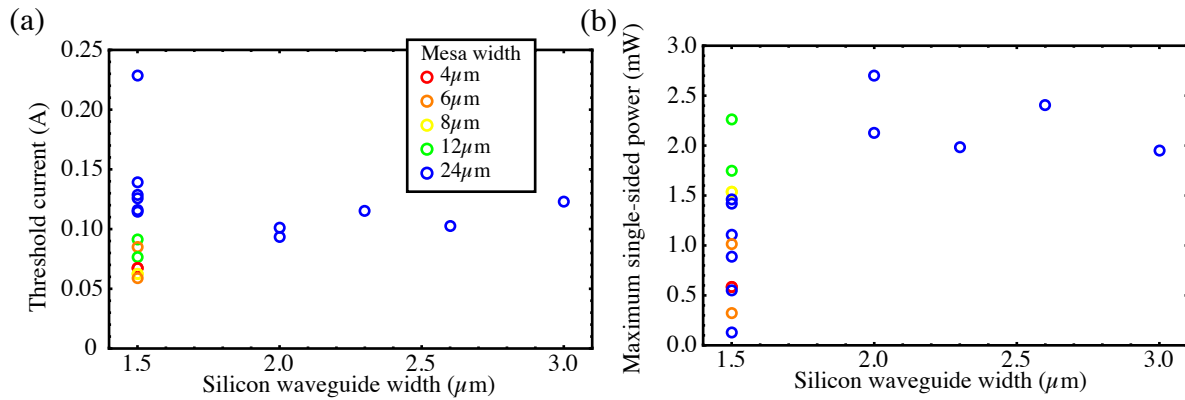


Figure 3.10: Dependence of threshold current and maximum single-sided output power on silicon waveguide width for heterogeneously integrated $\lambda \approx 2.0 \mu\text{m}$ lasers with 1-mm-long III-V mesas.

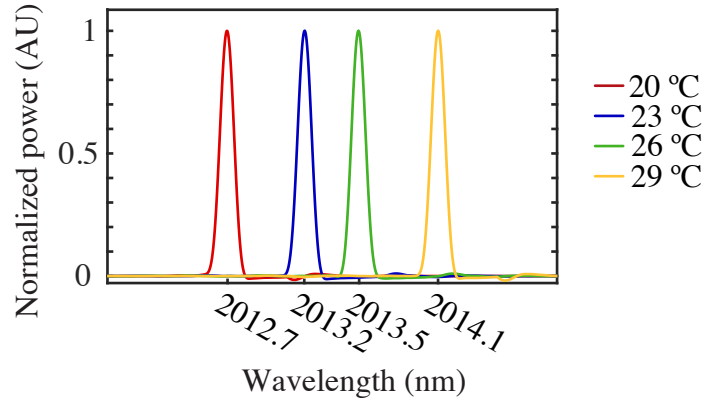


Figure 3.11: Normalized optical spectra at various temperatures for a heterogeneously integrated $\lambda \approx 2.0 \mu\text{m}$ laser with a 2-mm-long III-V mesa. Peak wavelengths are indicated on the horizontal axis.

beyond $2\mu\text{m}$. As seen in Figure 3.2, the mode profile for thinner silicon waveguides extends further laterally from the center of the III-V mesa. While this geometry provides higher total optical confinement in the quantum wells, the modal gain is reduced due to a decreased modal overlap with the carrier density distribution near the center of the mesa. This tradeoff causes a peak net gain value for $2\mu\text{m}$ wide silicon waveguides.

There was no consistent significant correlation between ion implanted current channel width and device performance; however, the devices with narrow III-V mesas showed the lowest threshold currents. Because the narrow mesa provides improved modal overlap with the carrier density distribution, the modal gain is higher in these devices. However, this improvement over the proton-implanted current channels comes at the expense of reduced thermal dissipation, hence the maximum output power does not improve compared to the wide-mesa design.

The emission spectra were measured by collimating the output and coupling in free-space into a Bruker Vertex 70 FT-IR spectrometer. Figure 3.11 shows the spectra for a 2 mm-long device at four temperatures ranging from 20 to 29 °C. The peak wavelength at 20 °C is 2012.7 nm with a FWHM linewidth <0.2 nm and the wavelength shift with

temperature is $0.15 \text{ nm}/^\circ\text{C}$. The single-longitudinal-mode behavior is attributed to the tendency of reflections from the III-V tapers to form multiple coupled longitudinal cavities, in addition to the primary lasing cavity defined by the polished silicon facets. In many cases this caused the devices to lase in a single longitudinal mode, although multiple modes were seen at other drive currents and temperatures. Mode hopping also occurred sometimes as the operating conditions changed. While typically the lasing mode was $2.01 \mu\text{m}$, different devices and operating conditions produced wavelengths ranging from 1986 nm to 2033 nm . In future runs, it should be possible to minimize the wavelength non-uniformity by improving both the processing and design of the tapers.

Finite difference time domain (FDTD) simulations suggest that the reflectivity of the taper tip is near -18 dB . This can be addressed by reducing the $1.5\text{-}\mu\text{m}$ width of the active region taper tip.

3.2 Semiconductor Optical Amplifiers for $2.0 \mu\text{m}$

The same gain structures can also be used in an SOA configuration [73], where the active region is not within a laser cavity.

An anti-reflective coating was applied the silicon waveguide end-facets of the lasers and light from an external tunable laser emitting near $2.0\text{-}\mu\text{m}$ was injected with a lensed fiber to test the gain properties of these devices. The SOA emission was collected with another lensed fiber from the opposite silicon facet, and monitored with an optical spectrum analyzer.

For $2.01\text{-}\mu\text{m}$ light, on-chip gain with a peak value of over 13 dB and 3-dB bandwidth of $\sim 75 \text{ nm}$ was observed at 20°C . These SOAs operated up to 50°C . Figure 3.12(a) shows the on-chip gain as a function of drive current for an SOA pumped with wavelengths in the range $2.01\text{--}2.06 \mu\text{m}$, while Figure 3.12(b) shows the on-chip gain as a function of

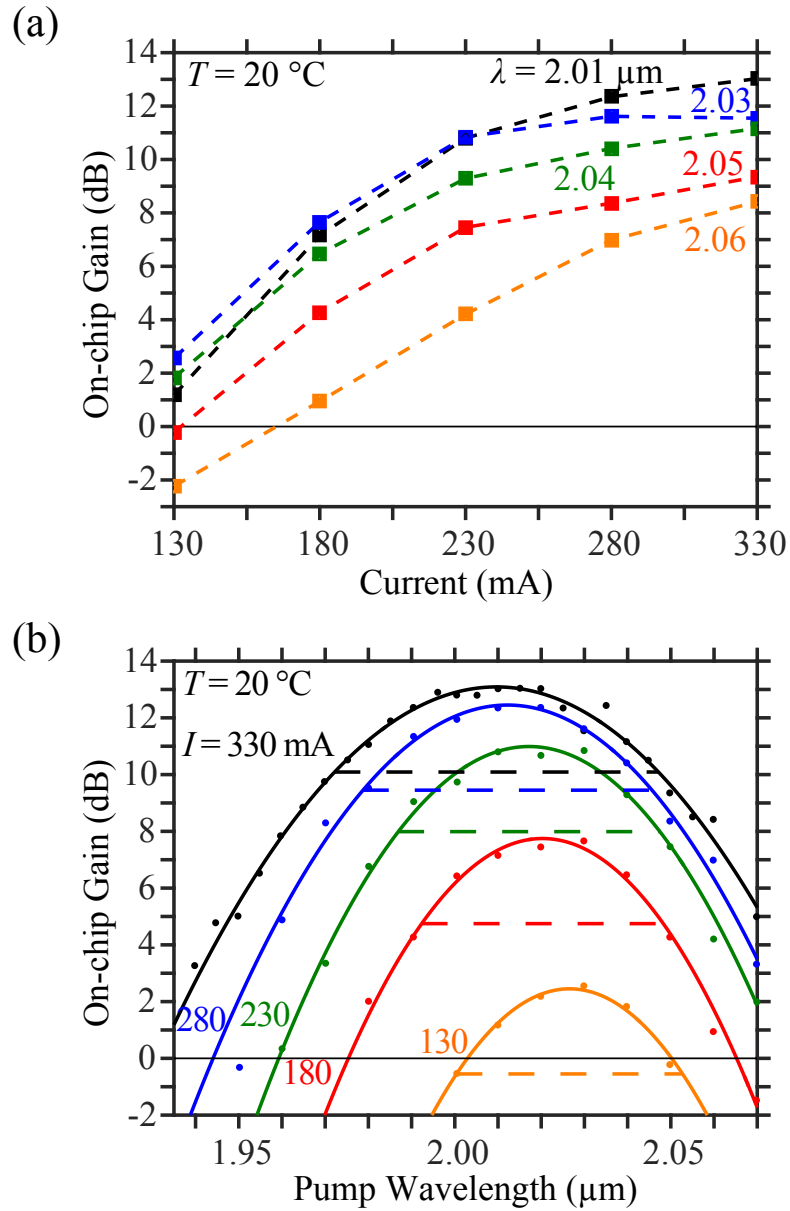


Figure 3.12: On-chip gain measured at 20°C for an integrated $2\text{-}\mu\text{m}$ SOA (a) vs. the drive current for wavelengths from $2.01\ \mu\text{m}$ to $2.06\ \mu\text{m}$ and (b) vs. the pump wavelength for drive currents from $130\ \text{mA}$ to $330\ \text{mA}$.

wavelength for various drive currents.

The dashed lines in 3.12(b) indicate the 3-dB bandwidth of the gain, while the solid curves indicate a fitting with the theoretical spectral dependence of the on-chip gain, $G(\lambda)$. $G(\lambda)$ at a fixed temperature and current can be described by [108, 73]

$$G(\lambda) = G_p e^{-A(\lambda - \lambda_p)^2}$$

$$G_p \equiv e^{g_{net}(\lambda_p)L}$$

where g_{net} is the net modal gain, L is the length of the gain region, and λ_p is the peak gain wavelength. A is a fitting parameter which depends on L , transverse active region confinement Γ , and material gain, g .

3.3 Conclusion and Summary

We have demonstrated room temperature, continuous wave, heterogeneously integrated Si/III-V lasers operating near $2.0\mu\text{m}$, sometimes in a single spectral mode. The devices function up to $35\text{ }^\circ\text{C}$, produce up to 8.7 mW of CW single-sided power, have threshold currents as low as 59 mA , and are heterogeneously integrated with silicon waveguides. This gain material has been used in an SOA configuration, generating over 13 dB gain near $2.01\text{ }\mu\text{m}$ at room temperature with a 3-dB bandwidth of 75 nm .

Chapter 4

Quantum Cascade Lasers on Silicon

QCLs are most commonly grown on either InP or GaAs substrates. For operation in 4–10 μm wavelength range, the best performing lasers use the InGaAs/InAlAs system, lattice-matched to an InP substrate. While GaAs lasers have been successfully heterogeneously integrated on silicon for near-infrared wavelengths, we first focused on integrating an InP-based QCL for operation at $\lambda \approx 4.8 \mu\text{m}$.

This work is published in [77, 78].

UCSB: *A. Spott, J. Peters, M. Davenport, E. Stanton, C. Zhang, and J. Bowers.* A. Spott designed the devices, fabrication process, and mask, and performed the initial laser characterization and facet polishing. J. Peters fabricated the lasers. The team at UCSB contributed to the laser design, fabrication process design, and data interpretation.

US Naval Research Laboratory: *C. Merritt, W. Bewley, I. Vurgaftman, C.S. Kim, and J. R. Meyer.* The team at NRL aided in the laser design and data interpretation, and performed the laser characterization measurements included in this Chapter.

University of Wisconsin: *J. Kirch, L. Mawst, and D. Botez.* The team at University of Wisconsin performed the MOCVD growth of the QCL material and contributed

to the III-V material design.

4.1 SONOI, SOI, and SON Platform

The first QCLs demonstrated were fabricated on the SONOI waveguide platform (overviewed in Chapter 1.4) in order to establish an ultra-broadband platform which supports SiN-on-SiO₂ waveguides for shorter wavelengths in addition to the silicon waveguides that the lasers were constructed upon. Additional QCLs have also been constructed on the traditional SOI waveguide platform. In both cases, a 1500 nm device layer was chosen. The thicker waveguide was expected to reduce propagation loss by limiting the optical confinement in the surrounding cladding layers.

The SONOI waveguide platform is not commercially available and must be constructed from a customized die-bonding process, which will be discussed later. The custom process allows the flexibility to choose the cladding layer thicknesses. The cladding layers must be thick enough to avoid loss due to mode leakage into the high-index silicon substrate. Figure 4.1(a) shows the substrate leakage loss of the fundamental TM₀₀ mode in a 1.5 μm -tall and 2.0 μm -wide SONOI waveguide as a function of the underlying buried SiO₂ thickness for a 400 nm-thick SiN layer and a 700 nm-thick SiN layer. Intuitively, a thicker SiO₂ layer is necessary for the thinner SiN layer. In either case, a 600 nm-thick SiO₂ layer is sufficient to prevent mode leakage. Our SONOI platform used a 3 μm -thick SiO₂ layer, which conservatively ensures that no substrate leakage occurs. This thicker SiO₂ layer does introduce a thermal disadvantage as (discussed in Chapter 4.4) and could be thinned in future generations. Figure 4.1(c) shows the simulated optical mode intensity of the fundamental TM₀₀ mode used in the SONOI waveguide.

If SiN-on-SiO₂ waveguides are not necessary, SON waveguides can be used instead. Figure 4.1(b) shows the fundamental TM₀₀ mode in a 1.5 μm -tall and 2.0 μm -wide SON

waveguides as a function of the SiN thickness, where no SiO₂ is present. A 1.0–1.2 μm thick SiN layer is necessary to avoid substrate leakage loss. This waveguide platform will likely be used in future generations of devices, where the application focus is entirely on the mid-infrared. Removing the SiO₂ layer also has thermal benefits, (discussed in Chapter 4.4).

The Si₃N₄ was deposited by Rogue Valley Microdevices by low pressure chemical vapor deposition (LPCVD). A stoichiometric Si₃N₄ was chosen with the expectation that the optical loss would be lower than a non-stoichiometric SiN film (see Chapter 1.4). Although the thickness of stoichiometric LPCVD-deposited Si₃N₄ films is typically limited to $\sim 400\text{--}450$ nm due to film stress, other compositions of SiN can be deposited with lower stress either in place or of, or in combination with, the stoichiometric Si₃N₄. This is particularly necessary for SON waveguides where at least 1000 nm SiN is necessary.

4.2 Fabry-Perot QCLs on SONOI

Laser Design

A top-view optical microscope image of a fabricated laser is shown in Figure 4.2. Each laser consists of a 4 mm long hybrid silicon-QCL active region coupled to passive silicon waveguide regions at each side. Tapered III-V mesas are designed to couple light between the hybrid silicon-QCL mode and a passive silicon waveguide mode. A Fabry-Perot cavity is then formed by uncoated, polished silicon waveguide facets, one of which is shown in the scanning electron microscope (SEM) image in Figure 4.3. It is also possible to obtain feedback from gratings (DFB or DBR) or loop mirrors, as we have done successfully at shorter wavelengths [1]. DFB QCLs are discussed later, in Section 4.3 [78].

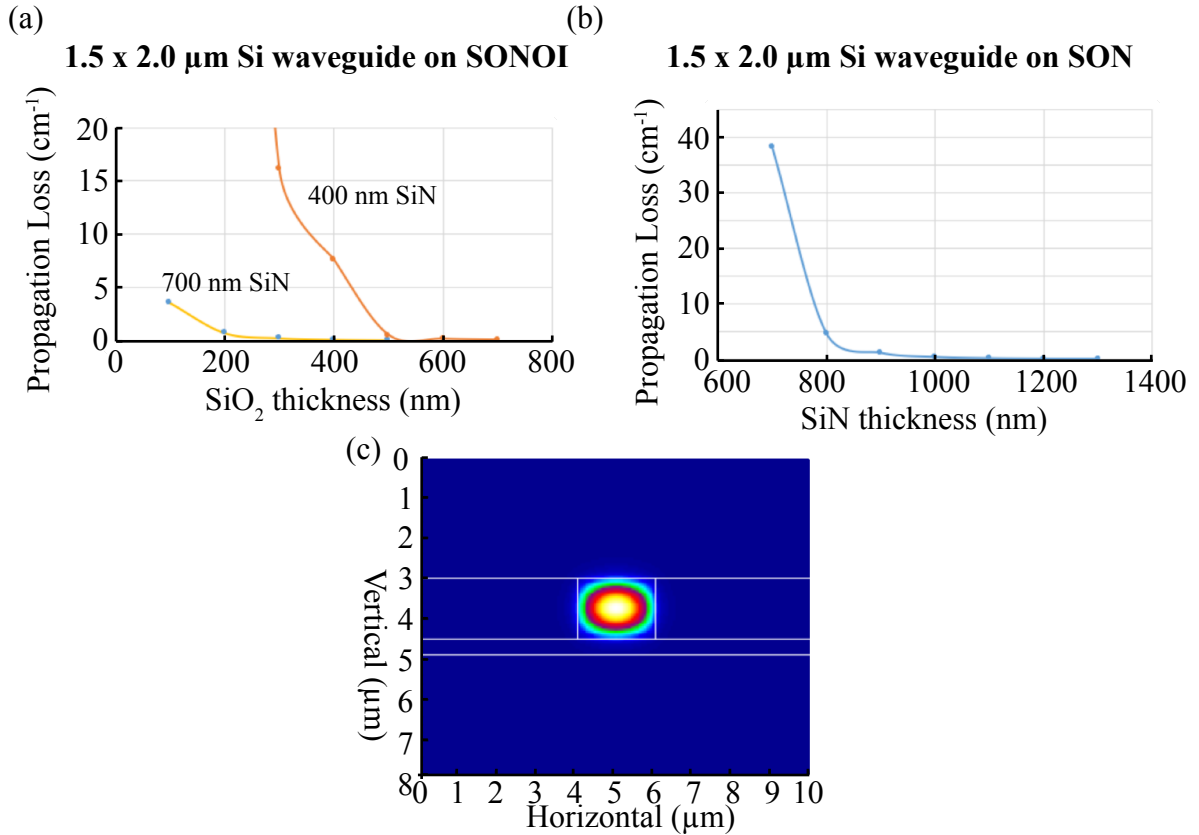


Figure 4.1: Loss due to substrate leakage for a 1.5 μm-tall and 2.0 μm-wide silicon waveguide for (a) SONOI, as a function of the buried SiO₂ thickness and (b) SON, as a function of the buried SiN layer. (c) A FIMMWAVE simulation of the electric field intensity of the TM mode of a 1.5 μm × 2.0 μm SONOI waveguide.

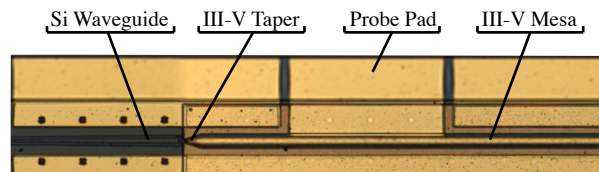


Figure 4.2: Optical microscope image of an integrated QCL on silicon.

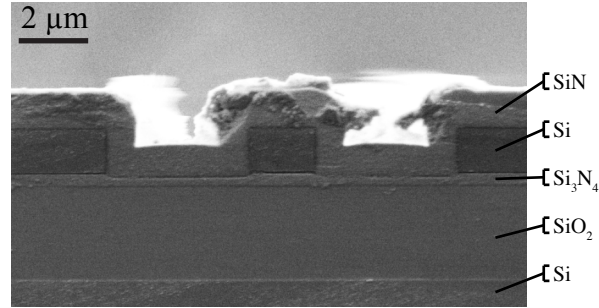


Figure 4.3: Polished SONOI end-facet of an integrated QCL.

Table 4.2: QCL III-V layers

Description	Material	Thickness (nm)	Doping (cm ⁻²)
Substrate	InP	–	–
Etch stop	InGaAs	50	–
Top contact	<i>n</i> -InP	1500	5 × 10 ¹⁸
Top clad	<i>n</i> -InP	50	5 × 10 ¹⁷
Top clad	<i>n</i> -InP	50	1 × 10 ¹⁷
Top clad	<i>n</i> -InP	2450	2 × 10 ¹⁶
Transition	<i>n</i> -InGaAs/InAlAs	50	1 × 10 ¹⁷
Active core	<i>n</i> -QC structure	1510	Variable
Transition	<i>n</i> -InGaAs/InAlAs	50	1 × 10 ¹⁷
Bottom clad	<i>n</i> -InP	50	1 × 10 ¹⁷
Bottom clad	<i>n</i> -InP	50	5 × 10 ¹⁷
Bottom contact	<i>n</i> -InP	200	1 × 10 ¹⁸
Bonding SL	<i>n</i> -InP	7.5	1 × 10 ¹⁸
Bonding SL	<i>n</i> -InGaAs	7.5	1 × 10 ¹⁸
Bonding SL	<i>n</i> -InP	7.5	1 × 10 ¹⁸
Bonding SL	<i>n</i> -InGaAs	7.5	1 × 10 ¹⁸
Bonding layer	<i>n</i> -InP	10	1 × 10 ¹⁸
Capping layer	<i>n</i> -InGaAs	200	1 × 10 ¹⁸

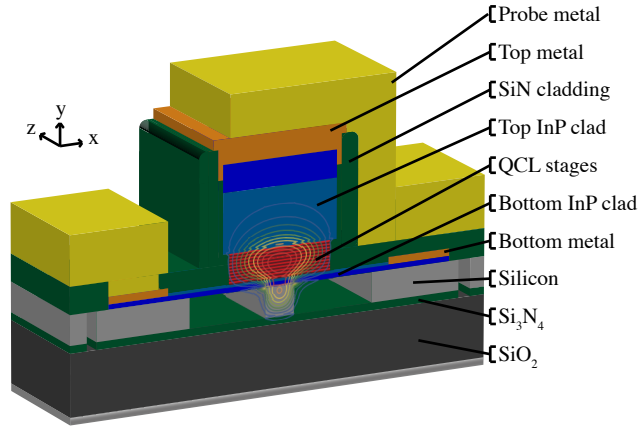


Figure 4.4: Cross-sectional schematic of an integrated QCL active region. A contour plot of the electric field component, $|E_y|$, of the simulated fundamental TM optical mode is overlaid.

The QCL material was grown by metalorganic chemical vapor deposition (MOCVD) at U. Wisconsin, with 30 active stages having a design similar to that described in [109]. A low injector-doping (estimated to be mid- 10^{11} cm^{-2}) was used to provide a low threshold current density. The surrounding layers, modified for heterogeneous integration on silicon, are shown in Table 4.2. A thick top InP cladding separates the optical mode from the contact metal, while a thin InP bottom cladding keeps the active region close to the silicon for improved efficiency of the taper mode conversion. Previous heterogeneously integrated near-infrared lasers have used alternating InP and InGaAsP layers to form a bonding superlattice (SL) which prevents defects formed at the bonded interface from propagating into the active region and degrading laser performance [110]. Here we similarly introduce a defect-blocking InP/InGaAs SL, although the impact on laser performance has not been investigated for heterogeneously integrated mid-infrared lasers (particularly QCLs or ICLs).

Figure 4.4 shows a cross-sectional schematic of the hybrid silicon-QCL region for Devices A and B discussed below. The laser geometry is designed to support light

in the transverse magnetic (TM) polarization emitted by QCLs. A simulation from FIMMWAVE of the fundamental TM mode (for $\lambda=4.8 \mu\text{m}$), which is shared between the narrow silicon waveguide and the InP QCL ridge waveguide, is shown projected onto the active region cross-section in the schematic. Mode solver simulations find the transverse confinement factor Γ_{xy} in the QCL active core, which depends on both the III-V mesa and silicon waveguide widths, to be ~ 0.76 and 0.73 for devices A and B, respectively. The effective index of the mode is 2.97 in the passive SONOI region and 3.17 in the hybrid silicon-QCL active region.

The silicon waveguides are $1.5 \mu\text{m}$ tall, with a 400 nm Si_3N_4 lower cladding and $3 \mu\text{m}$ buried SiO_2 layer. The III-V mesas for Devices A and B are $6 \mu\text{m}$ wide and their silicon waveguides in the active region are $1 \mu\text{m}$ and $1.5 \mu\text{m}$ wide, respectively. Within the taper region, the III-V mesa linearly narrows from $6 \mu\text{m}$ wide to 500 nm wide at the taper tip, although the width of the fabricated taper tip varies from device to device. The silicon waveguide expands to $6 \mu\text{m}$ wide underneath the entire III-V taper region, and is $2 \mu\text{m}$ wide in the passive regions. The III-V taper lengths are $20 \mu\text{m}$ for Device A and $45 \mu\text{m}$ for Device B. The design, impact on laser performance, and simulated performance of the III-V tapers are discussed in Chapter 6.

Two potential sources of internal loss for these devices are the optical overlap with both the 200 nm thick $1 \times 10^{18} \text{ cm}^{-3}$ doped n-InP bottom contact layer and the $3 \mu\text{m}$ thick SiO_2 cladding layer underneath the SONOI waveguide. Similar to the active region confinement, the confinement in the n-InP contact layer depends on the III-V mesa and silicon waveguide widths, and is found to be < 0.04 for both Devices. Although the free-carrier absorption in n-InP at this doping level and wavelength is not precisely known, we expect a loss contribution less than 1 cm^{-1} [111]. As with previous heterogeneously integrated lasers on silicon, the n-InP contact layer thickness and doping presents a design trade-off between electrical performance, active core confinement, and internal loss which

will be explored in future heterogeneously integrated QCL generations.

The overlap of the fundamental TM mode with the lower SiO₂ cladding was estimated by simulations to be 4.4×10^{-3} for the 2 μm wide passive SONOI waveguides, and $<3.4 \times 10^{-5}$ for the hybrid silicon-QCL active region of Devices A and B. This suggests a propagation loss contribution for the SiO₂ at 4.8 μm (using an estimated loss of 200 dB/cm [112]) of <1.0 dB/cm in the passive waveguide section and insignificant in the active region. A lower Si₃N₄ cladding thicker than 400 nm may be necessary to support extremely low loss SONOI waveguides or lasers emitting at longer wavelengths where the SiO₂ absorption becomes higher. Leakage into the silicon substrate is found to be negligible due to the sufficient SiO₂ thickness of 3 μm .

Fabrication

The SONOI waveguide platform is constructed by transferring the device layer from a silicon-on-insulator (SOI) wafer onto a nitride-on-insulator (NOI) wafer by direct wafer bonding. Each NOI wafer purchased from Rogue Valley Semiconductor consists of a silicon substrate with a 3 μm thermally grown SiO₂ layer and 400 nm stoichiometric Si₃N₄ layer deposited on both top and bottom. The SOI wafer consists of a 1.5 μm Si device layer, a 1 μm buried SiO₂ (BOX) layer, and a Si substrate.

Figure 4.5 shows the process flow used to fabricate the SONOI waveguide. Vertical outgassing channels (VOCs) are etched through the Si₃N₄ and SiO₂ layers of the NOI chip. An SOI chip is then bonded after a plasma surface activation. The resulting chip is annealed in a graphite bonding fixture at 300 °C for 2 hours, then further annealed in a tube furnace at 900 °C for 4 hours (with a 600 °C overnight idling). After bonding, the Si substrate is removed from the SOI chip by mechanical lapping and an inductively coupled plasma (ICP) C₄F₈/SF₆/Ar etch, whose rate slows once it reaches the SiO₂. The

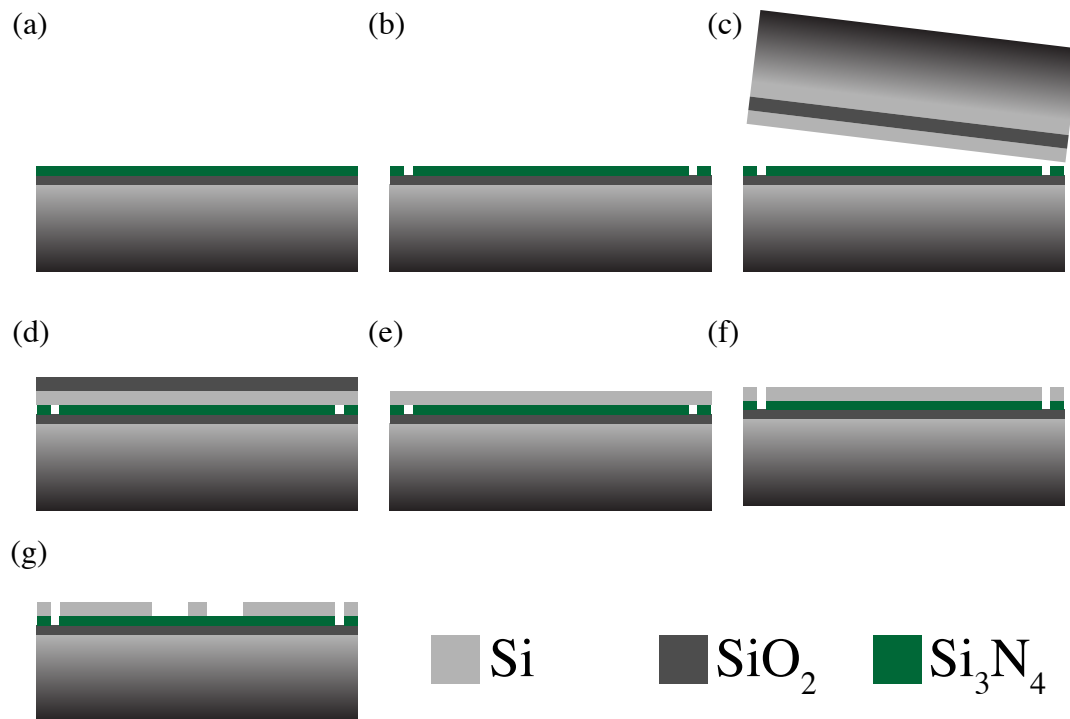


Figure 4.5: Fabrication steps of the SONOI waveguides. (a) Begin with the NOI chip. (b) Dry etch the vertical outgassing channels through the Si_3N_4 and into the SiO_2 . (c) Bond the SOI chip to the NOI chip. (d) Remove the Si substrate. (e) Remove the SiO_2 layer with buffered HF. (f) Dry etch the vertical outgassing channels in the Si device layer for later QCL bonding. (g) Dry etch the strip waveguides.

SiO₂ layer is then removed with buffered HF to leave the SONOI chip. Finally, VOCs for QCL bonding and the strip waveguides are fully etched with C₄F₈/SF₆/Ar ICP etches.

Figure 4.6 illustrates the QCL fabrication process. It begins by flip-chip bonding the QCL material to the SONOI chip after removing the capping layer (with an H₃PO₄:H₂O₂:DI 1:1:38 wet etch) and plasma activation. The InP substrate is removed by mechanical lapping and an HCl:DI 3:1 wet etch that selectively stops on an InGaAs etch stop layer.

The QCL mesa is defined with an SiO₂ hard mask. The InP top cladding is etched with a CH₄/H₂/Ar reactive ion etch (RIE) and stopped at the QCL active region with laser endpoint detection. The QCL active region is removed with an H₃PO₄:H₂O₂:DI 1:5:15 wet etch. In order to reduce undercutting of the QCL layers, this etch is performed in multiple steps consisting of repeated stripping and re-patterning of the photoresist. Pd/Ge/Pd/Au (10/110/25/1000 nm) is deposited for both the top and bottom contacts. Before the bottom contact metal is deposited, the bottom cladding is etched with a short RIE to reveal the 200 nm, highly doped n-InP bottom contact layer. Transmission line measurements estimated the sheet resistance of this layer to be 60-70 Ω/sq, suggesting that the total series resistance contribution of the lateral current travel on both sides of the mesa is less than 0.1 Ω. 1200 nm PECVD SiN is deposited as an electrical isolation layer, and vias are etched prior to depositing the top contact and probe metals. Laser bars are diced from the chip and the SONOI facets are mechanically polished.

Results

After fabrication, the silicon laser bar substrate was bonded with GE varnish to a copper sub-mount and the probe pads were contacted with wire bonds to inject current. The lasers were driven with a pulsed current source that produced 250 ns wide pulses at

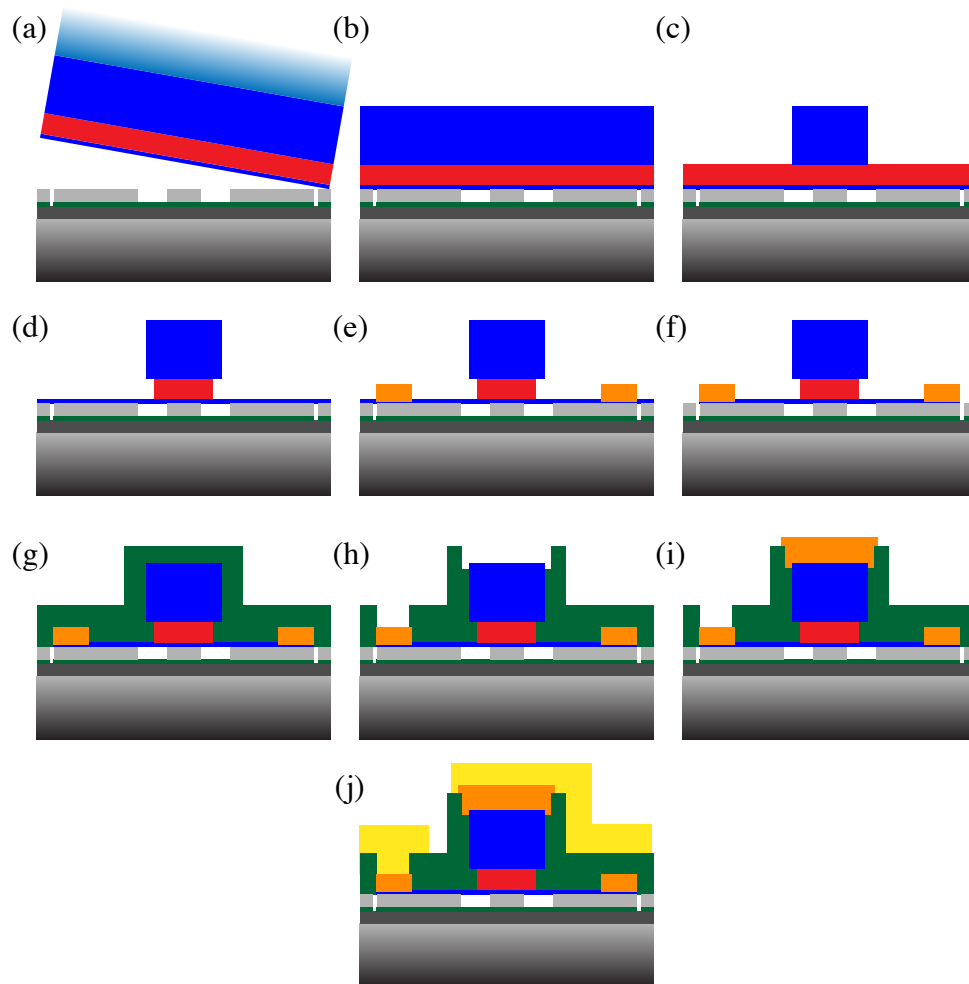


Figure 4.6: Steps to fabricate the integrated QCLs on silicon. (a) Bond the QCL material to the SONOI chip. (b) Remove the InP substrate. (c) Dry etch the top InP cladding. (d) Wet etch the QCL active stages. (e) Deposit n-metal for the bottom contact. (f) Dry etch the bottom InP cladding. (g) Deposit a SiN cladding by PECVD. (h) Dry etch vias. (i) Deposit n-metal for the top contact. (j) Deposit the probe metal.

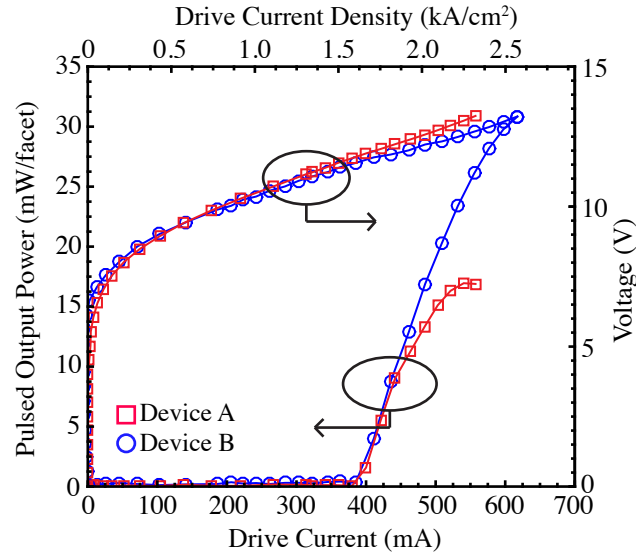


Figure 4.7: Single-sided pulsed optical output power and voltage versus drive current of two $\lambda \approx 4.8 \mu\text{m}$ QCLs-on-SONOI with 4 mm-long active regions and $6 \mu\text{m}$ -wide III-V mesas. The silicon waveguides of Devices A and B are $1 \mu\text{m}$ and $1.5 \mu\text{m}$ wide, respectively. The lasers were driven at 20°C with a pulsed current source that produced 250 ns wide pulses at a 1 kHz repetition rate. Light is collected from the polished passive SONOI facet.

a 1 kHz repetition rate for all of the measurements. The light output was collected with an $f/1$ aspheric ZnSe lens and focused onto a fast room temperature HgCdTe detector with an $f/2$ aspheric ZnSe lens. Digitized scope readings were averaged from 150 - 200 ns to measure the detector voltage. A direct calibration of the measured detector voltage was obtained by operating the device at 200 kHz and measuring the output with both the above described collection and detection, and also with a 25 mm diameter thermopile detector placed directly at the device output.

The L-I-V characteristics for operation in pulsed mode at room temperature were measured for 10 integrated QCLs of varying geometries. Despite quantitative variations, the results are generally consistent qualitatively. Figure 4.7 plots the characteristics of two of the better lasers at 20°C . The threshold currents are 388 mA and 387 mA for Devices A and B, respectively, while the maximum output powers are 17 mW and 31

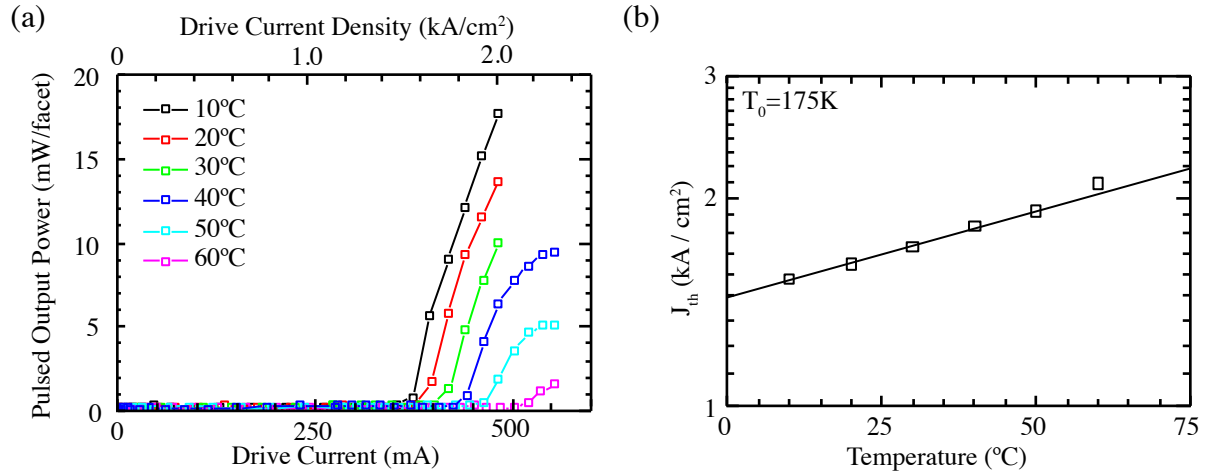


Figure 4.8: (a) Single-sided pulsed optical output power versus drive current for a $\lambda \approx 4.8 \mu\text{m}$ QCL-on-SONOI with a 4 mm-long active region, tested at temperatures from 10 °C to 60 °C. This laser (Device A) has a 6 μm wide III-V mesa and a 1.0 μm wide silicon waveguide. Light is collected from the polished passive SONOI facet. (b) Corresponding threshold current densities versus temperature. The fit yields a characteristic temperature of T_0 175K.

mW. The slope efficiency near threshold for Device A is 150 mW/A, while for Device B it is 170 mW/A. The maximum wall-plug efficiency for Device B (from one of the two uncoated SONOI facets) is 0.35%.

Figure 4.8 shows the output power emitted from Device A at a series of temperatures maintained by a thermoelectric cooler, ranging from 10 to 60 °C. Figure 4.8 plots the corresponding temperature dependence of the threshold current density obtained by dividing the threshold current by the III-V active area. The characteristic temperature T_0 was found to be 175 K by fitting the exponential function $J_{th} = J_0 \exp(T/T_0)$. This pulsed characteristic temperature is typical for a relatively low-injector-doping, 4.5–5.0 μm -emitting QCL [113] that is suitable for low-power-dissipation applications. A fit of the slope efficiency vs. temperature yields $T_1=87$ K.

As with previous heterogeneously integrated lasers on silicon, the low thermal conductivity of the buried SiO_2 layer significantly impedes heat removal from the active region,

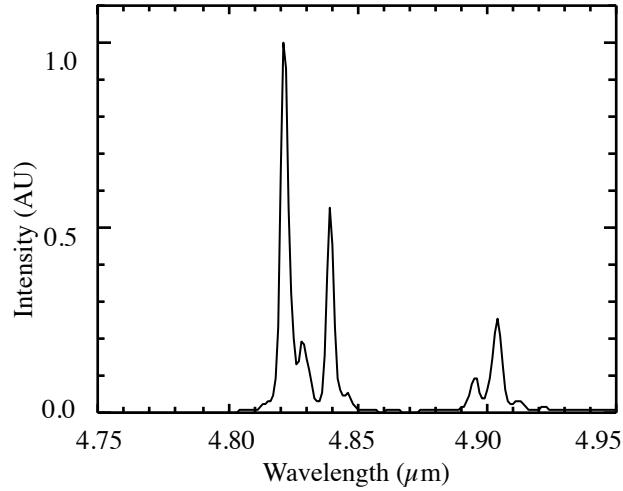


Figure 4.9: Emission spectra of Device B, a 4 mm-long $\lambda \approx 4.8 \mu\text{m}$ QCL integrated on SONOI. This device has a $6 \mu\text{m}$ -wide III-V mesa and a $1.5 \mu\text{m}$ -wide silicon waveguide. The laser was measured with a monochromator at $20 \text{ }^\circ\text{C}$.

while the GE varnish used to bond the laser bar to the copper submount introduces a further thermal barrier. However, poor heat dissipation is not a fundamental limitation. Possibilities for improvement include the introduction of a thermal shunt [114], or an epilayer-down arrangement wherein the top of the chip is bonded to a thermally conductive submount. Given the relatively low current and power density thresholds of these devices, along with their relatively high characteristic temperature, continuous-wave (CW) operation of the heterogeneously integrated QCLs at ambient temperature should be quite feasible.

Figure 4.9 shows the spectral emission from Device B at $20 \text{ }^\circ\text{C}$. The spectrum acquired with a Digikrom 0.5 m monochromator with 1.5 nm resolution indicates a peak wavelength of $4.82 \mu\text{m}$.

The solid curves in Figure 4.10 show horizontal (top) and vertical (bottom) far-field profiles of the emission from Device A. A similar profile along the slow axis was obtained for Device B (which was not measured along the fast axis). The dashed lines in the figures are FIMMWAVE simulations corresponding to the fundamental TM mode of the

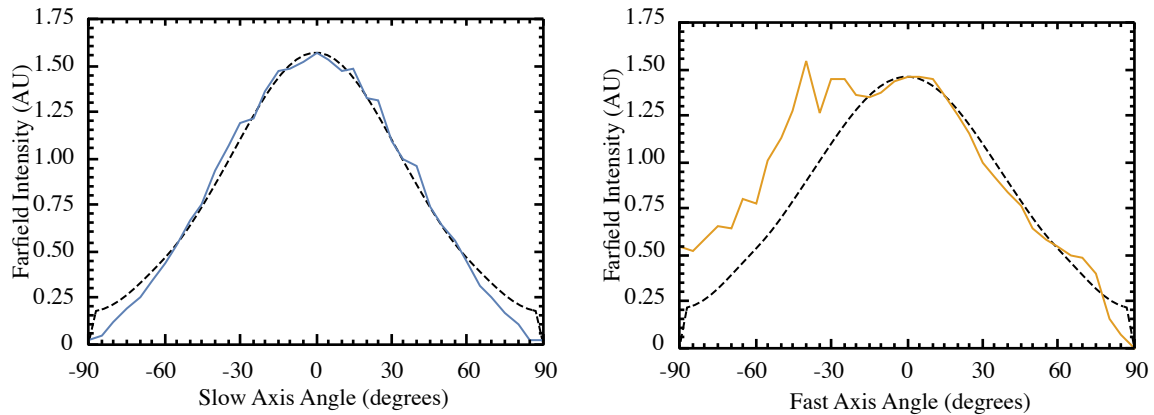


Figure 4.10: Far-field intensity of a $\lambda \approx 4.8 \mu\text{m}$ QCL integrated on SONOI with a 4 mm-long active region, as a function of the angle normal to the facet in the slow (horizontal) axis (top) and fast (vertical) axis (bottom). Solid lines indicate measurements, and dotted lines indicate simulated profiles. Measurements were taken at 20 °C and a drive current of 500 mA. This laser (Device A) had a 6 μm -wide III-V mesa and a 1.0 μm -wide silicon waveguide.

passive SONOI waveguides. That the measured profiles agree well with the simulated shapes, particularly in the horizontal direction, indicates that the QCLs emit primarily in the fundamental TM mode. The additional features at negative angles below ~ -15 degrees along the fast axis are most likely due to polishing imperfections, such as residue on the SONOI facet or the surrounding cladding. According to the simulations, a higher-order transverse TM mode in the SONOI waveguide has strong optical overlap with the QCL core in the hybrid active region. Since that mode is expected to efficiently couple through the tapers into a higher-order mode in the passive silicon waveguide, the far-field measurements imply that this higher-order mode does not reach the lasing threshold.

A seemingly-inconsistent feature of the L-I data shown in Figures 4.7 and 4.8 is that while the threshold current densities for both devices are rather low ($\sim 1.6 \text{ kA/cm}^2$), the single-facet slope efficiencies are also low (150–170 mW/A). This should not occur in a QCL, since a loss strong enough to suppress the efficiency by this amount should also substantially increase the lasing threshold. It suggests that strong feedback from

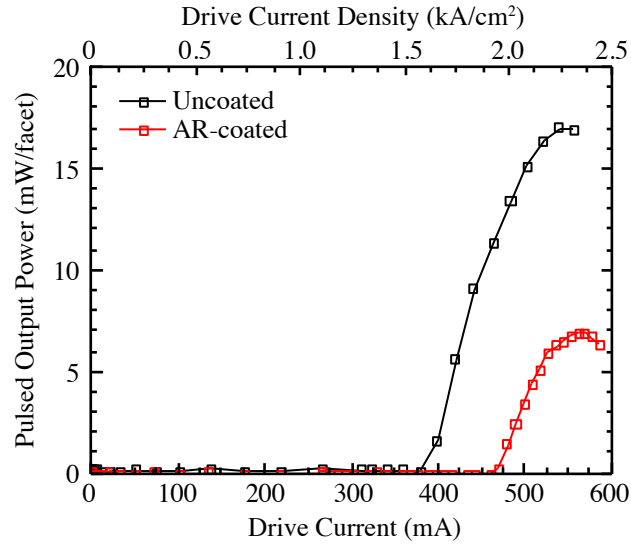


Figure 4.11: Pulsed single-sided output power versus drive current at 20 °C for a $\lambda \approx 4.8 \mu\text{m}$ QCL-on-SONOI with a 4 mm-long active region, before and after depositing an AR coating on a SONOI waveguide facet. This laser (Device A) had a 6 μm -wide III-V mesa and a 1.0 μm -wide silicon waveguide.

the tapers, rather than the SONOI end facets, may define the primary lasing cavity. A reduced efficiency then results from the smaller fraction of light generated within the higher-Q inner cavity (formed by the tapers) able to couple into the SONOI waveguide for extraction. In order to investigate this possibility, an antireflective (AR) coating was applied to the SONOI end-facets on the output side of some of the lasers. The AR coating deposited by electron beam evaporation consists of a $\lambda/4$ thick alumina layer (for $\lambda=4.85 \mu\text{m}$) with refractive index ~ 1.6 . Figure 4.11 compares the L-I curves for Device A before (black) and after (red) the AR coating was applied. The threshold is seen to increase only modestly (by 20%, to 466 mA) while the efficiency decreases from 153 mW/A to 89 mW/A (most likely because the threshold current is approaching the thermal rollover regime). Consistent results were obtained for one other device that showed a similar threshold increase and a slight increase of the efficiency. Three other devices did not lase following AR coating of the output facet, probably because they operated too close to

the thermal rollover point. Device B had already been damaged when the AR coating experiments were performed.

The findings for the two devices that continued to lase following application of the AR coating are inconsistent with the assumption of lasing primarily within the cavity formed by the SONOI facets, since the much higher reflection loss at the AR-coated output facet should then have induced a proportionally larger increase of the lasing threshold. SEM inspection of the tapers during fabrication revealed substantial undercutting of the active region and a lithographic longitudinal misalignment between the upper cladding etch and the active region wet etch for some devices. The reflections within the taper were likely caused by the resulting active region taper, which was both non-uniform and shorter than the design. Variations of the fabricated taper tip geometry from device to device most likely produced different magnitudes of the taper reflectivities and transmission efficiencies. Such variations are probably responsible for the divergent performance characteristics of lasers that should have been more similar. Further experiments investigating the III-V taper dynamics will guide the optimization of future integrated QCL designs.

4.3 Distributed Feedback QCLs on SONOI

Wavelength-selective feedback mechanisms such as gratings or loop mirrors, which have been demonstrated at shorter wavelengths [1], may also be adapted to MIR QCLs on silicon. Distributed-feedback (DFB) lasers are attractive in many sensing applications including laser-based chemical bond spectroscopy, gas analysis [115], and explosive detection [116] that require a single frequency, narrow-linewidth source. In the present work, we have demonstrated DFB QCLs integrated with SONOI waveguides on a silicon substrate. These lasers output over 200 mW of peak power from a hybrid Si/III-V facet,

and operate to 100 °C.

Laser Designs

The integrated laser structure, SONOI waveguide platform, and fabrication process are similar to those described used for the Fabry-Perot QCLs on silicon, with the exception of the surface grating introduced onto the silicon waveguide. The same 30-stage QCL design as in Table 4.2 was used. A slightly shorter 3 mm-long active gain region was chosen for the DFB QCLs.

Lasers with four active region waveguide geometries were tested. Figure 4.12 shows active region cross sections for the four designs labeled A–D. Designs A, B and C contain fully-etched narrow III-V ridges as in [77], with mesa widths of 4 μm , 6 μm and 8 μm , respectively. Design D alternatively has a 6 μm -wide upper cladding combined with a 24 μm -wide active region. The width of the silicon waveguide underneath the active region is 1.5 μm for Designs A, B, and D and 3.5 μm for Design C. Figure 4.12 also overlays simulated optical modes onto the four waveguide cross-sections, along with estimated transverse optical confinement factors (Γ) in the active QCL stages. Both the active region confinement and optical overlap with the gratings etched into the underlying silicon depend on the widths of the III-V and silicon waveguides. Single-mode operation requires careful design of the laser geometry, so as to optimize both the net modal gain and the guided-mode mirror reflectivity. Here, the heterogeneous silicon platform provides some engineering versatility. For example, Design D with its narrow silicon waveguide and wide active region reduces the optical loss induced by sidewall roughness, while potentially maintaining operation in a single lateral mode. Since the current spreading below the lasing threshold is significant in QCLs, this is achieved at the expense of increasing the threshold current by the ratio of the active-region width to the lateral modal extent. The

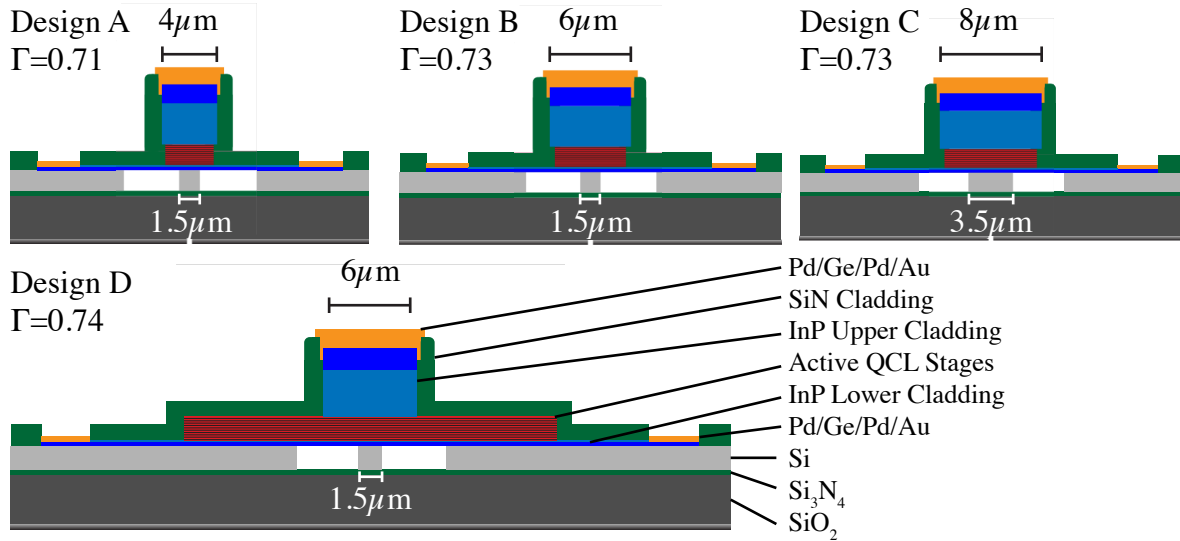


Figure 4.12: Cross-sectional schematics of the active regions for four different DFB QCL-on-SONOI designs. Simulated optical modes are overlaid (TM_{00} for Designs A, B, and D, and TM_{10} for Design C), and the active region transverse optical confinement factor Γ for each design is indicated.

far-field profiles discussed in the results Section 4.3 appear to show that, in agreement with the mode simulations illustrated in Figure 4.12, Designs A, B, and D lase primarily in the TM_{00} mode while Design C lases primarily in the higher-order TM_{10} mode.

Grating Designs

Typically, gratings for QCLs are defined on the laser ridge sidewalls [117], as a surface grating on the top of the laser [118], or buried within a cladding layer [119] with some advantages and disadvantages to each approach. QCL mesa sidewalls are typically several μm tall and defining a clean first-order sidewall grating that does not induce additional scattering loss can be challenging. Surface gratings can be associated with additional internal losses due to their proximity to the highly absorptive metal stack on top of the laser ridge. While gratings buried within a cladding layer allow a shallow low-loss grating to be introduced very close to the active region, this require a III-V regrowth

step. Heterogeneous integration alternatively offers the option of etching a shallow surface grating into the silicon waveguide underneath the III-V mesa [60], to provide distributed feedback.

The grating periods were chosen by first calculating the first-order Bragg wavelength as a function of grating period from the coupled mode theory approximation [120], $\lambda_B = 2\bar{n}_{eff}\Lambda$, where Λ is the pitch of the grating and \bar{n}_{eff} is the average effective index of the mode. The average effective index was approximated by an average of the effective indices of the optical mode simulated in FIMMWAVE (TM₀₀ for Designs A, B, and D, and TM₁₀ for Design C) with and without a grating air gap, weighted by the duty cycle of the grating.

The grating period used for different devices on the chip ranges from 738 to 778 nm based on an estimation that the etch depth would be ~ 25 nm and that the duty cycle would be 50%. After fabrication, the calculated Bragg wavelength for each device was adjusted to compensate for the measured grating etch depth of 28 nm and the measured etched duty cycle of $\sim 31\%$. The active region wet etch step during fabrication also undercut the active region, reducing the active region width within the mesa. This undercut was estimated from images during and after laser fabrication.

Table 4.3 shows the weighted effective indices, simulated in FIMMWAVE. To correspond with data in the results Section 4.3 (as discussed below), the effective indices were adjusted by a factor of 0.99.

Grating Fabrication

The shallow DFB grating is etched onto the surface of the silicon waveguides throughout the extent of the 3 mm-long active region, with a quarter-wavelength shift introduced in the middle. Figure 4.13(a) shows a 3D illustration of the SONOI waveguide with an

Table 4.3: Adjusted \bar{n}_{eff} for DFB QCLs with gratings

Upper InP width (μm)	Active QCL width (μm)	Si waveguide width (μm)	Mode	\bar{n}_{eff}
4	3.6	1.5	TM ₀₀	3.119
6	5.6	1.5	TM ₀₀	3.140
8	7.6	3.5	TM ₀₀	3.179
8	7.6	3.5	TM ₁₀	3.108
6	24	1.5	TM ₀₀	3.146

etched surface grating underlying the III-V layers and Figure 4.13(b) illustrates the DFB QCL, consisting of a hybrid Si/III-V active region coupled by III-V tapers to passive silicon waveguides on both sides, as in previous Fabry-Perot QCL devices. End facets are formed by mechanically polishing the passive SONOI waveguides. The SONOI waveguide is fully etched and 1.5 μm tall.

The silicon waveguides in the passive regions and output facets are 2 μm wide. However, the silicon waveguides expand underneath the III-V taper to aid the mode conversion. For subsequent measurements carried out to clarify the role of the tapers in the laser operation, the tapers adjacent to the output facet were removed by polishing back to immediately past the tapers. In that case, the silicon waveguide at the resulting hybrid Si/III-V output facet was slightly wider than within the rest of the hybrid active region. Figure 4.13 depicts the laser structure with one taper removed.

Before the silicon waveguide is etched, the grating is patterned onto the silicon with electron beam lithography (EBL) and formed with a $\text{C}_4\text{F}_8/\text{SF}_6/\text{Ar}$ inductively coupled plasma (ICP) etch. Atomic force microscope (AFM) measurements of one device found a $\sim 31\%$ etched silicon duty cycle and 28 nm etch depth.

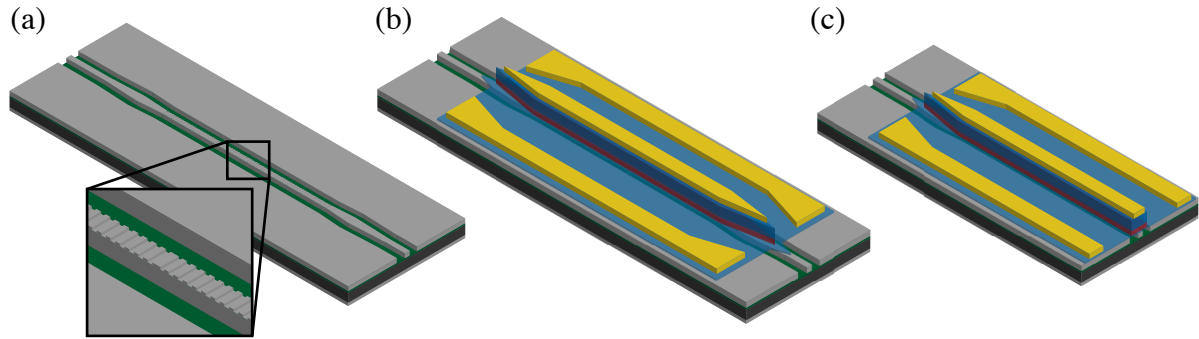


Figure 4.13: A 3D schematic of (a) a SONOI waveguide with shallow surface DFB grating, which lies underneath the integrated QCL (b) a DFB QCL heterogeneously integrated with a SONOI waveguide, including III-V tapers on both sides of the laser (c) an integrated DFB QCL with one taper removed to expose a hybrid III-V/Si facet.

Results

The DFB QCLs were driven with 250 ns wide pulses at 1 kHz repetition rate. The I-V characteristics at 20 ° C of each device were measured both before and after removal of the III-V tapers. Figure 4.14 shows the best of the results for a device (of Design D) before the taper was removed (with the assumption that the current spreads uniformly over the 24 μm -wide active region). Although the threshold current density appears quite low (0.58 kA/cm²), the maximum output power is only 11 mW, and the differential slope efficiency is only 23 mW/A. These observations would be inconsistent if obtained for a conventional QCL geometry with cleaved facets, since the observed low efficiency implies a high loss, which should greatly increase the threshold current density. Other devices of all 4 designs also displayed relatively low threshold current densities of 0.6–1.2 kA/cm², but even lower maximum output powers of 1.2–4.1 mW. Several of the devices (of Designs B and C) did not produce enough light to measure.

All of the lasers were re-measured following removal of the tapers from the output sides. Figure 4.15 plots the light intensity vs. injection current density for all of the lasers studied (2 with Design A, 2 with Design B, 4 with Design C, and 2 with Design

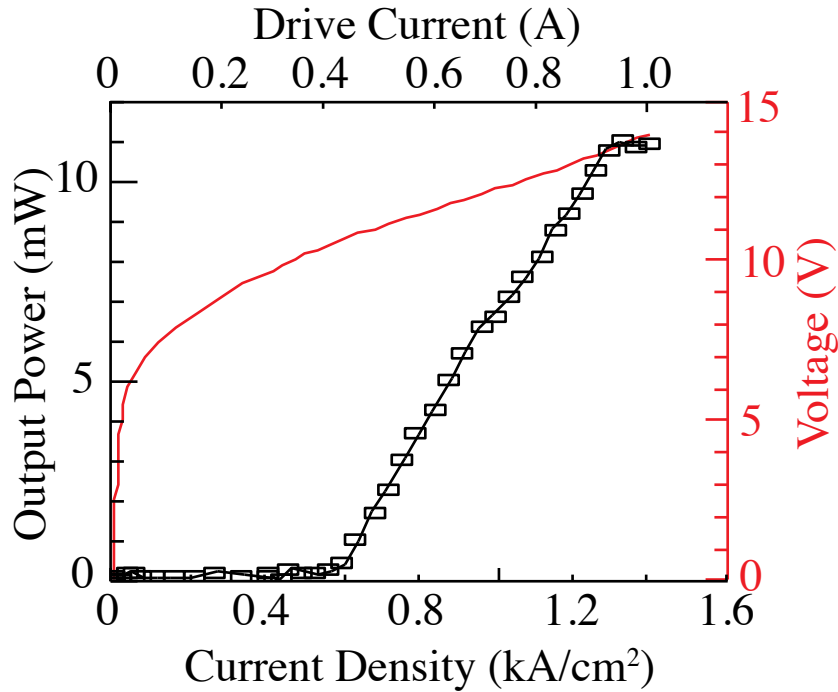


Figure 4.14: Pulsed output power and voltage vs. injection current density and current at 20 °C of an integrated $\lambda \approx 4.8 \mu\text{m}$ DFB QCL-on-SONOI of Design D with a 3 mm-long active region and III-V tapers on both sides. Light is collected from the polished passive SONOI facet. This laser had a 6 μm -wide upper InP cladding, a 24 μm -wide QCL active region, and a 1.5 μm -wide silicon waveguide.

D). In all cases, the threshold current densities increased only slightly (by 7-26%) while the differential efficiencies improved dramatically (by factors of 14-51). Furthermore, the devices that emitted too little light to measure when both tapers were intact became fully operational, with performance comparable to the others. Apart from one anomalous device (Design A), the slope efficiencies following removal of the tapers ranged from 161 mW/A (for a laser with Design C) to 541 mW/A (Design D). The maximum measured output power was 211 mW (not yet saturated), as seen in Figure 4.15(d). The threshold current densities ranged from 0.71 to 1.36 kA/cm² for Designs A, B, and D, while the thresholds for devices with Design C were somewhat higher (1.44-1.83 kA/cm²).

The low threshold current densities, both before and after the tapers were polished

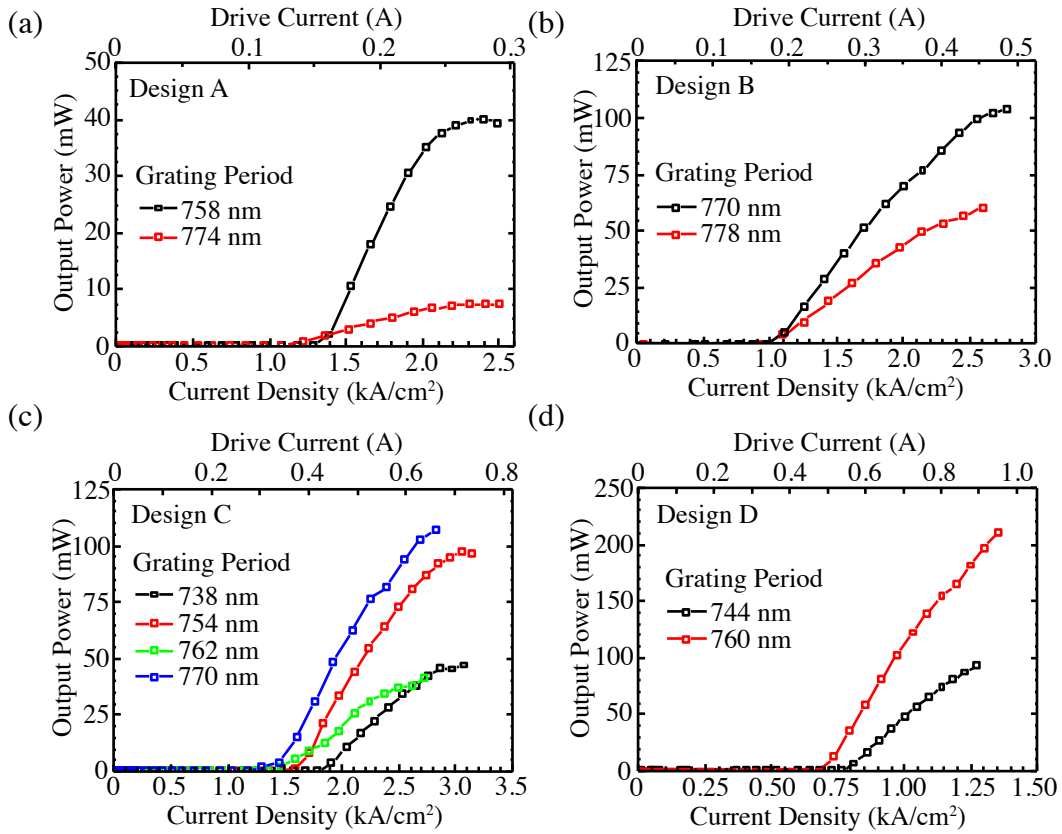


Figure 4.15: Pulsed output power vs. injection current density at 20 °C for $\lambda \approx 4.8 \mu\text{m}$ DFB QCLs-on-SONOI after taper removal, with four different active region designs and various grating pitches. Light is collected from a polished hybrid Si/III-V facet.

off, indicate that the tapers limit the collection efficiency outside of the DFB cavity rather than increase the loss within the primary laser cavity. The slight increase in threshold current after removal of the taper suggests that the reflectivity from the taper is higher than that of the polished (but uncoated) hybrid Si/III-V facet, whereas a large increase in the slope efficiency after the polishing indicates that the transmission through the taper is very low. This is consistent with the findings of our previous investigation of heterogeneously integrated QCLs, from which we concluded that the taper reflections are strong enough to form the primary Fabry-Perot lasing cavity [77].

The narrow III-V waveguide of Design A and the TM_{10} mode of Design C (see Figure

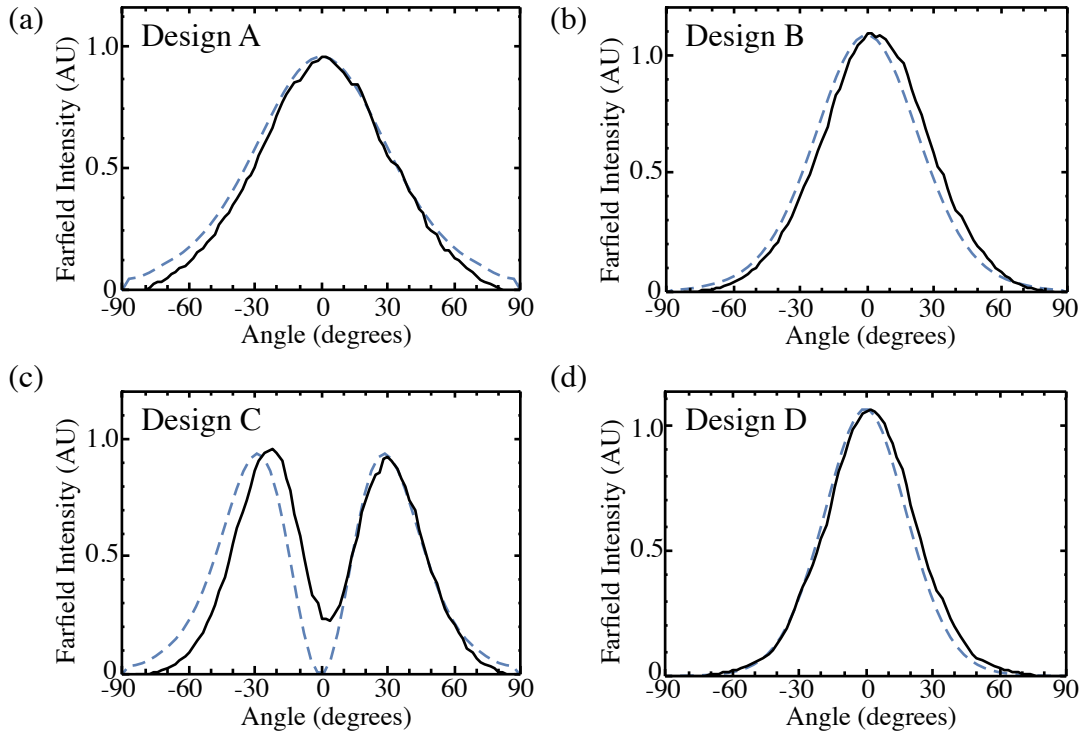


Figure 4.16: Slow-axis far field profiles for a $\lambda \approx 4.8 \mu\text{m}$ DFB QCL-on-SONOI of each of four active region design. The drive currents were 200, 350, 500, and 700 mA for Designs A-D, respectively. The solid curves show the measured profiles while the dashed curves show the simulated profiles for the TM_{00} mode in (a), (b), and (d) and the TM_{10} mode in (c).

4.12 and Figure 4.16 below) induce greater mode interaction with the InP mesa sidewalls relative to the other designs. The additional internal loss contributed by sidewall roughness most likely causes the higher current densities observed for lasers of Design A and Design C. Although a laser with Design A displayed the second highest slope efficiency (489 mW/A), that result may be related more closely to out-coupling efficiency than to loss.

The solid lines in Figure 4.12 represent the slow-axis far field profiles for one laser with each waveguide geometry. The single-lobe distributions observed for devices with Designs A, B, and D indicate lasing primarily in the fundamental TM_{00} mode. The two lobes seen in the profile for Design C indicate that the higher-order TM_{10} mode dominates the

emission, although the absence of a complete central null suggests that the fundamental mode also contributes. The dashed curves are FIMMWAVE simulations of the far field distributions corresponding to the TM_{00} and TM_{10} modes of each waveguide design at the hybrid Si/III-V facets. These agree well with the measured profiles, with the exception of Design C near 0 degrees. The fast-axis profile measured for the device with Design B displays a similar symmetric single-lobe distribution.

These mode selections are generally consistent with the optical confinement distributions simulated for each of the active cross-section designs. The second-order TM_{10} mode is calculated to be above cutoff for the narrow $4\ \mu\text{m}$ mesa of Design A. While Design B supports a TM_{10} mode with high active region confinement, that mode resides almost entirely in the III-V mesa, overlaps significantly less with the Si surface grating, and interacts more with the mesa sidewalls. The $3.5\ \mu\text{m}$ wide Si waveguide of Design C is wide enough to contain much of the TM_{00} mode, which limits its active region confinement ($\Gamma = 0.46$) compared to the TM_{10} mode ($\Gamma = 0.73$). However, this configuration may allow both modes to lase simultaneously, given that the fundamental mode may suffer less from sidewall scattering loss. The apparent operation of the laser with Design D in a single mode is not as easily explained, since both the TM_{00} and TM_{10} modes have sufficient overlap with the active region and grating. One possibility is that the wider higher-order mode may have additional loss associated with optical leakage into the silicon slab on both sides of the $4\ \mu\text{m}$ -wide air trenches that define the silicon waveguide.

Spectral measurements at $20\ ^\circ\text{C}$ were acquired with a Digikrom 0.5 m monochromator with 1.5 nm resolution. Figure 4.17 shows the spectra for lasers of each geometry and various grating periods. In all cases, a primary lasing peak at a wavelength ranging from $4.62\text{--}4.86\ \mu\text{m}$ tracks the central Bragg frequency of the particular DFB grating, although many of the lasers emit in multiple modes. The weaker spectral features likely result from Fabry-Perot resonances corresponding to reflections between the polished

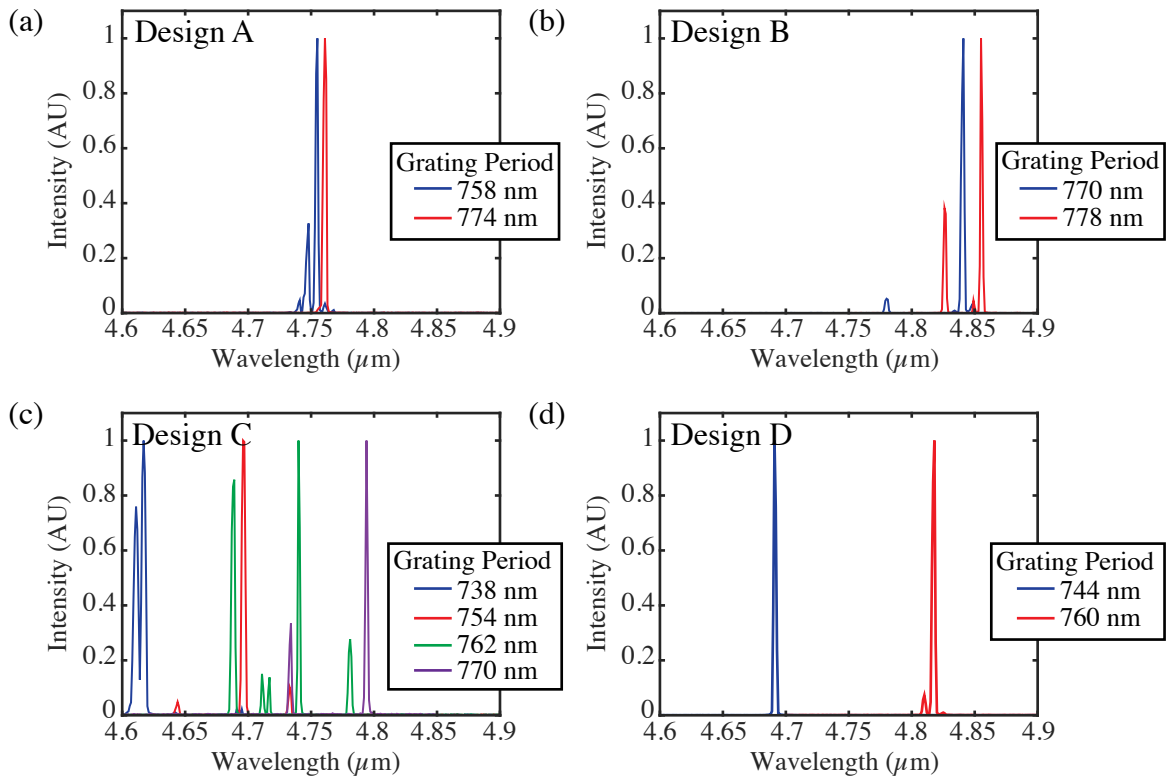


Figure 4.17: Normalized emission spectra at 20 °C of $\lambda \approx 4.8 \mu\text{m}$ DFB QCLs-on-SONOI with four designs, as measured with a monochromator. The spectra were obtained at currents of ~ 0.3 A for Designs A and B, 0.5 A for Design C, and 0.7 A for Design D. The legends show the DFB grating pitches of each device.

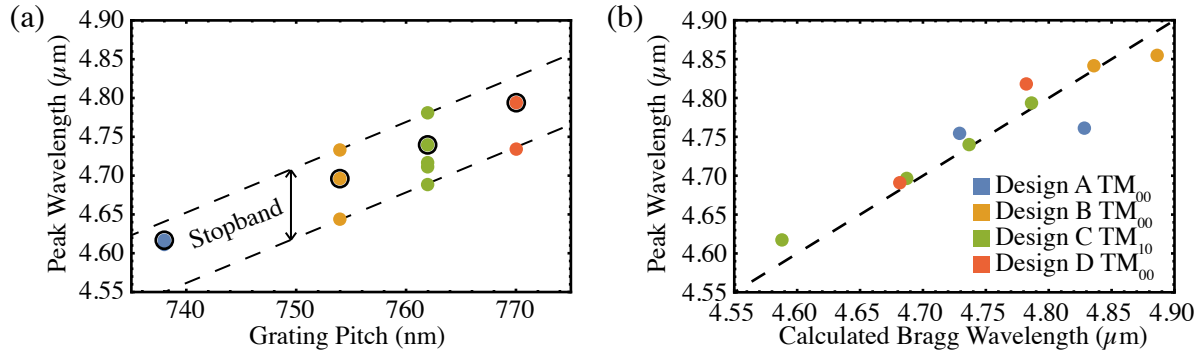


Figure 4.18: (a) Measured peak wavelengths as a function of DFB grating pitch for all four $\lambda \approx 4.8 \mu\text{m}$ DFB QCLs-on-SONOI of Design C, from the spectral data of Figure 4.17(c). Multiple points of the same color (a single grating pitch) represent the multiple spectral peaks for that device. The circled points represent the strongest peak for that device. The dashed lines, with a slope of $\sim 6.2 \text{ nm/nm}$ ($\approx 2 n_{eff}$), show that modes lasing at the edges of the 90 nm wide stopband track the fabricated grating pitch. As in Table 4.3, the simulated n_{eff} of the TM_{10} mode is 3.108 (b) Measured peak wavelength as a function of calculated Bragg wavelength for the strongest lasing mode of the devices shown in Figure 4.17.

hybrid Si/III-V facet and the remaining III-V taper. Inconsistencies of these modes from device to device may be attributed to variations in the taper fabrication associated with non-uniform undercut at the taper tip across the chip after wet etching of the active region.

For the lasers with Designs A and D, the central mode of the $\lambda/4$ -shifted DFB grating appears split by the additional cavity resonance, while the lasers with Designs B and C show evidence for higher-order grating modes at the edges of the stop-band. For all four lasers with Design C, Figure 4.18(a) plots the wavelengths of the strongest peaks as a function of grating periodicity. The central peak (circled points) and two side modes follow a linear trend with the grating period, indicated by the dashed lines. This suggests a grating stopband width of 90 nm for this design.

Figure 4.18(b) shows the wavelength of the strongest peak for each laser with all four designs vs. the estimated Bragg wavelength of the DFB grating. The Bragg wavelength calculated directly from the simulated value of \bar{n}_{eff} is on average 1% lower than the

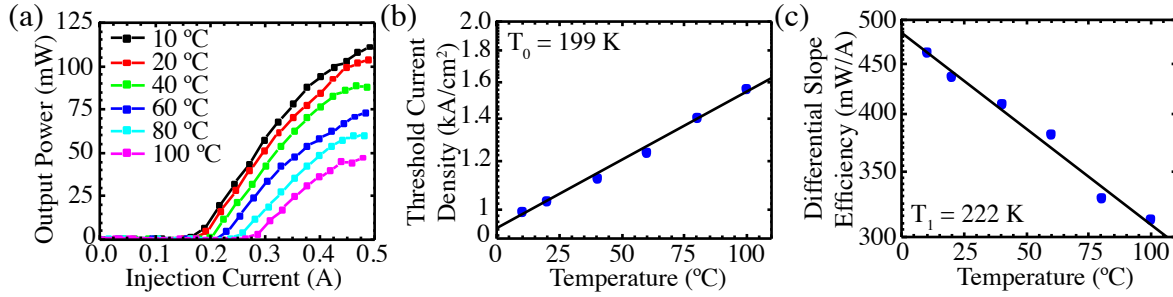


Figure 4.19: (a) Pulsed output power for a $\lambda \approx 4.8 \mu\text{m}$ DFB QCL-on-SONOI of Design B at temperatures ranging from 10 °C to 100 °C. The III-V mesa width was 6 μm and the silicon waveguide width was 1.5 μm . (b) Corresponding threshold current density vs. temperature, which yields a characteristic temperature of $T_0=199$ K. (c) Corresponding differential efficiency vs. temperature, which yields a characteristic temperature of $T_1=222$ K.

measured peak wavelength. This inconsistency is most likely attributable to an overestimation of the effective index by the mode solver. Accordingly, the \bar{n}_{eff} values used to calculate the Bragg Wavelength for Figure 4.18(b) are adjusted by a factor of 0.99. Note the nearly linear dependence of the experimental peak emission wavelength on calculated Bragg wavelength. The only significant departure is for the same laser with Design A (emitting at $\lambda=4.76 \mu\text{m}$) that displayed anomalously low slope efficiency.

Figure 4.19(a) shows the light output vs. injection current for the laser of Design B with grating period 770 nm, measured at a range of temperatures from 10 to 100 °C. The threshold current density and differential slope efficiency vs. temperature are shown in Figures 4.19(b) and 4.19(c), respectively. The characteristic temperatures of $T_0=199$ K for threshold and $T_1=222$ K for efficiency are extracted from the exponential fits indicated by the lines.

Both of these relatively high pulsed characteristic temperatures are much higher than those observed for the Fabry-Perot QCLs on silicon [77], which lased in pulsed mode only to 60 °C. One possibility is that the gain peak is better matched to the Bragg wavelength at higher temperatures. The much higher T_0 and T_1 values are consistent with both the

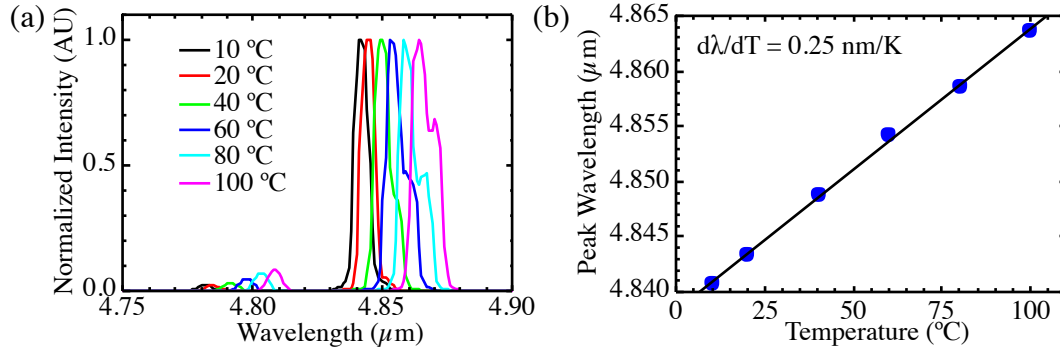


Figure 4.20: (a) Temperature-dependent emission spectra for the same $\lambda \approx 4.8 \mu\text{m}$ DFB QCL-on-SO₂ with a 3 mm-long active region of Design B whose temperature-dependent L-I characteristics are shown in Figure 4.19. The III-V mesa width was $6 \mu\text{m}$ and the silicon waveguide width was $1.5 \mu\text{m}$. (b) Peak wavelength as a function of temperature.

significantly lower room temperature threshold current density compared to the Fabry-Perot devices [77] and the relatively low injector sheet-doping density ($\sim 0.5 \times 10^{11} \text{ cm}^{-2}$) [113].

Figure 4.20 shows the emission spectra for the same device over the same range of temperatures. The single primary peak tunes at a rate of 0.25 nm/K , which is consistent with the expected shift of the modal index that governs the DFB mode rather than the shift of the gain peak.

Given their low threshold current densities and high characteristic temperatures, CW operation of these lasers at room temperature should be achievable with improved heat dissipation.

4.4 QCL Thermal Analysis

The QCLs in this dissertation function only in pulsed mode and do not reach a lasing threshold when operated in CW mode, either at room temperature or while cooled. For first-generation devices, this is not an unexpected result. QCLs operate at higher

threshold current densities and threshold drive powers than diode lasers. Many of the Fabry-Perot and DFB lasers discussed here dissipate near 4 W of injected power before reaching lasing threshold. In general, even the best QCLs on a native substrate typically generate much more heat than light and 70–80% of the injected electrical power must be dissipated as heat [14]. This issue is not improved by the inherently low thermal conductivity of the QCL active stage materials, InGaAs and AlInAs, which help trap heat within the active region. QCLs operating in CW mode typically employ heat extraction techniques either implementing buried heterostructures with thick, electroplated gold for epilayer-up operation, or epilayer-down mounting where the QCL ridge is flip-chip bonded, post fabrication, to a submount with preferable thermal characteristics.

AlN is the most common thermal submount used for QCLs because the thermal expansion coefficient is matched well to that of InP. The thermal conductivity of AlN (~ 200 W/(m-K)) is almost 3 times that of InP (~ 70 W/(m-K)) [14]. Fortunately, the thermal conductivity of silicon is also quite high (~ 160 W/(m-K)) [121].

COMSOL Multiphysics thermal simulations were used to analyze the QCLs-on-SONOI and other material systems. Figure 4.21 shows thermal simulations of QCLs integrated above SONOI (with 1.5/0.4/3.0 μm -thick Si/Si₃N₄/SiO₂) and SON (1.5/0.4 μm -thick Si/Si₃N₄) waveguides. For these simulations, the active region representing 30 QCL stages (for $\lambda=4.8\mu\text{m}$ emission) was injected with 2 A of CW current and biased under an ideal voltage condition of 7.75 V, although practical operating voltages for QCLs at this wavelength can be above 10 V depending on design and operating current. These simulations assume an ideal simplified case where power is dissipated only from the voltage drop of the radiative transitions in the active region, and neglects finite series or contact resistance in real devices, which will add additional heating to the overall device. The active region and InP thermal conductivity values used were from [122], while other material constants were supplied by COMSOL.

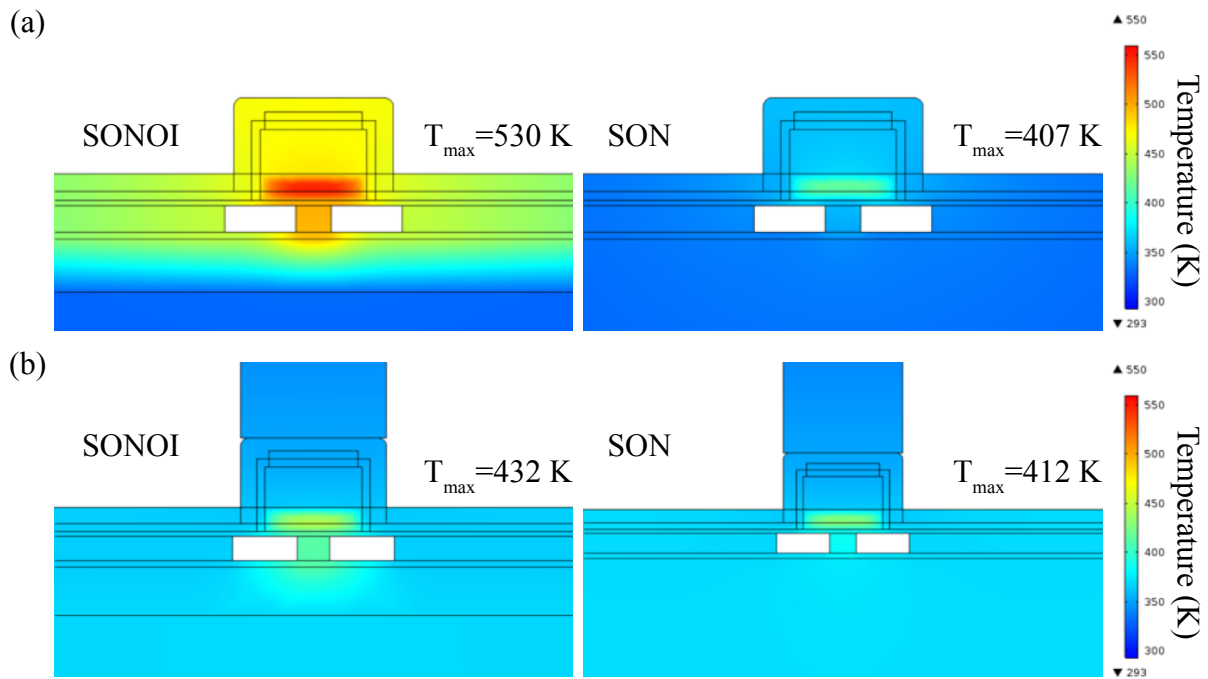


Figure 4.21: 2-dimensional COMSOL thermal simulations of heterogeneously integrated QCLs with $6 \mu\text{m}$ -wide QCL mesas. The simulated active region is injected with 2 A injection current biased under ideal voltage conditions at 7.75 V. All injected power is thermally dissipated and the maximum temperature is indicated. The figures on the left of (a) and (b) show a QCL ridge integrated above a SONOI waveguide, while the figures on the right of (a) and (b) show a QCL ridge integrated above a SON waveguide. For (a) the heat is extracted downward through the silicon substrate, held at 20°C , while for (b) the heat is extracted through gold upward and through an AlN submount, held at 20°C .

The underlying SiO_2 provides the primary thermal bottleneck for heat extraction downwards of these lasers. In 4.21(a), heat is extracted downward through the silicon substrate, the base of which is held at room temperature. Note that by removing the 3 μm SiO_2 layer for the QCL-on-SON, the maximum temperature is drastically reduced. In 4.21(b), heat is extracted upward instead through gold and an AlN submount (not shown). In this case, the top submount surface is held at room temperature rather than the silicon substrate. Here the effect of the SiO_2 layer is minimized because the majority of the heat travels upward. Lateral heat spreading is still improved for the QCL-on-SON case, slightly reducing the active region temperature.

Of particular note, is that the QCL-on-SON in 4.21(a) has a lower maximum temperature than the simulated lasers which use an AlN submount. While this simplified simulation likely does not fully represent the improvements which can be achieved with a state-of-the-art flip-chip submount configuration, this does show that good thermal performance should be possible by constructing a QCL on a silicon-based waveguiding system. For applications where the broadband SONOI platform is not necessary, removing or significantly thinning the SiO_2 layer should greatly reduce the active region temperature. Similarly, constructing a QCL on the Ge-on-Si waveguide system should yield good thermal performance. A thermal submount, as is used for QCLs fabricated on a native III-V substrate, can also be applied to heterogeneously integrated QCLs.

4.5 Conclusion and Summary

We have demonstrated the successful heterogeneous integration of QCLs on silicon with the broadband SONOI platform. Both Fabry-Perot and DFB QCLs were demonstrated, which coupled light through III-V tapers into passive silicon waveguides.

The Fabry-Perot lasers displayed threshold currents as low as 387 mA and single-

sided output powers as high as 31 mW in pulsed operation at 20 °C. These lasers functioned up to 60 °C. The characteristic temperatures T_0 and T_1 were found to be 175 K and 87 K, respectively. This pulsed characteristic temperature T_0 is typical for a relatively low-injector-doping, 4.5–5.0 μm -emitting QCL suitable for low-power-dissipation applications. We found that some of the Fabry-Perot lasers continued to lase after an anti-reflective coating was deposited on a silicon waveguide facet, indicating that strong reflections from the III-V tapers were present.

We have also demonstrated QCLs heterogeneously integrated with SONOI waveguides that incorporate shallow $\lambda/4$ -shifted distributed feedback surface gratings etched into the silicon waveguides underneath the bonded III-V layers. Lasers with four different active region geometries were measured. Multiple grating periodicities systematically selected lasing modes at wavelengths ranging from 4.62 to 4.86 μm . The lasers operate up to 100 °C, and emit over 200 mW of pulsed power with slope efficiencies up to 541 mW/A from a hybrid Si/III-V polished facet. Threshold current densities $<1 \text{ kA}/\text{cm}^2$ are observed for devices both before and after removal of the taper adjacent to the output facet.

Although strong reflection from and low transmission through the III-V taper are observed for these lasers, it should be possible to significantly improve the efficiency of mode transfer to the silicon waveguide by optimizing both the fabrication process and the waveguide design (discussed more in Chapter 6).

Chapter 5

Interband Cascade Lasers on Silicon

The optimal on-chip chemical sensing system will fully integrate one or more light source in the PIC. However, the most appropriate MIR emitter depends on the wavelength range chosen for the given application, since no single semiconductor laser technology provides high performance throughout the MIR. Interband GaSb- and InP-based diode lasers can operate with low threshold drive powers at MIR wavelengths as long as $\sim 6 \mu\text{m}$ [123, 5, 15], whereas InP-based quantum cascade lasers (QCLs), which derive gain from intersubband optical transitions, are capable of providing high output powers with high wallplug efficiencies at wavelengths extending from $4 \mu\text{m}$ to the Terahertz regime [8].

An overview of ICLs is given in Chapter 1.3. The GaSb-based interband cascade laser (ICL) derives gain from band-to-band electron-hole recombination, as in a conventional diode laser, but with multiple cascading stages to recycle the electrons as in a QCL [16, 124]. These lasers function from $2.9\text{--}7 \mu\text{m}$ [7], with threshold drive powers 1–2 orders of magnitude lower than for QCLs [22], while still generating up to 500 mW of continuous wave (CW) output power [21]. ICLs are ideal for MIR spectroscopy in $3\text{--}6 \mu\text{m}$ applications that rarely require Watt-level optical power. An ICL-based system with far lower energy demand will have a much smaller spatial footprint, for ready deployment

in a hand-held or remotely-deployed sensor powered by batteries or solar energy.

While preliminary measurements of GaSb-based lasers operating in pulsed mode near $2.38\ \mu\text{m}$ have been reported [70], the III-V active elements in the vast majority of lasers integrated on silicon have been grown on InP and GaAs substrates. GaSb-based device integration introduces additional fabrication and design challenges, because the selective etch chemistries required to define and pattern active antimonide devices are much less mature. The III-V layers of an ICL on silicon must be engineered to produce a high-gain optical mode and efficient III-V tapers to couple the hybrid and silicon waveguide sections with high yield.

In this work, we demonstrate the first integration of ICLs with silicon waveguides. These lasers emit at $\lambda = 3.65\ \mu\text{m}$ and operate in pulsed mode up to $50\ ^\circ\text{C}$. To better understand the laser performance, each device was characterized both before and after the III-V taper was removed from one end of the laser.

This work is currently in review in [79].

UCSB: *A. Spott, E. Stanton, A. Torres, M. Davenport, and J. Bowers.* A. Spott designed the lasers, fabrication process, and mask, fabricated the devices, and performed the initial laser characterization and the facet polishing. Alfredo Torres aided in the fabrication process development. The team at UCSB contributed to the laser design, fabrication process design, and data interpretation.

US Naval Research Laboratory: *C. Canedy, I. Vurgaftman, M. Kim, C.S. Kim, C. Merritt, W. W. Bewley, and J. R. Meyer.* The team at NRL aided in the fabrication process design, laser design, and data interpretation, performed the MBE growth of the ICL material, and performed the laser characterization measurements included in this Chapter.

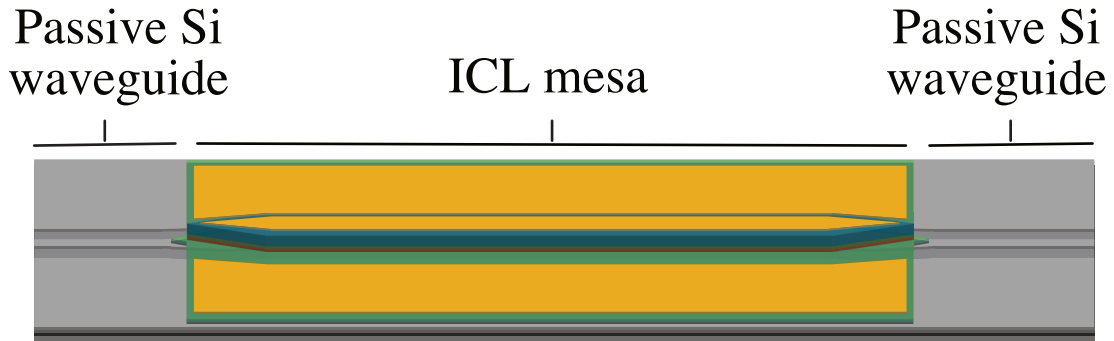


Figure 5.1: 3D schematic of the ICL heterogeneously integrated with a silicon waveguide.

5.1 Fabry-Perot ICLs on SOI

Design

The waveguide design of the heterogeneously-integrated ICL is similar to that we used previously to integrate Fabry-Perot QCLs on silicon [77]. Figure 5.1 schematically shows a tilted top-view of the device. The III-V mesa bonded to the silicon waveguide forms a 3100 μm -long hybrid III-V/Si gain region bounded by 320- and 350- μm -long passive silicon waveguide regions. Both ends of the III-V mesa narrow in 50- μm -long tapers which are designed to adiabatically transfer the hybrid III-V/Si optical mode to the passive silicon waveguide. The silicon waveguide is terminated on both ends by polished silicon facets, which are designed to reflect light and form a Fabry-Perot laser cavity.

The lasers were constructed on the SOI platform. While a silicon-on-nitride-on-insulator (SONOI) platform was used in our previous integration of QCLs, SOI waveguides have been shown to maintain propagation losses as low as 1.5 dB/cm at wavelengths up to 3.73 μm [125, 126].

Figure 5.2 shows a cross section of the hybrid III-V/Si active region. A narrow, partially-etched silicon rib waveguide sits underneath the wider III-V mesa. The thin n-InAs/AlSb bottom contact layer extends laterally to both sides of the mesa, where

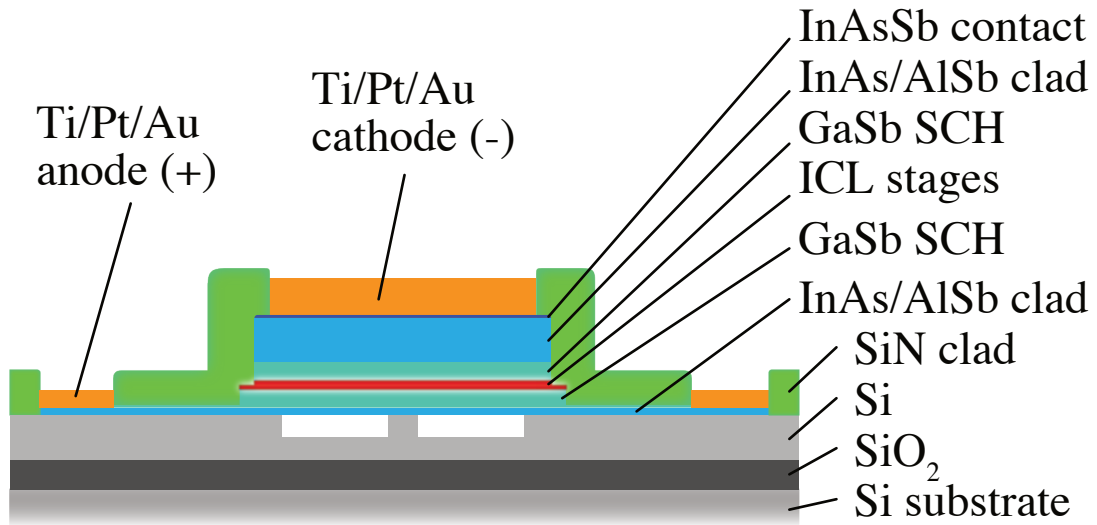


Figure 5.2: Cross-sectional schematic of the III-V/Si active region of an ICL-on-SOI.

Table 5.1: Laser Geometries

Laser	Si waveguide width (μm)	III-V mesa width (μm)
Device A	1	11
Device B	1	8
Device C	2	6

Table 5.1: ICL III-V layers

Description	Material	Thickness (nm)	Doping (cm^{-2})
Substrate	GaSb	–	–
Buffer	n-GaSb	400	1.0×10^{17}
Etch stop	<i>n</i> -InAsSb	1000	5.0×10^{18}
Sacrificial	<i>n</i> -GaSb	100	1.0×10^{17}
Top contact	<i>n</i> -InAsSb	100	5.0×10^{18}
Transition	<i>n</i> -InAs/AlInSb SL	33.8	5.0×10^{18}
Transition	<i>n</i> -InAs/AlSb SL	31.9	5.0×10^{18}
Top clad	<i>n</i> -InAs/AlSb SL	1400	$1.5\text{--}5.0 \times 10^{17}$
Transition	<i>n</i> -InAs/AlGaSb SL	24.5	2.0×10^{17}
Top SCH	<i>n</i> -GaSb	600	$0.05\text{--}1.0 \times 10^{17}$
Transition	<i>n</i> -InAs/AlSb SL	20	2.0×10^{18}
Active core	<i>n</i> -InAs/AlSb/GaInSb	290	Variable
Transition	<i>n</i> -n-InAs/AlSb SL	20	2.0×10^{17}
Bottom SCH	<i>n</i> -GaSb	600	$0.05\text{--}1.0 \times 10^{17}$
Transition	<i>n</i> -InAs/AlSb SL	24.5	2.0×10^{17}
Bottom contact	<i>n</i> -InAs/AlSb SL	200	5.0×10^{17}
Bonding SL	GaSb/AlSb SL	30	–
Capping layer	GaSb	10	–

metal is placed to form anodes. Lasers were fabricated with silicon waveguide widths of 1, 2, or 3 μm , while the III-V mesa widths ranged from 5 to 11 μm . This manuscript focuses on the performance of three specific lasers with the dimensions specified in Table 5.1.

The ICL wafer was grown by molecular beam epitaxy (MBE) on a GaSb substrate at the Naval Research Laboratory (NRL). Table 5.1 summarizes the III-V layer stack. The 7-stage W active region, which is similar to those employed in Refs. [127, 21], is designed for emission near 3.6 μm . As in other heterogeneously integrated lasers, the surrounding layers are modified for integration on silicon. An etch stop layer and sacrificial layer are included to allow removal of the GaSb substrate. Alternating GaSb and AlSb layers comprise a bonding superlattice (SL) to prevent defects at the bonding interface from propagating into the bottom contact and active region, although the potential for such

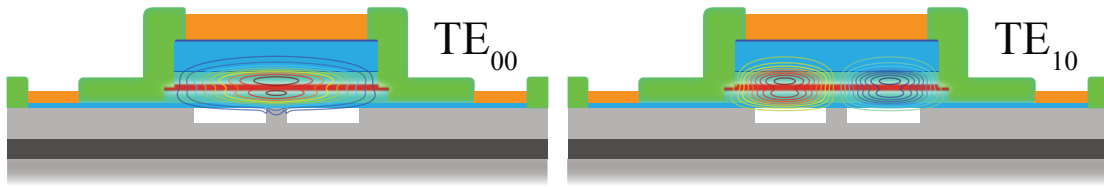


Figure 5.3: Active region cross sections of an integrated ICL-on-Si (Device A) overlaid with contour plots of the electric field profiles $|E_x|$ of the first two optical modes.

defect propagation has not been investigated thoroughly for this type of heterogeneous laser. The n-InAs/AlSb SL bottom contact layer is thin to allow the optical mode residing partly in the active ICL stages to also overlap the silicon waveguide, and to minimize free-carrier absorption in the heavily-doped contact layer.

The III-V layering design of the heterogeneously-integrated laser presents a trade-off between sufficient modal overlap with the active stages to provide high gain, against high overlap with the silicon in the hybrid mesa and tapered regions to efficiently transfer light from the hybrid waveguide to the passive silicon waveguides at each end of the mesa. Thicker bottom SCH and bottom contact layers also increase the fabrication tolerances, as discussed in the fabrication Section 5.1 below. In the trade-off between net gain, taper performance, electrical performance, and fabrication difficulty, our first-generation integrated ICL design emphasized high optical overlap with the ICL stages and minimum fabrication difficulty. In particular, the 600 nm thickness of the high-index ($n \sim 3.77$) GaSb SCH layers facilitated the anode metal deposition and increased the active-region mode confinement. However, it also reduced overlap with the silicon waveguide, which appears to have compromised the taper performance as will be discussed below in the results Section 5.1. The epilayer thicknesses in the next generations of these lasers will be adjusted to address the taper efficiency.

Figure 5.3 illustrates the simulated electric field profile — E_x — for the TE_{00} and TE_{10}

optical modes overlaid on the active-region cross section of Device A. The simulated transverse confinement factor for the active stages including the injectors, Γ , in all three devices ranges from 0.17 to 0.18 for both modes. While for the TE_{10} mode slightly exceeds that for the TE_{00} mode, the difference of < 0.01 should not meaningfully impact the mode selection. In all three lasers, the silicon waveguide with $2 \mu\text{m}$ width in the taper region narrows to $1.5 \mu\text{m}$ beyond the tapers. Since the passive silicon waveguide supports only the fundamental TE_{00} mode, it should act as a mode filter. However, misalignment or imperfections in the taper fabrication may potentially couple TE_{00} light from the passive silicon region into higher-order modes within the hybrid III-V/Si region, as will be discussed below.

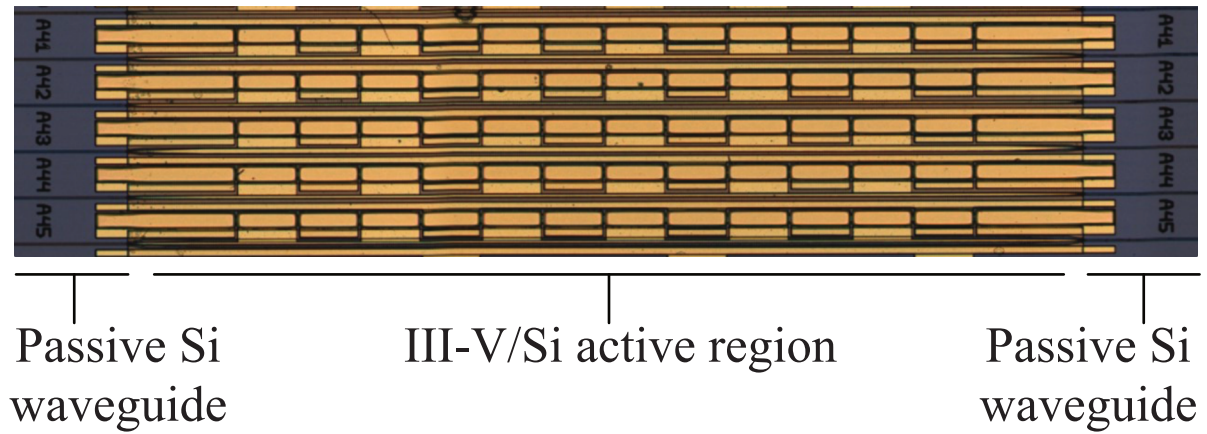
Fabrication

Figure 5.4(a) shows an optical microscope image of the bar containing five integrated ICLs with various geometries (following all the fabrication). Figure 5.4(b) shows scanning electron microscope images of the tapered III-V region of a representative device in the middle (left) and at the end (right) of the fabrication.

Figure 5.5 schematically illustrates the fabrication steps. Processing begins with an SOI wafer consisting of a 1500 nm thick silicon device layer above $1 \mu\text{m}$ of buried SiO_2 (BOX) on a silicon substrate. First, silicon waveguides are patterned and partially etched to a depth of $\sim 750 \text{ nm}$ with a $\text{C}_4\text{F}_8/\text{SF}_6/\text{Ar}$ inductively coupled plasma (ICP) reactive ion etch (RIE). Vertical outgassing channels (VOCs) are fully etched through the Si device layer to aid the diffusion of molecules formed at the bonding interface [107].

After the silicon processing is complete, the III-V epilayer is bonded above the silicon waveguides with a hydrophilic plasma-assisted bonding process similar to that used to heterogeneously integrate InP-based devices [128]. The surfaces of the silicon and III-V

(a)



(b)

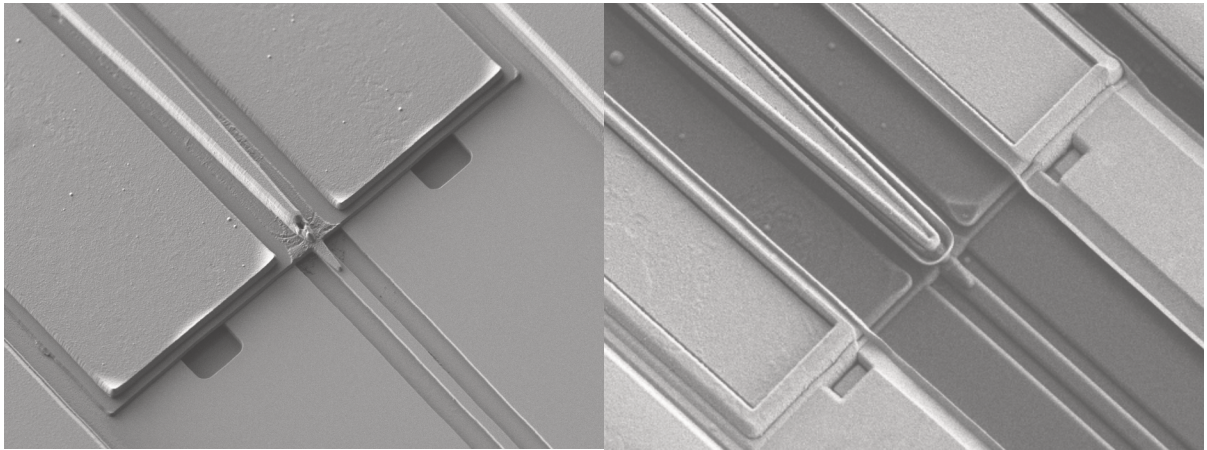


Figure 5.4: (a) Top-down optical microscope image of fully-fabricated ICLs integrated on silicon. (b) Scanning electron microscope (SEM) images of the III-V taper tip of a representative device. Left: before SiN encapsulation. Right: after probe metal deposition.

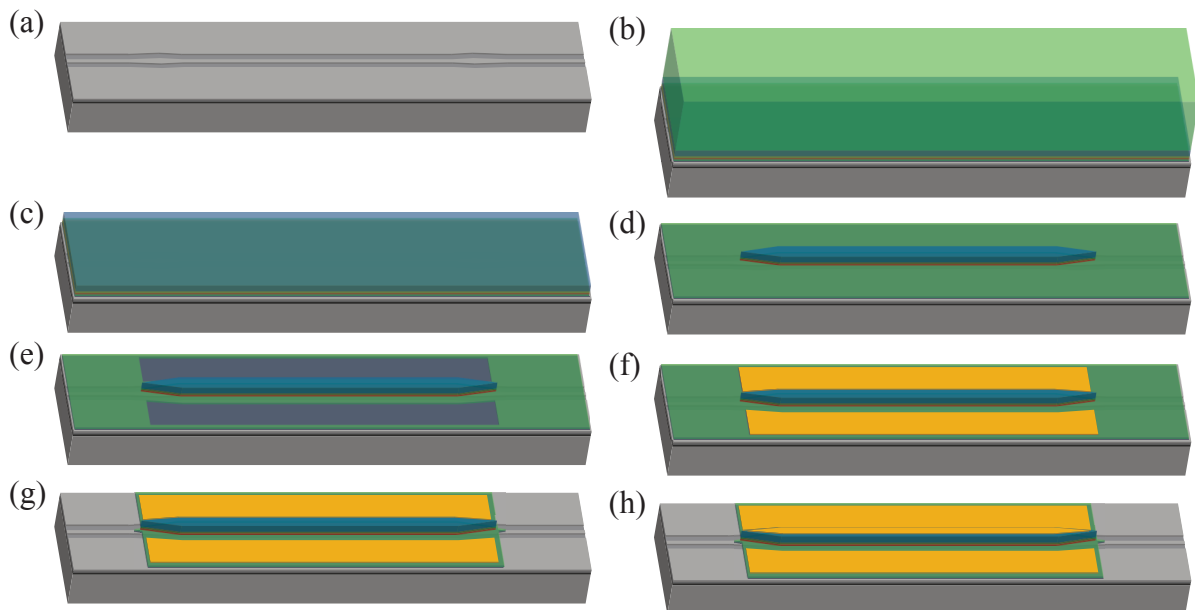


Figure 5.5: Simplified fabrication process flow for the integrated ICLs-on-SOI. Hard masks, via etches, and probe metals are not shown. (a) Beginning with an SOI wafer with $1.5 \mu\text{m}$ of silicon on top, Si waveguides are partially etched, and VOCs (not shown) are fully etched. (b) The ICL chip is flip-chip die-bonded to the Si. (c) The GaSb substrate is removed by mechanical lapping, followed by chemical etching. (d) The upper cladding, top SCH layer, and active ICL stages are etched to form a mesa above the Si waveguide. (e) The bottom SCH layer is selectively chemically-etched to reveal the bottom contact layer. (f) Ti/Pt/Au is deposited for bottom metal contacts. (g) The remaining III-V layers are etched. (h) Ti/Pt/Au is deposited for top metal contacts after SiN deposition and via etches.

chips are subjected to an O_2 plasma and manually fused together. The bonded chip is then placed in a graphite bonding fixture and annealed overnight in an oven. While the anneal for heterogeneously integrating InP-based active materials with Si is typically at $300\text{ }^\circ\text{C}$ for 1 hour, a lower temperature of $200\text{ }^\circ\text{C}$ was used for the ICL integration because the thermal expansion coefficient of GaSb is nearly three times larger than that of silicon. The GaSb substrate was then thinned by mechanical lapping to a thickness $\leq 100\text{ }\mu\text{m}$. The remaining substrate material was chemically etched in a $\text{CrO}_3:\text{HF}:\text{H}_2\text{O}$ solution that selectively stopped on the n-InAsSb etch stop layer. This etch stop layer was removed with a $\text{C}_6\text{H}_8\text{O}_7:\text{H}_2\text{O}_2$ solution, after which the underlying GaSb sacrificial layer was removed with a tetramethylammonium hydroxide (TMAH)-based developer.

A primary challenge in the fabrication of any heterogeneously-integrated laser is to etch the III-V mesa, but then stop precisely and uniformly within the thin bottom contact layer prior to deposition of the bottom metal. The desired etch depth can be reached using a slower ICP dry etch, either timed or with a laser end-point detection monitor. However, uniformity is a challenge since plasma etch rates often vary by as much as 20% across a die. To achieve the necessary uniformity, a selective dry or wet etch can be used to planarize the etch field. Although a variety of highly-selective wet chemical etches are available for processing InP-based devices, options for the GaSb material system are more limited.

The III-V mesas were defined with an SiO_2 hard mask. The upper contact, cladding, SCH, and a portion of the active region were removed with a first BCl_3 ICP etch step, using a laser end-point detection monitor. After the etch depth was confirmed, the exposed sidewalls were passivated with a 3 second $\text{H}_3\text{PO}_4:\text{H}_2\text{O}_2:\text{Tartaric Acid}$ etch, 15 nm atomic layer deposition (ALD) of Al_2O_3 , and plasma-enhanced chemical vapor deposition (PECVD) of SiN. The remainder of the active region was removed with a second ICP etch step, which stopped within the 600 nm-thick bottom GaSb SCH layer. Prior to

metallization, the remainder of the bottom SCH layer was removed with a TMAH-based developer that stopped at the top of the n-InAs/AlSb bottom contact layer. Ti/Pt/Au (20/150/1000 nm) was deposited for both bottom and top metal contacts. After the bottom metallization, the remaining III-V material was etched with a CH₄/H₂/Ar RIE to isolate individual devices, after which the lasers were encapsulated with 1125 nm of SiN deposited by PECVD. Finally, individual laser bars were diced and the silicon waveguide facets were mechanically polished.

Results

After fabrication, the laser bar on silicon was bonded with GE varnish to a copper sub-mount and the probe pads were contacted with wire bonds to inject current. The drive current source produced 250 ns pulses at a 1 kHz repetition rate. Digitized scope readings were averaged from 150–200 ns to measure the detector voltage. The output power emitted from the polished silicon waveguide facet was collected by an $f/1$ lens and imaged to overfill a fast 2x2 mm² HgCdTe detector element, which was not calibrated for quantitative determination of the peak powers of <1 mW.

Figure 5.6 shows the light intensity (in arbitrary units) and voltage vs. drive current (L-I-V) characteristics of Devices A and B when operated at room temperature (20 °C). Note first that the I-V curves show a rather soft turn-on. Although the precise output power could not be determined, the maximum output power collected from Devices A and B in this configuration were estimated to be near 0.5 and 0.1 mW, respectively, based on measurements performed on a different set-up. Device A had a threshold current of 423 mA (1.20 kA/cm²) while Device B had a slightly lower threshold current of 359 mA (1.45 kA/cm²). The threshold current for Device C was 561 mA (3.01 kA/cm²). These threshold current densities are substantially higher than typical room-temperature values

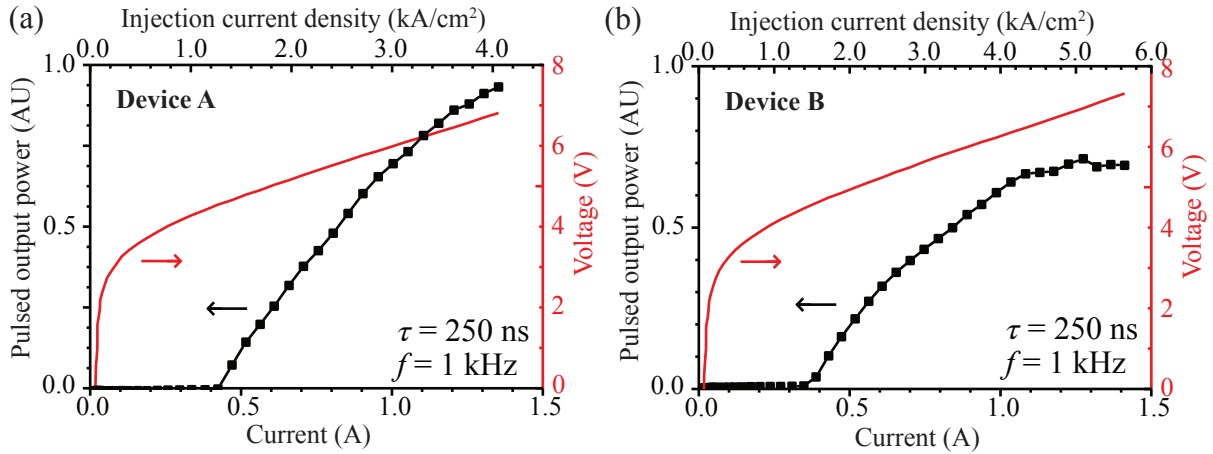


Figure 5.6: Single-sided pulsed output power (in arbitrary units) and voltage vs. drive current at 20 °C for $\lambda \approx 3.6 \mu\text{m}$ ICLs-on-SOI with 3.1 mm-long active regions. Light was collected from a passive silicon waveguide facet. The silicon waveguides under the active region were 1 μm wide and the III-V mesas were (a) 11 μm wide (Device A) and (b) 8 μm -wide (Device B).

of $\approx 150\text{--}300$ A/cm² for narrow-ridge ICLs processed on native GaSb substrates [15, 127], although the results for Devices A and B are comparable to those observed previously for Fabry-Perot QCLs on silicon [77]. Devices A and B both operated to above 40 °C.

Figure 5.7 shows the spectral characteristics for Devices A (green) and B (blue) with both tapers intact, as measured by a 0.5-m-long Digikrom monochromator with a resolution of 1.9 nm. Both spectra, with centroid wavelengths $\sim 3.64 \mu\text{m}$, display a pronounced longitudinal mode spacing of ~ 5 nm. This relatively large free-spectral range (FSR) indicates the presence of a cavity much shorter than the 3770 μm -long Fabry-Perot cavity formed by the two polished silicon facets, and also much shorter than the 3100 μm length of the hybrid gain region bounded by the two tapers. However, it corresponds closely to the calculated FSRs of 5.3/5.8 nm for the 350/320 μm -long passive silicon waveguide regions on opposite ends of the device (with simulated $n_g=3.58$). Apparently, a coupled cavity that includes one or both of these passive waveguides forms due to reflections between the III-V tapers and the polished silicon facets.

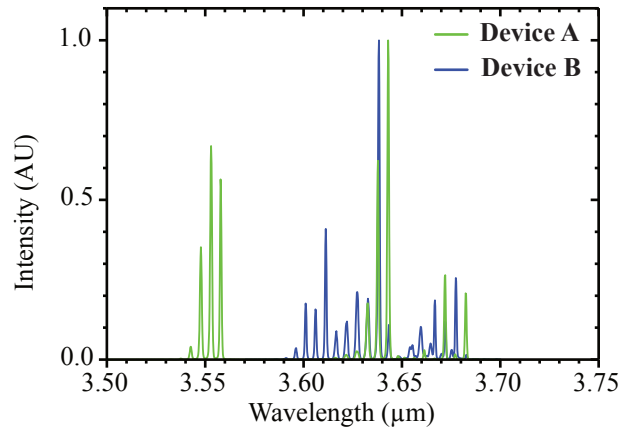


Figure 5.7: Emission spectra at 20 °C of two integrated $\lambda \approx 3.6 \mu\text{m}$ ICLs-on-SOI with 3.1 mm-long active regions. Devices A and B had 11 μm -wide and 8 μm -wide III-V mesas, respectively, and 1 μm -wide silicon waveguides. Light was collected from a passive silicon waveguide facet.

In studying the first generation of QCLs integrated on silicon, we observed that even though the active gain region was surrounded on both sides by III-V tapers, the primary lasing cavity was formed by reflections from the tapers rather than the silicon end facets [78]. The conjecture that the tapers in the present devices similarly display high reflection is consistent with the formation of a cavity between the taper and the end facet as well as with other observations that will be discussed below.

The same lasers were re-characterized after one taper was removed by mechanical polishing. This reduced the length of the active gain region (including the other taper) from 3100 to 2530 μm and allowed light to be collected from the polished hybrid III-V/Si facet. A 4-mm-diameter InSb detector with 5 μs time constant collected all the light transmitted by the f/1 imaging lens. In this configuration, the total output powers were reliably calibrated by analyzing the angular profile determined from far-field characterization of each output (Figure 5.10, below). The reported total power is adjusted to account for light not collected by the f/1 lens.

Figure 5.8(a) shows the room-temperature L-I characteristics for emission from the

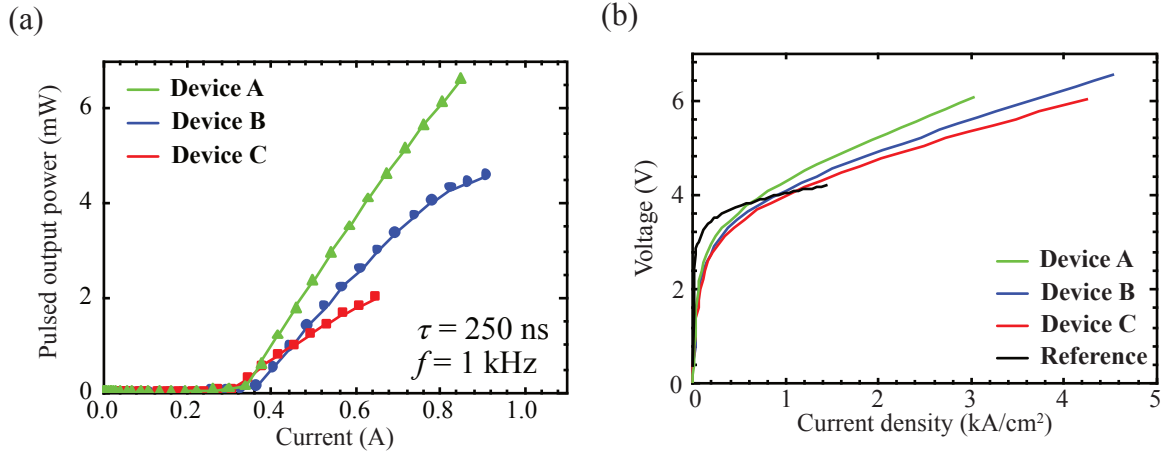


Figure 5.8: (a) Single-sided pulsed output power vs. drive current at 20 °C collected from a polished hybrid III-V/Si facet after taper removal of three $\lambda \approx 3.6$ μm ICLs-on-SOI. (b) Voltage vs. drive current density for Devices A, B, C, and a 32 μm -wide ICL ridge fabricated on a native GaSb substrate for reference. Devices A, B, and C had 11 μm , 8 μm , and 6 μm -wide III-V mesas, respectively. Devices A and B had 1 μm -wide silicon waveguides, while Device C had a 2 μm -wide silicon waveguide.

hybrid III-V/Si facets of all three devices. The slope efficiencies for Devices A/B/C (ridge widths 11/8/6 μm) are 13.7/10.1/6.6 mW/A, while the maximum (unsaturated) output powers are 6.6/4.6/2.0 mW. These powers and efficiencies are dramatically increased over the same devices before one taper was removed but still much lower than the typical efficiencies of >500 mW/A for 7-stage ICL ridges processed on native GaSb substrates [127].

The most striking aspect of the L-I characteristics in Figure 5.8(a) is that the threshold current is nominally independent of ridge width, i.e., all three values fall within the narrow range 0.31–0.36 A. This implies that the high thresholds are dominated by current leakage at the ridge sidewalls (the same for any ridge width), rather than by the current required to invert the carrier populations in the active quantum wells (increases linearly with ridge width). Sidewall leakage will be discussed further below.

It follows that the threshold current density increases rapidly with decreasing ridge width, with samples A/B/C displaying values of 1.1/1.7/1.9 kA/cm². The threshold

current densities after one taper was polished off differ from the devices with both tapers by $-7\%/+19\%/-40\%$, respectively. That is, the variation was minimal for Devices A and B, whereas the threshold for Device C decreased more significantly, implying a non-negligible loss induced by the taper. Again, these threshold current densities are much higher than typical values for 7-stage ICLs fabricated on native GaSb substrates [15, 127].

Figure 5.8(b) shows I-V characteristics for all three lasers, along with analogous data for a 7-stage ICL reference laser with $32\ \mu\text{m}$ ridge width and similar emission wavelength ($3.45\ \mu\text{m}$) that was fabricated on a native GaSb substrate (black curve). That the integrated ICLs show a noticeably softer turn-on than the reference device is again consistent with the presence of severe current leakage at the ridge sidewalls. This leakage may be attributed to the BCl_3 ICP used to etch through the active stages of the III-V mesas. Although native-substrate ICLs processed with the alternative $\text{CH}_4:\text{H}_2:\text{Cl}_2$ RIE usually display minimal sidewall leakage (as in the reference device) [127, 129], that dry-etch chemistry was not available to UCSB for the fabrication of these integrated devices. Previous ICL ridges fabricated at NRL on native substrates using the BCl_3 ICP etch chemistry have sometimes displayed minimal sidewall leakage [129], although on other occasions the sidewall currents have been quite substantial, as in the present devices. When NRL characterized native-substrate ICL test devices, that were processed by UCSB using the BCl_3 ICP etch chemistry prior to processing the integrated devices on silicon, the results confirmed sidewall leakage currents much lower than those indicated by the present data for integrated devices.

The slopes of the three I-V curves above threshold correspond to series resistances in the range $3.1\text{--}3.8\ \Omega$, which are clearly higher than for the reference device. Transmission line measurements during fabrication estimated that the bottom metal contact resistivity and sheet resistance are $4 \times 10^{-4}\ \Omega\text{-cm}^2$ and $340\ \Omega/\text{sq}$, respectively. These values correspond to $1.0\ \Omega$ of series resistance added by the contacts and lateral current path in the

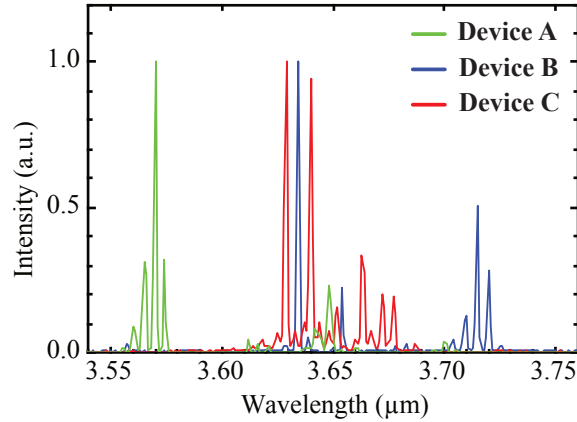


Figure 5.9: Emission spectra, collected from a polished hybrid III-V/Si facet at 20 °C, of three $\lambda \approx 3.6 \mu\text{m}$ ICLs-on-SOI after taper removal. Devices A, B, and C had 11 μm , 8 μm , and 6 μm -wide III-V mesas, respectively. Devices A and B had 1 μm -wide silicon waveguides, while Device C had a 2 μm -wide silicon waveguide.

bottom n-InAs/AlSb layer. However, the top contact resistivity of $4 \times 10^{-6} \Omega\text{-cm}^2$ adds $< 0.1 \Omega$ to the series resistance.

Figure 5.9 shows the emission spectra at 20 °C for all three devices with one taper removed. Note that the mode spacing of $\sim 5 \text{ nm}$ is preserved, meaning that there is still coupling to the remaining passive silicon cavity at the other end of the laser. A widely separated grouping of modes (e.g., emission from Device A around 3.57 and 3.65 μm) also appears, both before and after the taper is removed. One possibility is an additional very short cavity with long FSR, such as a cavity formed by multiple reflections within the 50 nm-long tapering regions. More generally, the result may be explained by a wavelength-dependent taper reflectivity.

Figure 5.10 shows measured (solid) and simulated (dashed) far-field profiles along the slow axis, for emission from the hybrid III-V/Si facets of all three devices. The dual lobes indicate emission primarily in the higher-order TE_{10} mode. The profile for the narrowest ridge (Device C), with its symmetric shape and deepest central null, agrees well with the simulated TE_{10} profile. The contrasting absence of a complete central null for Devices

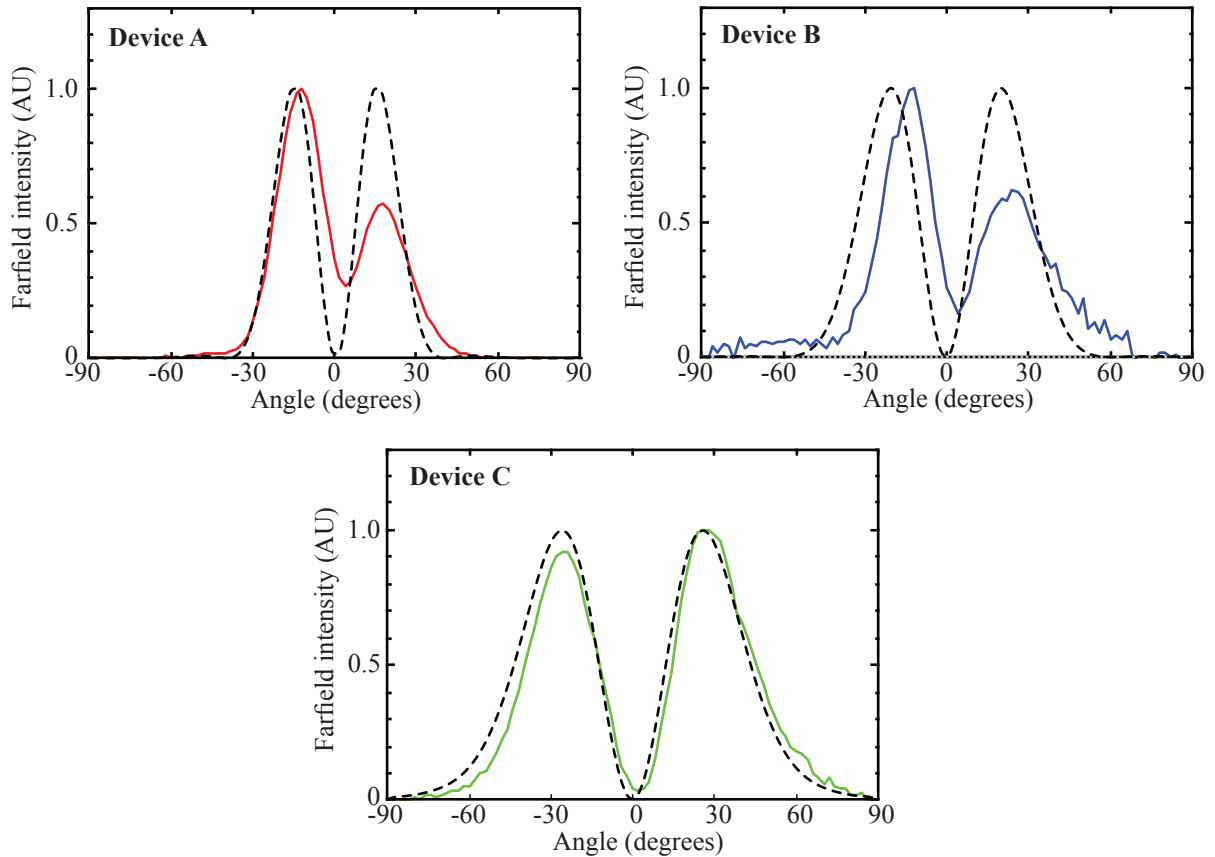


Figure 5.10: Far field intensity as a function of the angle normal to the facet in the slow (horizontal) axis of three $\lambda \approx 3.6 \mu\text{m}$ ICLs-on-SOI, measured from polished hybrid III-V/Si facets. Solid lines indicate measured profiles and dashed lines indicate simulated TE_{10} profiles. Measurements were taken at 20°C and a drive current of 640 mA (Devices A and C) and 700 mA (Device B). Devices A, B, and C had $11 \mu\text{m}$, $8 \mu\text{m}$, and $6 \mu\text{m}$ -wide III-V mesas, respectively. Devices A and B had $1 \mu\text{m}$ -wide silicon waveguides, while Device C had a $2 \mu\text{m}$ -wide silicon waveguide.

A and B may indicate additional emission in the TE_{00} mode (approximately Gaussian with a single lobe). The notable horizontal asymmetry of the data for Devices A and B may be due to an offset of the emission angle of the two modes with different effective indices. This could result from a slight angle in the polished facet with respect to the waveguide ridge, or to an asymmetry in the waveguides refractive index profile at the facet associated with residue or the generally low quality of the polished facet.

An SEM examination of the III-V/Si hybrid facets after one taper was polished off revealed a high degree of roughness, and even some separation between the III-V and silicon layers. This is likely to have contributed additional loss at the polished facet, although apparently not as much as the loss at the tapers because the lasing threshold for Device C decreased substantially when one taper was replaced by a polished facet. It will be seen below that Devices A and B also lased to a higher temperature after the taper was removed.

These data imply a mismatch of the dominant modes on opposite sides of the tapers, since the far-field data show primarily a TE_{10} mode in the hybrid gain region, whereas the simulations indicate that only the TE_{00} mode is supported on the silicon waveguide side of the tapers. Due to the mode mismatch, we expect the tapers to reflect most of the light reaching them (in addition to scattering and absorption losses) rather than transmitting it. This is consistent with the very low differential efficiencies observed for emission from the silicon waveguide before a taper was removed. In this context, it seems somewhat surprising that the FSRs in the spectral data show evidence for coupling between the two cavities. It may be that mode mixing in the intermediate tapered regions induces the coupling.

A further question is why the TE_{10} mode is selected for lasing according to the far-field data, when the TE_{00} mode should have lower sidewall scattering loss as well as greater feedback from the silicon waveguides beyond the tapers (we pointed out above

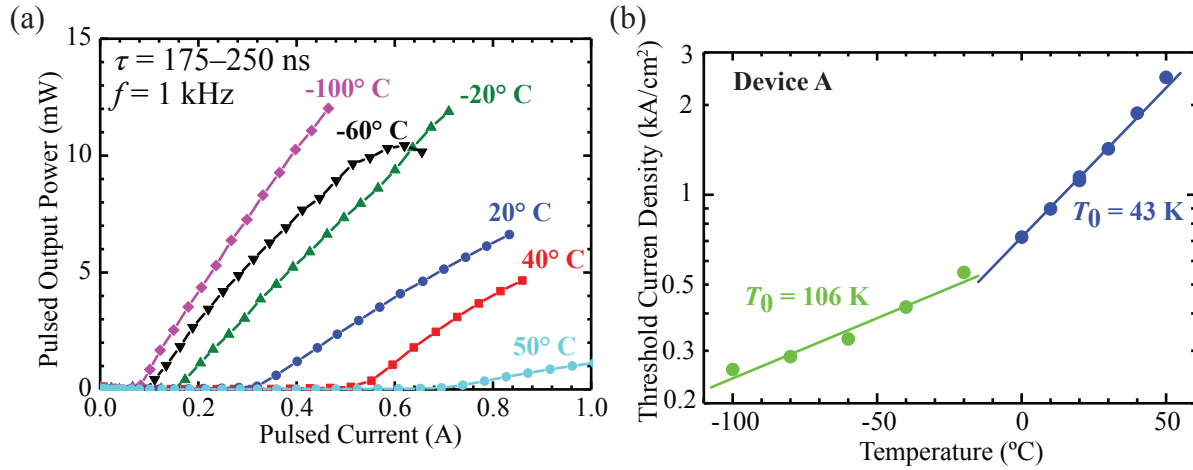


Figure 5.11: (a) Single-sided output power vs. drive current of a $\lambda \approx 3.6\ \mu\text{m}$ ICL-on-SOI (Device A with an $11\ \mu\text{m}$ -wide III-V mesa and a $1\ \mu\text{m}$ -wide silicon waveguide) at temperatures ranging from $-100\ ^\circ\text{C}$ to $50\ ^\circ\text{C}$ after taper removal. (b) Threshold current density vs. temperature. The characteristic temperatures are separately calculated for lower temperatures $-100\text{--} -20\ ^\circ\text{C}$ (green, $T_0 = 106\text{ K}$) and higher temperatures $0\text{--}50\ ^\circ\text{C}$ (blue, $T_0 = 43\text{ K}$).

that the calculated optical confinement factors are effectively equal). This may be related to the excessive sidewall leakage that causes a large fraction of the current to flow down the edge of the ridge rather than within its interior. It is well known the surface of an InAs-rich epitaxial layer pins within the conduction band, which induces band bending and strong surface conduction. The surface conduction is quite sensitive to the etching and/or passivation procedures used to form the mesa [130]. Both the active electron wells and electron injector in each active stage of an ICL contain InAs layers [15] that are prone to surface conduction. With much more current flowing at the ridge sidewalls, gain may occur at the outer edges of the ridge before sufficient current to produce gain flows within the interior (where there may still be a net loss). This double-lobed gain profile would favor lasing in the TE_{10} rather than TE_{00} mode and the effect may be greatest in the narrowest ridge where sidewall leakage is the most prominent.

All three devices were characterized in the thermoelectric-cooler range of $10\text{--}50\ ^\circ\text{C}$,

while Device A was also measured down to $-100\text{ }^{\circ}\text{C}$ in a liquid-nitrogen-cooled cryostat. Figure 5.11(a) shows the pulsed L-I characteristics of Device A over the entire temperature range. Lasing was observed to $50\text{ }^{\circ}\text{C}$, which is $10\text{ }^{\circ}\text{C}$ higher than before the taper was removed. At $-100\text{ }^{\circ}\text{C}$, it produced up to 12.0 mW before any appreciable rollover. For $T = -60\text{ }^{\circ}\text{C}$, the decreasing output at the highest current is probably associated with an optical mode hop rather than thermal rollover, since no analogous rollover is observed at either higher or lower temperatures in the same current range

Using the threshold current density as a function of temperature in Figure 5.11(b), we extract a characteristic temperature of $T_0 = 43\text{ }^{\circ}\text{C}$ from an exponential fit to the higher-temperature data ($0\text{--}50\text{ }^{\circ}\text{C}$). At cryogenic temperatures, there is less improvement in the threshold with decreasing T . Devices B and C lased up to $50\text{ }^{\circ}\text{C}$ and $40\text{ }^{\circ}\text{C}$, respectively, and showed similar characteristic temperatures of $T_0 = 43$ and $37\text{ }^{\circ}\text{C}$, respectively, for the higher temperature range. These values are only slightly lower than the typical results of $\sim 45\text{--}50\text{ K}$ for optimized ICLs fabricated on native substrates. A fit to the slope efficiency vs. temperature for Device A over the range $10\text{--}50\text{ }^{\circ}\text{C}$ yields $T_1 = 71\text{ K}$. These characteristic temperatures indicate that CW operation should be feasible once the threshold current density is reduced.

Figure 5.12 plots the threshold voltage of Device A as a function of temperature. V_{th} in an ICL typically increases at lower temperatures where the minimum voltage per stage (the photon energy) is higher and there is also less thermally-assisted transport. An increase is also expected at higher temperatures, where the increasing threshold current drops across the series resistance. However, the minimum V_{th} of $\approx 4.1\text{ V}$ at intermediate temperatures is somewhat higher than the more typical value of $\approx 3.6\text{ V}$ for a 7-stage ICL emitting at this wavelength. The series resistance of the bottom contacts is higher, combined with the elevated threshold current density associated with sidewall leakage.

The spectral characteristics of Device A were also measured at temperatures from -100

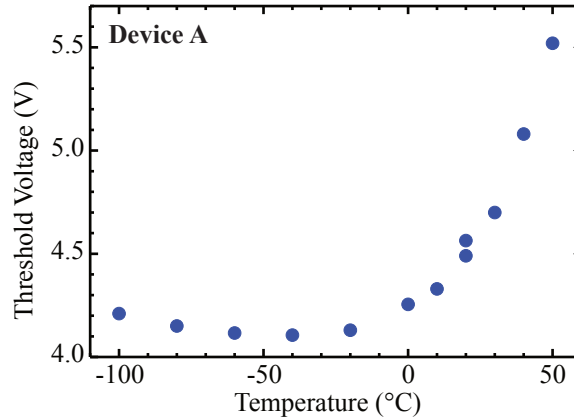


Figure 5.12: Pulsed threshold voltage vs. temperature for a $\lambda \approx 3.6 \mu\text{m}$ ICL-on-SOI with an $11 \mu\text{m}$ -wide III-V mesa and a $1 \mu\text{m}$ -wide silicon waveguide (Device A).

$^{\circ}\text{C}$ to 50°C . The results shown in Figure 5.13(a) indicate the usual redshift with increasing temperature, which is quantified in the plot of centroid wavelength vs. temperature in Figure 5.13(b). The tuning rate of $2.4 \text{ nm}/^{\circ}\text{C}$ is consistent with the expected shift of the gain peak, as governed by the bandgap. The periodic longitudinal modes with $\text{FSR} \approx 5 \text{ nm}$ are observed at all temperatures, with individual modes shifting at the thermo-optic rate of $\approx 1 \text{ nm}/^{\circ}\text{C}$. We also note an apparent systematic clumping of the modes, which becomes more obvious when the spectra for $T = 10\text{--}50^{\circ}\text{C}$ are presented over a finer grid of temperatures in Figure 5.13(c). The clump spacing of $\sim 40\text{--}50 \text{ nm}$ is consistent with the possibility that reflections at multiple points within the tapering region form an additional short cavity of length $20\text{--}50 \mu\text{m}$. The spectra for Sample B show a similar clumping, with period $\approx 40 \text{ nm}$.

5.2 Conclusion and Summary

A few primary issues were identified to be limiting the laser performance. First, while the TE_{10} optical mode dominates the lasing in in the hybrid III-V/Si gain region,

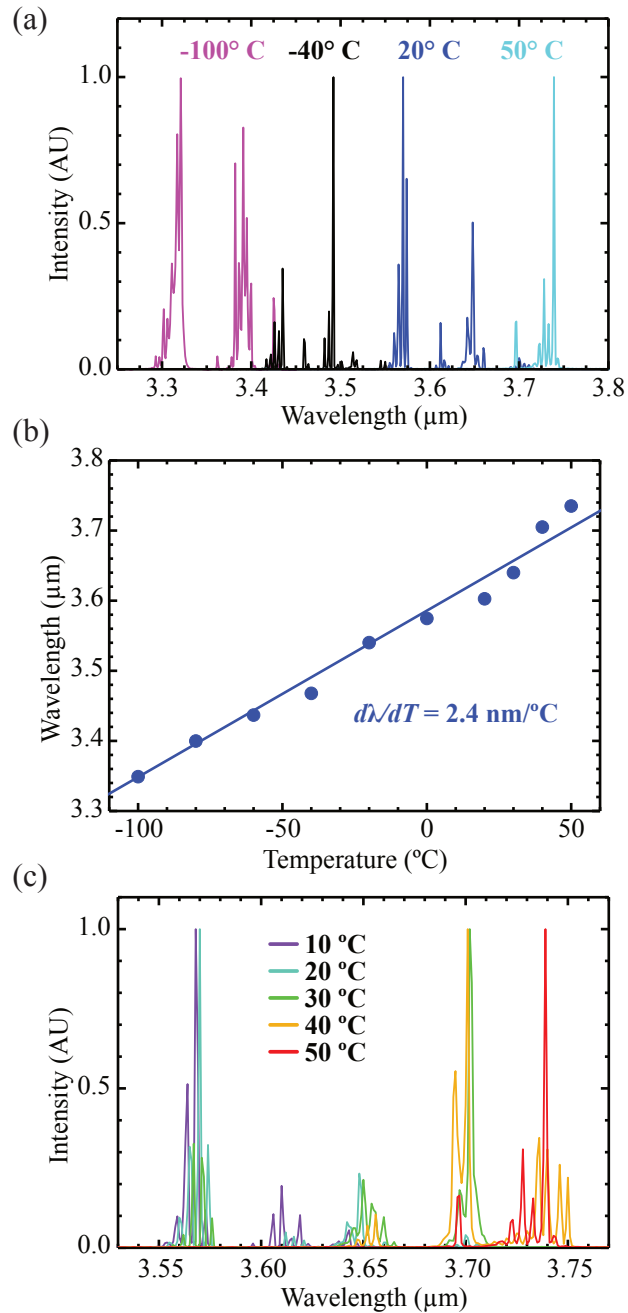


Figure 5.13: Emission spectra measured from a polished hybrid III-V/Si facet of a $\lambda \approx 3.6 \mu\text{m}$ ICL-on-SOI with an $11 \mu\text{m}$ -wide III-V mesa and a $1 \mu\text{m}$ -wide silicon waveguide (Device A) at (a) a broad temperature range -100°C to 50°C and (c) a narrow temperature range 10°C to 50°C . (b) Peak wavelength vs. temperature of Device A.

only the TE_{00} mode is supported in the silicon waveguides that ideally form part of the Fabry-Perot lasing cavity. Because of the mode mismatch, the tapers induce reflection and loss rather than efficient coupling between the hybrid and silicon waveguide sections. When one of the tapers is removed and the emission is from a polished hybrid facet, the efficiency increases by more than an order of magnitude, despite very poor hybrid III-V/Si facet quality. The maximum pulsed operating temperature also increased, by 10–20 °C

The mode mismatch may be partially caused by the presence of severe sidewall leakage currents, which are evident in both the invariance of the threshold current with ridge width and the very soft turn-on in the I-V characteristics of all three devices. The much higher current density at and near the outer edges of the ridge appears to favor lasing in the TE_{10} mode rather than the fundamental (which has less intensity near the ridge sidewalls). Presumably, the BCl_3 ICP dry etch used to define the mesas produced an unfavorable surface quality that induced the leakage. In the next generation of integrated ICLs, this etch will be modified or replaced with $CH_4:H_2:Cl_2$ RIE. A much lower threshold current density will naturally make CW operation much more straightforward to attain.

Once the emitted light is primarily in the TE_{00} mode, it may be possible to further enhance the III-V taper coupling efficiency by engineering the optical mode to reside more in the silicon portion of the hybrid III-V/Si waveguide. This can be accomplished by reducing the separate confinement layer thickness in the ICL design. The gain in an ICL is high enough that a reduced optical confinement factor is acceptable, as long as the loss in the silicon is sufficiently low.

There appears to be no fundamental reason why ICLs integrated on silicon, with flip-chip bonding to provide CW operation, should not exhibit performance rivaling that of the optimized devices fabricated on native substrates. The first QCLs on silicon already operate at threshold current densities of ≈ 1 kA/cm² [77, 78], which is roughly at the

state of the art for native-substrate devices, although the slope and wallplug efficiencies still require improvement.

Summarizing, we have demonstrated the first interband cascade lasers integrated on a silicon substrate. The heterogeneously-integrated devices with ridge widths of 6–11 μm emit at $\lambda \approx 3.65 \mu\text{m}$ and operate up to 50 $^{\circ}\text{C}$ in pulsed mode. At 20 $^{\circ}\text{C}$, the threshold current density is as low as 1.1 kA/cm^2 , and up to 6.6 mW (unsaturated) of peak power is emitted from a hybrid III-V/Si facet. For the widest ridge at temperatures above 10 $^{\circ}\text{C}$, the characteristic temperatures for threshold and slope efficiency are $T_0 = 43 \text{ }^{\circ}\text{C}$ and $T_1 = 71 \text{ }^{\circ}\text{C}$, respectively. Based on the minimum threshold power density of 5 kW/cm^2 and these characteristic temperatures, it appears likely that CW operation will be possible once more robust thermal dissipation is provided by flip-chip bonding.

Chapter 6

III-V Tapers

A prominent challenge in constructing heterogeneously integrated lasers is to efficiently transfer the light generated within the III-V active region into a passive silicon waveguide. A few schemes are possible, but the most common is to terminate the III-V region by tapering the mesa to a point. Ring lasers, where the III-V mesa is in a ring configuration and does not terminate, have also been demonstrated at near-infrared wavelengths [131]. In this case, light is evanescently transferred to a neighboring silicon bus waveguide. All of the lasers described within this dissertation use an adiabatic III-V taper as a mode converter to couple light from a hybrid III-V/Si mode into the underlying silicon waveguide mode. As concluded in previous sections, the III-V taper performance is one of the primary factors contributing to the overall laser performance. In this Chapter, heterogeneously integrated lasers which include III-V tapers are discussed and analyzed.

6.1 Three-Section Lasers With Tapers

The lasers in this dissertation all consist of a hybrid Si/III-V active region coupled on both sides to passive silicon waveguides. The interface between each of these regions

can cause transmission loss or reflections.

Taper transmission and reflection are related but separate issues with very different effects on laser performance. For Fabry-Perot lasers, the taper is a part of the Fabry-Perot laser cavity, and therefore any transmission loss through the taper is part of the internal loss of the laser. In the absence of taper reflection, the analysis is relatively simple. The total average internal loss equates to:

$$\langle \alpha_i \rangle = \frac{L_a \langle \alpha_a \rangle}{L_a + L_p + 2L_t} + \frac{L_p \langle \alpha_p \rangle}{L_a + L_p + 2L_t} + \frac{2L_t \alpha_t}{L_a + L_p + 2L_t}$$

where L_a and L_p are the respective total lengths of the passive and active regions, L_t is the length of one taper, and α_a , α_p , and α_t are the losses of the active, passive, and taper regions in cm^{-1} . Additional internal loss contributed by the taper regions is

$$\frac{2L_t \alpha_t}{L_{total}} \approx \frac{2\alpha_{t,dB}}{4.34L_{total}} \approx \frac{0.46\alpha_{t,dB}}{L_{total}}$$

where $\alpha_{t,dB}$ is the optical power lost per pass when the optical mode couples through the taper, in dB.

The threshold current is proportional to

$$I_{th} \propto e^{2(\langle \alpha_i \rangle + \alpha_m)/g_{0N}}$$

where g_{0N} is the gain coefficient [120]. The impact of the taper loss on the threshold current is then proportional to

$$\Delta I_{th} \propto \exp\left(\frac{0.92}{g_{0N}} \frac{\alpha_{t,dB}}{L_{total}}\right)$$

Because the tapers are discrete elements within the laser cavity, their impact on the total internal loss of the laser, and therefore the required gain to reach threshold, is

inversely proportional to the length of the laser. Furthermore and intuitively, the impact is mitigated by a larger gain coefficient, g_{0N} .

Taper reflection complicates the situation. The 3-section passive-active-passive laser must be treated as a coupled-cavity system. By applying a matrix element model, each side of the laser can be treated with an effective reflectivity [120], r_{eff} , which takes into account the taper reflectivity, r_t , taper transmission coefficient, t_t , passive region loss (contained within the complex propagation constant, $\tilde{\beta}_p$), and silicon end facet reflectivity, r_f :

$$r_{eff} = r_t + \frac{t_t^2 r_f e^{-2j\tilde{\beta}_p L_p}}{1 + r_f r_t e^{-2j\tilde{\beta}_p L_p}}$$

Taper reflectivity therefore can increase the maximum effective mirror reflectivity of each side of the laser, but with a wavelength-dependent feedback caused by the cavity coupling. Note that for cases where the taper reflectivity is high compared to the product $t_t^2 r_f$ (e.g. very poor taper transmission and high taper reflectivity), the effective reflectivity will be dominated by the reflection off of the taper rather than the silicon end facet. Very little feedback from the tapers is necessary to produce a wavelength-dependent mirror reflectivity strong enough to enforce the filtering of Fabry-Perot modes.

If the effective reflectivity is too low, the total cavity loss may prohibit lasing. This can occur in a situation where the taper reflectivity and the taper transmission coefficient are both extremely low. As we observed with both the Fabry-Perot QCLs in Chapter 4.2 and the ICLs in 5, a high enough taper reflectivity will provide a high enough effective reflectivity to allow lasing to occur, regardless of the loss induced by the tapers.

For the DFB lasers, the situation changes dramatically. Because the laser cavity is entirely contained in between the III-V tapers, the tapers do not introduce internal loss to the primary laser cavity. The DFB gratings used for the lasers in this dissertation

provided relatively strong feedback. This allows a low threshold current density to be achieved, while the taper inefficiency primarily serves to reduce the laser power output. For this reason, DFBs can be used to mostly isolate the transmission performance of the tapers within the observed output power, in order to compare lasers with different III-V taper designs. Feedback from the taper tips can still occur, undesirably filtering DFB lasing modes and preventing single-wavelength operation, as was observed with the QCLs in Chapter 4.3.

Although the previous discussion provides some intuition regarding the performance of the heterogeneously integrated lasers within this dissertation, in reality, the situation is more complex. The tapers themselves are not abrupt interfaces, but continuous sections of III-V/Si active region with gain, loss, and an adiabatically (ideally) changing effective modal index. Reflections from the tapers may occur at the taper tip, or at multiple points within the taper. The effective reflectivity can therefore potentially be wavelength dependent.

The laser metallization is designed with the intention of electrically pumping the entire extent of the III-V mesa including the tapered III-V regions, which should provide gain. Some observations of near-infrared heterogeneously integrated p-i-n lasers have concluded that the tapers are not entirely electrically pumped, and are therefore contribute to optical loss rather than gain. One possible cause is hydrogen passivation of the p-InP in the narrow upper cladding of the mesa within the taper region. Although this has not been investigated for any of the lasers in this dissertation, the 2.0 μm p-i-n lasers in Chapter 3 may suffer from the same issue. QCLs and ICLs, however, consist entirely of n-type semiconductor material and current spreading in the active stages of both QCLs and ICLs is significant. Additionally, because QCLs are unipolar devices with only electrons intentionally injected, the primary loss mechanism of an unpumped QCL mesa is free-carrier absorption rather than interband absorption. Therefore, the loss of

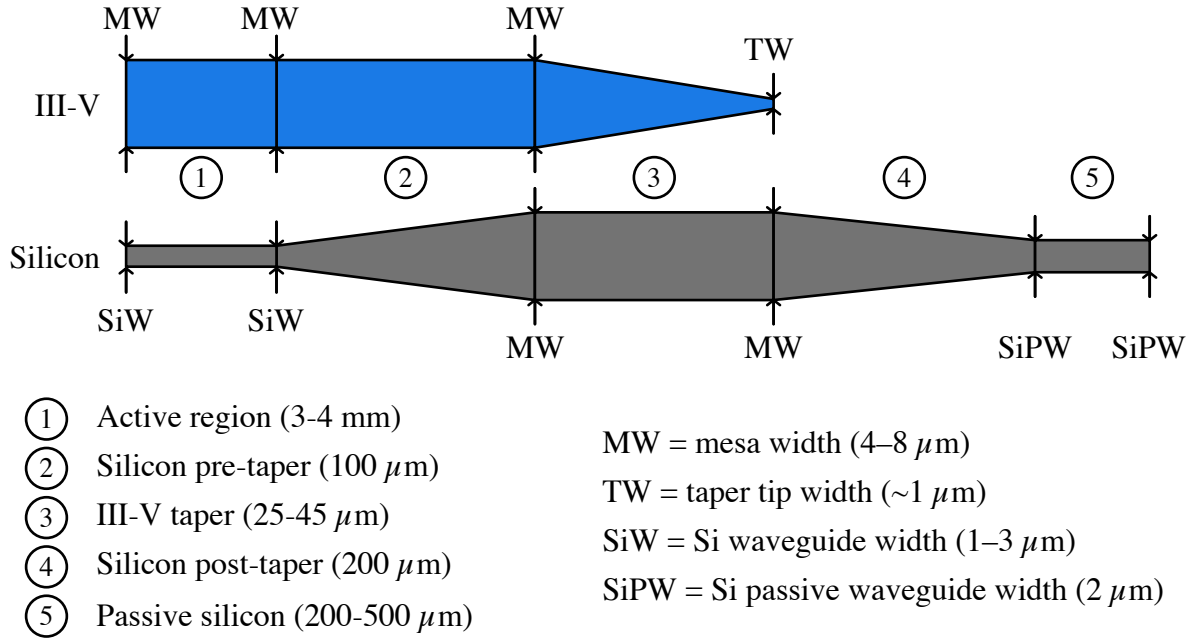


Figure 6.1: Top-down schematic of the silicon waveguide and III-V mesas during the taper section of the QCLs-on-SONOI described in this dissertation.

an unpumped region of QCL mesa is significantly lower than that of an unpumped ICL or diode mesa.

6.2 Taper Design

The general design of the devices used for the first generation Fabry-Perot and DFB QCLs in Chapter 4 are shown in Figure 6.1.

The III-V layers of diode lasers, QCLs, and ICLs have significantly different epilayer refractive index profiles and must therefore be designed individually for each laser. While the active region compositions chosen for the lasers demonstrated here (i.e. diode quantum wells and QCL/ICL stages) are mature designs, the complete epilayer stacks are each first generation designs.

Figure 6.2 shows a contour plot of the refractive index of the fundamental TM_{00} mode

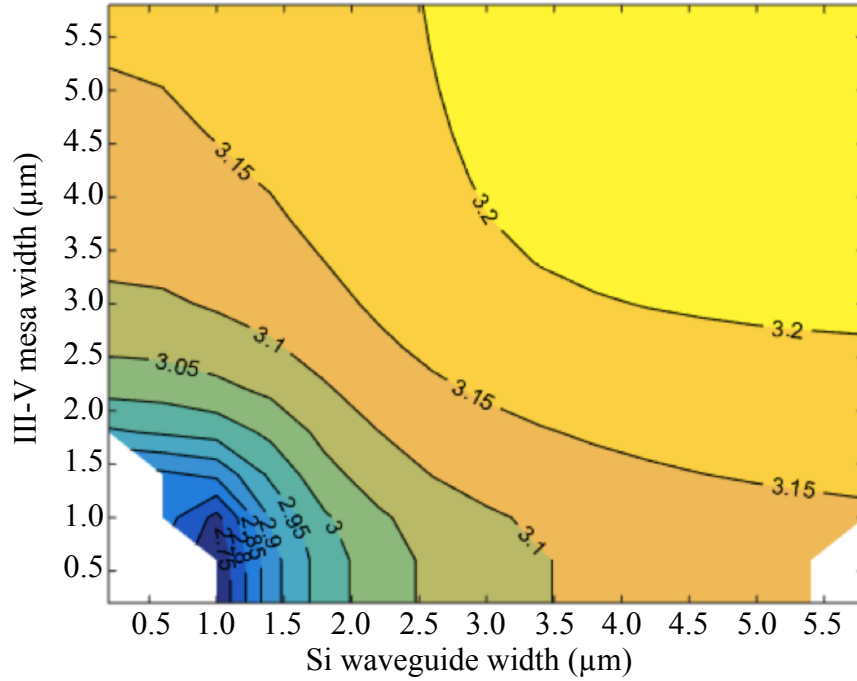


Figure 6.2: Contour plot of the effective index of the fundamental TM_{00} mode in the active region of a QCL-on-SONOI, as a function of the silicon waveguide and III-V mesa widths.

in the hybrid III-V/Si active region, as a function of both silicon waveguide and III-V mesa widths. The taper must effectively couple the fundamental TM mode within the hybrid III-V/Si region (the top of the plot with a $6 \mu\text{m}$ wide mesa) to a passive silicon waveguide (the bottom of the plot where the III-V mesa width is 0). If the transition across the effective index profile is slow enough, the mode will couple adiabatically, but reflections and transmission loss will become problematic for large effective index differentials, dn_{eff}/dz . For tapering profiles with a larger effective index differential, a longer taper will be required.

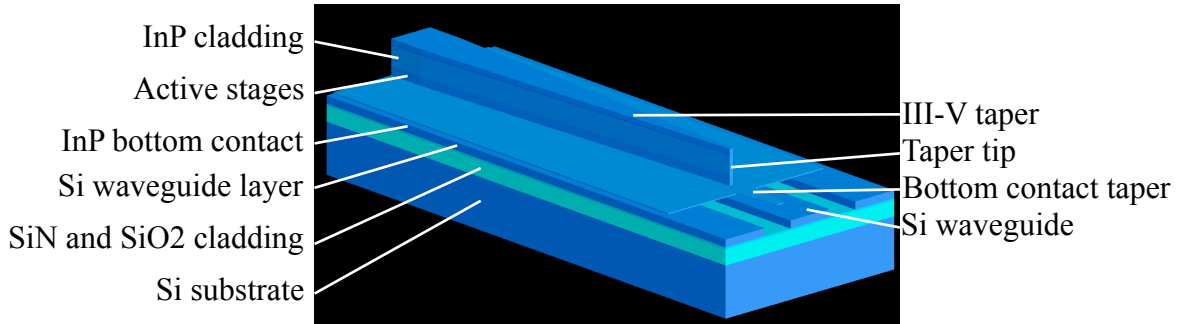


Figure 6.3: 3D image of the QCL-on-SONOI taper structure simulated in FDTD.

6.3 FDTD Taper Analysis

Finite difference time domain (FDTD) simulations of the optical mode propagation through the III-V taper region were performed. For the following simulations, both taper transmission and reflection were analyzed. The simple taper design described in the previous Section 6.2 was simulated. A 3-dimensional model of the taper simulation is shown in Figure 6.3.

Note that some numerical errors are present due to the limited mesh size used in the FDTD simulation in order to avoid impractical computation times. The general trends are accurate for smaller mesh sizes but a higher uncertainty is present particularly for some of the reflection values lower than about -40 dB.

Figure 6.4 shows contour plots illustrating the impact of taper length and taper tip width on reflection (left) and transmission loss (right). Figure 6.5 plots the reflection ((a) and (b)) and transmission ((c) and (d)) trends separately. The relatively long mid-infrared wavelengths compared to near-infrared wavelengths increase the tolerance of wider taper tips. For sufficiently long tapers, the taper tip can be as wide as 1.0–1.5 μm without introducing more than 0.5 dB transmission loss. Similarly, for lower than -30 dB reflection, the taper tip must be narrower 1.5 μm wide. For wider taper tips, the reflection has little dependence on the length of the taper. For a given taper tip width, little

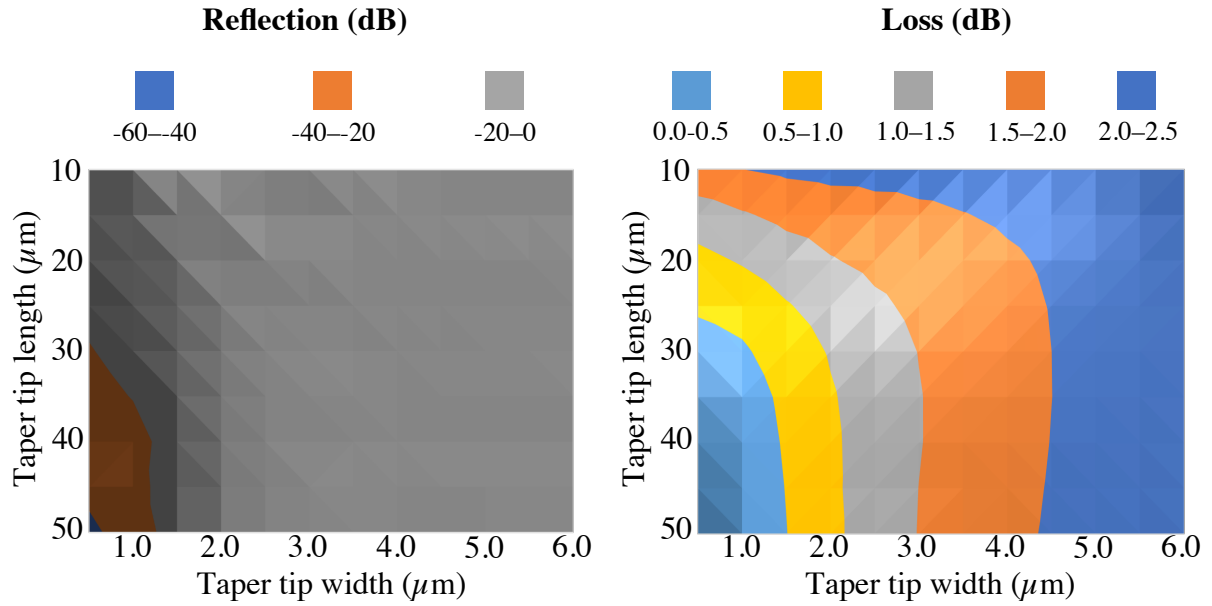


Figure 6.4: Contour plots showing reflection (left) and loss (right) induced by the taper of a QCL-on-SONOI, according to FDTD simulations.

improvement in the transmission is seen for tapers longer than $\sim 35 \mu\text{m}$, but narrower taper tips less than $1.5 \mu\text{m}$ continue to see improvements with longer tapers. According to these simulations, to truly isolate the laser from taper reflections, a conservative design rule is to target $< 1 \mu\text{m}$ wide taper tips. Longer tapers will theoretically always perform better, but at least $35 \mu\text{m}$ is necessary to avoid unnecessary losses.

Alignments between lithographic layers of better than 100 nm are achievable with local alignment in the GCA 200 autostepper housed in the UCSB Nanofabrication facility, which was used for the III-V layer processing steps during fabrication of the devices in this manuscript. In some cases, optimal alignment was not achieved and greater than 500 nm misalignment may have occurred. Figure 6.6 shows the impact of lateral misalignment of the III-V tapers with the underlying silicon waveguide. The extreme case of $1 \mu\text{m}$ misalignment, only contributes an additional 0.5 dB of transmission. The impact of misalignment on reflection is enhanced for narrower taper tips, but can still be easily

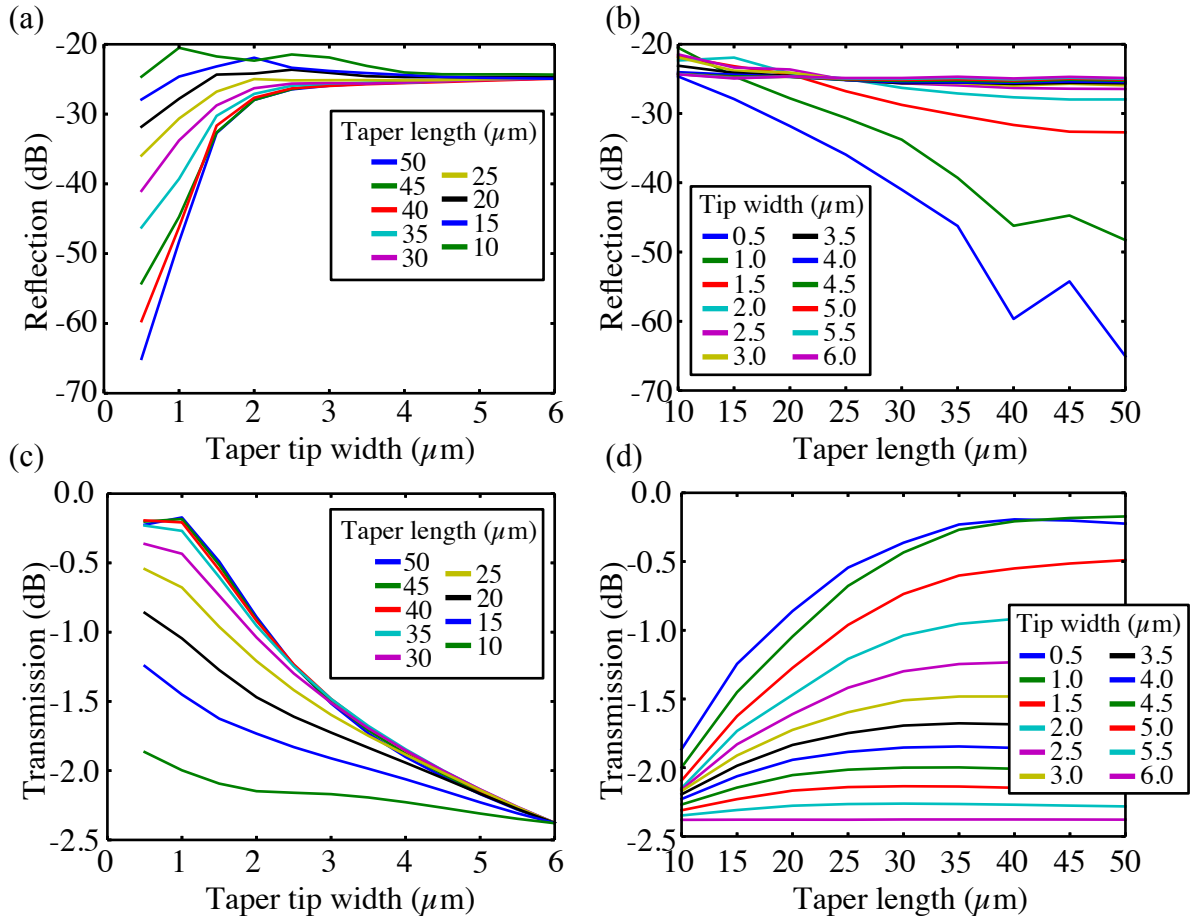


Figure 6.5: Plots showing (a) taper reflection as a function of taper tip width, (b) taper reflection as a function of taper length, (c) taper transmission as a function of taper tip width, and (d) taper transmission as a function of taper length for a QCL-on-SONOI taper.

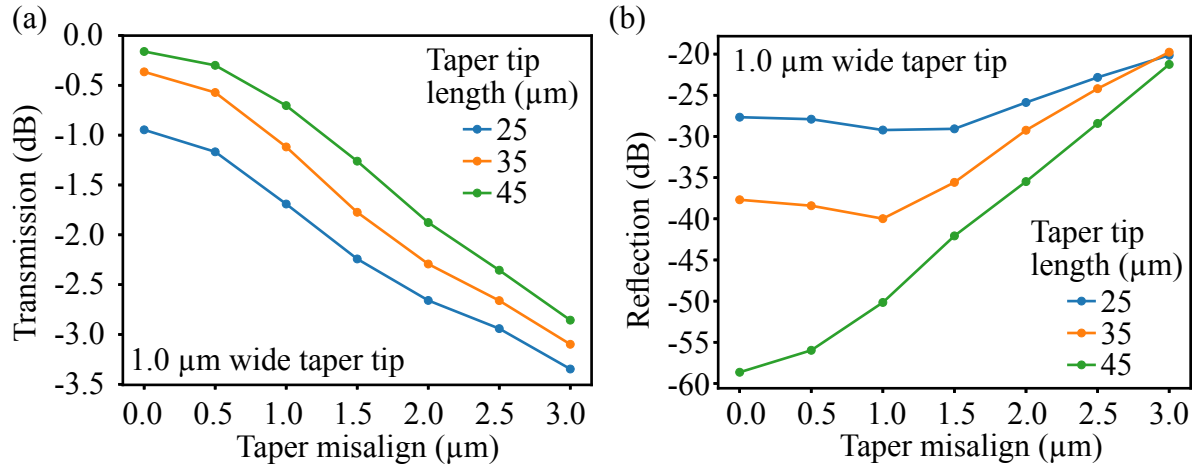


Figure 6.6: Simulated transmission (a) and reflection (b) of a QCL-on-SONOI taper as a function of misalignment of the III-V taper with respect to the silicon waveguide.

maintained below -45 dB for a 45 μm long taper with a tip narrower than 1 μm .

Reducing the number of QCL stages is one effective way to improve the taper transmission efficiency. Figure 6.7 shows the impact of the number of QCL stages on the taper performance, where fewer stages slightly improves the transmission and reduces the reflection for a given taper tip width. All of the QCLs within this dissertation used an active region with 30 stages. Obviously reducing the number of stages will have an important impact on the gain and active region modal overlap. However, fewer stages encourages more coupling of the optical mode with the silicon waveguide and it is possible that for fewer stages, the net modal gain remains similar as less optical confinement will be in the III-V cladding and contact regions which should have a higher optical loss than the silicon waveguide.

6.4 Conclusion and Summary

This chapter covered a general theoretical review of the impact of the III-V taper reflections and losses on the heterogeneously integrated laser performance. 3-D FDTD

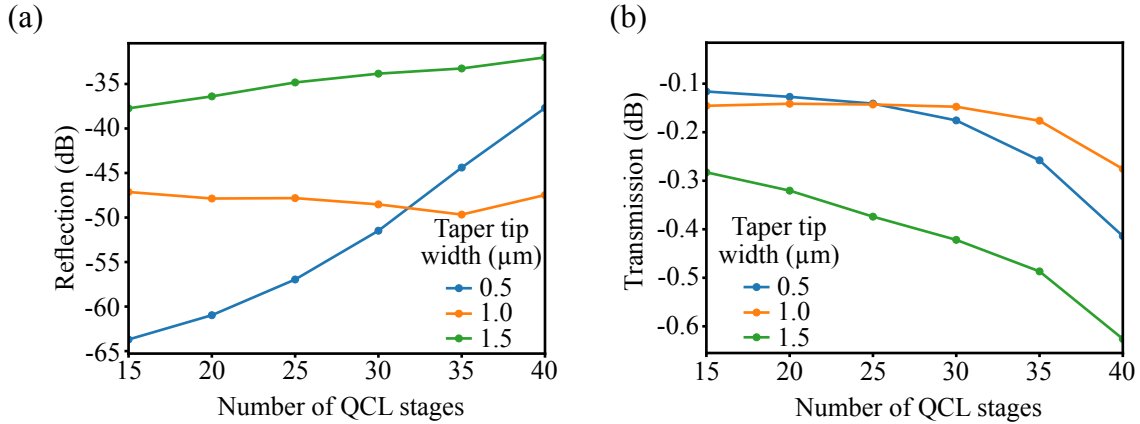


Figure 6.7: Simulated transmission (a) and reflection (b) of a 45 μm long taper of a QCL-on-SONOI as a function of the number of QCL stages.

simulations were performed on the QCL tapers used in Chapter 4.

In summary, FDTD simulations predict that good performance can be obtained from III-V tapers which are at least 35 μm long and have a taper tip narrower than $\sim 1 \mu\text{m}$. Reasonable lithographic misalignment of the tapers and the underlying silicon waveguide does not appear to have a detrimental effect on the transmission or reflection. Experimental observations show up to ~ 12 dB loss from the taper transition of a DFB QCL, which is much worse performance than predicted by the simulations. Most likely, the additional loss should be attributed to sidewall and taper-tip scattering, and material absorption near the taper region, rather than a highly inefficient taper design. Nonetheless, the taper design can still be improved to allow high efficiency with a shorter taper. A QCL with fewer active stages is also seen to couple light through the taper more efficiently and should be considered in future generations of QCLs on silicon.

Chapter 7

Applications

7.1 Power Scaling and Beam Combining

A significant advantage of heterogeneous integration is the ability to bond III-V material from multiple different epilayer growths onto a single photonic chip. For example, lasers can be constructed from QCL material optimized for drastically different wavelengths on one silicon chip. It is even possible, with some fabrication development, to bond and fabricate lasers on the same chip which were grown on different III-V substrates, such as GaSb-based ICLs and InP-based QCLs.

Light of different wavelengths generated on the chip can be used for either separate components (such as different gas sensor elements) or combined into the same waveguide. Wavelength beam combination can be achieved with multiple silicon photonic devices. For densely spaced spectral channels, arrayed waveguide gratings (AWGs) have been demonstrated with low loss spanning the visible (VIS) [132] to NIR [133], and moderate loss in the MIR [85], [51].

Figure 7.1 shows the concept schematic for a proposed multispectral source integrated on a single SONOI platform that combines the beams from bonded III-V lasers emitting

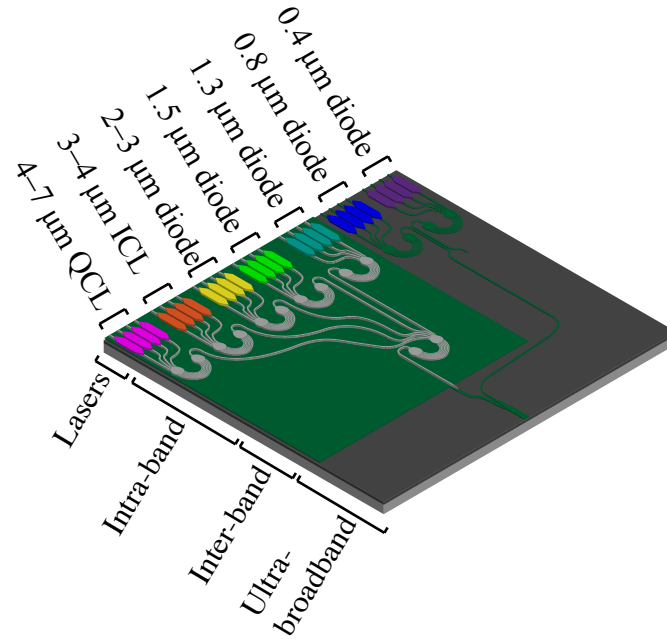


Figure 7.1: Multispectral laser architecture with multiple gain materials bonded onto a Si substrate. Each laser output is spectrally combined in multiple stages to a single output waveguide. ©2017 IEEE

at wavelengths ranging from $0.4 \mu\text{m}$ to $7 \mu\text{m}$. In a first (intra-band) combination stage, the light produced by arrays for each band is combined into a single output waveguide by an AWG. In the second (inter-band) combination stage, light from multiple spectral bands is combined with an AWG designed to have a much coarser wavelength spacing. On a SONOI waveguide platform, the light at shorter wavelengths is generated in Si_3N_4 waveguides while the light at longer wavelengths (including the MIR) is generated in Si waveguides. Then in the final combination stage, an ultra-broadband duplexer is used to combine all channels [134].

Two methods can be used to align each laser emission wavelength to the AWG spectral combiner channel. First, the lasers can be tuned to align with the combiner channel with a feedback that maximizes the output power. The AWG can also be tuned, although that approach may be more difficult and add more loss to the AWG transmission. The

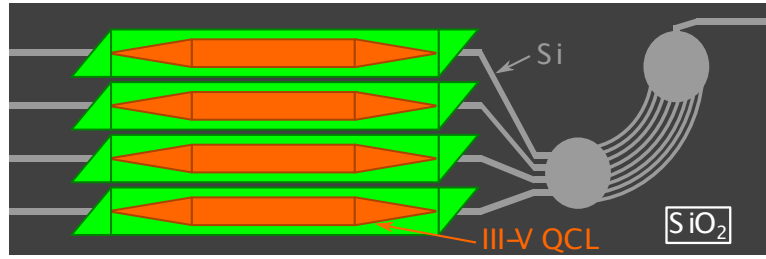


Figure 7.2: A schematic of DFB QCLs integrated with an AWG to combine the output emission into a single waveguide.

second option is to design the AWG within the laser cavity. This is typically avoided since it would compromise the performance of the lasers and result in lower output power and brightness. However, with ultra-low loss AWGs having ≤ 0.5 dB of loss per channel, this may nonetheless be advantageous when applied to a multispectral laser with many channels. Beam combination with AWGs is only advantageous for power scaling if the loss in the spectral combiners is reduced to less than about 3 dB per channel [135].

An integrated multi-spectral laser consisting of integrated QCLs and AWG wavelength beam combiners on Si was first shown by Stanton et al. [136, 137]. Figure 2.4 shows a schematic of the device, where four DFB QCLs output light into individual channels of an AWG, which outputs light through a waveguide terminated with a polished Si end-facet. These devices were fabricated on SOI with a $1.5 \mu\text{m}$ -thick Si waveguide layer above a $1.0 \mu\text{m}$ -thick SiO_2 layer. The TQE-thin (see table X) QCL epilayer design was chosen. $\lambda/4$ -shifted DFB gratings were etched 23 nm deep and had periods ranging from 734–756 nm to correspond with the AWG channels.

Three lasers were driven with 500 ns pulses with a 1 % duty cycle both individually and together. Figure 7.3(a) shows the light intensity and voltage vs. drive current per laser for single lasers and combinations of two or three lasers driven together. When driven together, a single current source was used to drive the lasers simultaneously and the reported current per laser is equal to the total current divided by the total peak drive

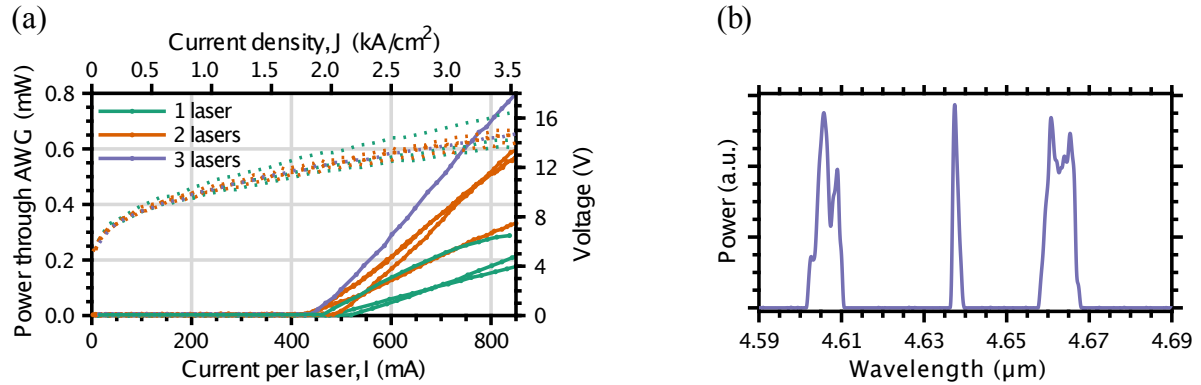


Figure 7.3: (a) Light emission and voltage vs. drive current per laser for combinations of 1, 2, or 3 multispectral QCLs-on-SOI being operated at the same time. (b) Optical spectrum of light collected from the AWG output waveguide while 3 QCLs are being driven simultaneously.

current, although because the variable resistance of the three lasers is likely not equal, the injected current may not have split equally between each laser. The output light was collected from the polished Si waveguide end facet at the output of the AWG. The total light collected from driving the lasers simultaneously at 850 mA per laser adds to 0.9 dB optical power greater than the sum of the power collected by driving each laser individually. The additional output power is possibly due to an unequal current injected in each laser when driven together, where a higher drive current is provided to lasers with a higher differential efficiency. Alternatively, the additional on-chip heating may shift the laser output wavelength (due to thermal refractive index tuning of the DFB grating) closer to the AWG channels, increasing the AWG efficiency for each channel.

Figure 7.3(b) shows the optical spectrum of the combined output of the three lasers while simultaneously driven, collected with a Bruker Vertex 70 FT-IR spectrometer. The three lasers operate at 4.60 μm , 4.64 μm , and 4.66 μm .

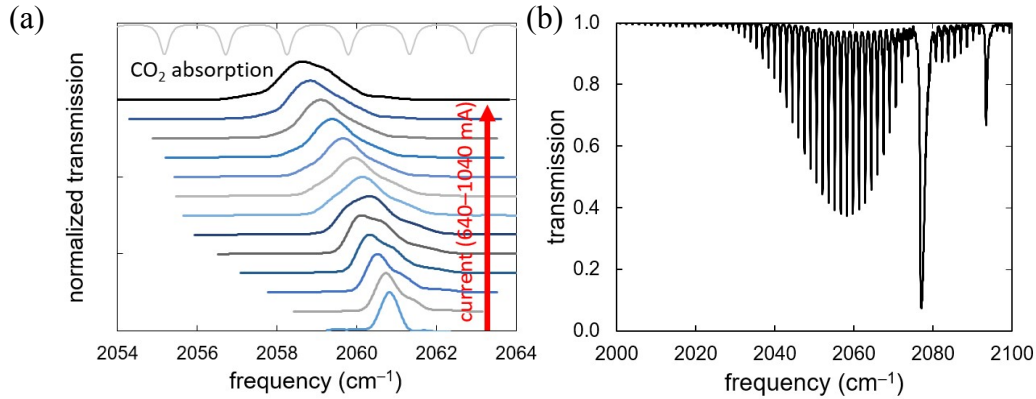


Figure 7.4: (a) FTIR spectrum vs. injection current, showing the tuning range of a QCL-on-SONOI and its transition from single-mode to multi-mode operation. (b) CO₂ absorption spectrum.

Summary

This result is the first photonic integrated circuit which uses heterogeneously integrated QCLs on a Si waveguiding system. An AWG was effectively used to combine the light emit from three QCLs operating at different wavelengths between 4.6 and 4.7 μm and scale the total output power on a single Si chip.

7.2 Gas Sensors

As a first step toward fully integrating a gas sensor on a Si chip, QCLs integrated on SONOI were used as a source in a tunable diode laser absorption spectroscopy (TDLAS) demonstration. Gas sensing measurements were performed at Physical Sciences Inc. (PSI) [138].

A 3 mm-long DFB QCL was chosen with a III-V mesa width of 4 μm , a Si waveguide width of 1.5 μm , and a $\lambda/4$ -shifted DFB grating period of 770 nm. This laser appeared to exhibit relatively single-wavelength characteristics, emitting near $\lambda=4.8 \mu\text{m}$.

In order to perform TDLAS, the laser must be tuned across a single absorption line.

The emission was first broadly tuned by adjusting the above-threshold injection current from 640–1040 mA. Figure 7.4(a) shows the optical spectrum of the laser, measured with an FTIR spectrometer, as the injection current is changed. The grey line indicates an absorption feature of CO₂.

This wavelength matches well with absorption features of CO₂. Figure 7.4(b) shows the absorption characteristics of CO₂ between 2000 cm⁻¹ and 2100 cm⁻¹ (4.76 μm and 5 μm). This simulation assumes a pressure of 1 atmosphere and path-length of 55 cm at room temperature. To measure a CO₂ absorption feature, the laser beam is collimated with a lens and passed through a 55 cm gas flow cell. We use a 1 Hz voltage triangle-wave, and the 1 MHz pulsed signal passes through a 10 kHz low-pass filter for detection by a liquid nitrogen cooled mercury cadmium telluride (MCT) photodiode. Ramping the voltage allowed the laser to be tuned across an absorption feature. The data was shifted using the FTIR spectrum and the wavelength sweep-rate was calibrated by observing fringes through a 25-mm thick Ge etalon in order to compare the measured spectrum with HITRAN data in Figure 7.4.

Figure 7.5 shows the normalized transmission through a CO₂ flow cell compared to scaled reference data from the HITRAN database. A transmission dip corresponding to the ~2061 cm⁻¹ feature in CO₂ was observed. The noise is greater near 2062 cm⁻¹, because the laser was operating near threshold to tune to that frequency. The smaller features observed near 2060 cm⁻¹ are consistent with the current at which the laser becomes multimode. The transmission minimum of 86% is higher than the value of 37% expected for the 55-cm path-length through CO₂. This may be due to linewidth broadening associated with chirp during the pulse.

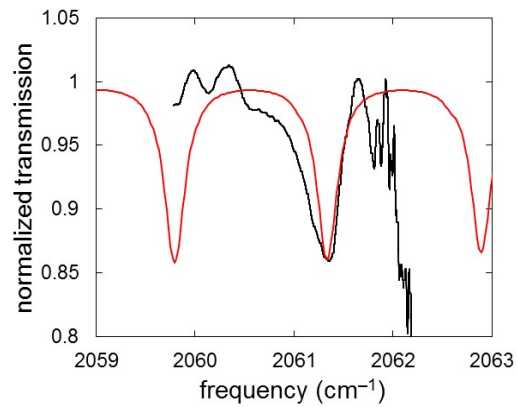


Figure 7.5: Normalized transmission through a CO₂ flow cell (black) compared to reference data (red) from the HITRAN database that has been scaled (reduced to 23%) to match the transmission minima of the data.

Summary

Here we showed tunable diode laser absorption spectroscopy (TDLAS) applied with a QCL integrated on Si as a first step toward demonstrating a fully-integrated gas sensor. The relatively single-wavelength laser emission was tuned by adjusting the drive voltage. The emission wavelength was scanned across a CO₂ absorption feature where a dip in the transmission corresponded well with the CO₂ absorption feature.

Chapter 8

Conclusions

8.1 Review

This dissertation outlines the successful integration of each of the three primary classes of mid-infrared light sources with silicon waveguides on silicon substrates: diode lasers, quantum cascade lasers, and interband cascade lasers. The III-V epitaxial material used for the diode lasers and the QCLs was grown on InP substrates, while that of the ICLs was grown on a GaSb substrate.

InP-based type-I diode lasers using InGaAs quantum wells for $\lambda \approx 2.0 \mu\text{m}$ operation were integrated on SOI. A Fabry-Perot laser emit more than 9.0 mW of CW power from a silicon waveguide at room temperature. Integrated SOAs with the same active material provide over 13-dB of peak gain at $\lambda = 2.01 \mu\text{m}$.

QCLs for $\lambda \approx 4.8 \mu\text{m}$ operation were integrated on SONOI. Fabry-Perot lasers emitted 31 mW from a polished silicon facet and operated in pulsed mode up to 60 °C. DFB lasers with threshold currents as low as 80 mA and threshold current densities below 1 kA/cm² emitted > 200 mW from a polished III-V/Si facet and operated in pulsed mode up to 100 °C.

Finally, ICLs for $\lambda \approx 3.6 \mu\text{m}$ operation were integrated on SOI. Fabry-Perot lasers emitted $\sim 0.5 \text{ mW}$ from a polished silicon facet and 6.6 mW from a polished III-V/Si facet in pulsed mode at room temperature. These lasers operated up to $50 \text{ }^\circ\text{C}$.

These results represent devices early in development. A number of improvements and optimizations can bring this technology closer to realistic integrated applications. The III-V epitaxial layer material designs are first-generation for all three lasers and should be optimized for future generations of devices. In particular, the number of quantum wells in the diode lasers and the number of active stages in the QCLs and ICLs were chosen based on the performance of lasers on native III-V substrates with waveguides formed entirely from III-V materials. It is unlikely that the same design rules apply best to the hybrid III-V/Si active region of heterogeneously integrated lasers, where the optical mode is shared between silicon and III-V layers.

The III-V tapers, which enable coupling of the optical mode from the hybrid III-V/Si active region to the passive waveguides, is currently a primary performance limitation particularly of the QCLs and ICLs. Simulations show that it should be possible to achieve high transmission and low reflectivity in an ideal case. The low taper transmission observed experimentally is likely attributed to material and scattering losses within the taper region. Modifications of the III-V epilayer designs will result in more efficient tapers for each laser type but with different considerations for the diode lasers, ICLs, and QCLs. The $\lambda \approx 2.0 \mu\text{m}$ diode lasers will benefit from a reduction in the thickness of the lower cladding and contact layers, which separate the active region and SCH layers from the silicon waveguides. The taper tip width, which was much too wide for this wavelength at $\sim 1.5 \mu\text{m}$, can be significantly reduced with a slightly modified fabrication process. A reduced number of stages in the QCLs will increase the coupling between the silicon waveguides and the high index active region, enabling a more efficient taper. The high index GaSb SCH layers surrounding the ICL active stages can be thinned or removed to

increase the modal confinement in the underlying silicon and improve the taper efficiency.

Measurements of the characteristic temperatures, T_0 , of the QCLs and ICLs are promising indications that the heterogeneous integration process is not fundamentally effecting the temperature dependence of the gain. Although SiO_2 cladding layers present in both SOI and SONOI impede the transfer of heat to the silicon substrate, silicon itself has a high thermal conductivity compared to the native III-V substrates. Alternative material systems such as GOS or SON, which are still suitable for mid-infrared operation, may improve the heat spreading of these lasers. QCLs, which generate a tremendous amount of heat during normal operation, may require more aggressive heat extraction technique, such as flip-chip bonding to a thermal submount. This should still be compatible with silicon photonic integration and when heat is extracted up through a submount, the thermal characteristics of the waveguiding platform can be ignored. ICLs, which generate much less heat than QCLs, will likely be able to achieve CW operation without a submount if the threshold current densities are decreased and the sidewall current leakage problems are mitigated.

Overall, these results show that heterogeneous integration techniques, where III-V materials are bonded above silicon waveguides, are not limited to the telecommunications bands or to type-I laser diodes and can be successfully applied to construct lasers on silicon from a range of III-V gain materials. While the performance of the lasers is not yet at the level of those fabricated on their native III-V substrates, the heterogeneous bonding and integration processes does not appear to introduce any fundamental limitations. These lasers can already be implemented in mid-infrared systems for applications which only need a few mW of pulsed light.

8.2 Prospects

At this time, all of the components necessary for a fully-integrated mid-infrared photonic system have been demonstrated. Resonators, multiplexers, modulators, phase shifters, frequency combs, detectors, and various other optical devices operating at wavelengths throughout the mid-infrared have already been demonstrated on silicon photonic waveguiding platforms. The lasers presented in this dissertation provide a basis for future integrated mid-infrared light sources on silicon.

However, very few PICs have been demonstrated for the mid-infrared, either monolithically on native III-V substrates, or on silicon photonic waveguiding platforms. Most research has been strongly focused on developing individual devices in the past, but often such research efforts have not had one specific application in mind. Going forward, individual applications should be addressed and developed. With sources and detectors available, complete complex systems can be constructed. Although optical characterization within the mid-infrared is significantly more challenging and limited compared to the near-infrared, many of the integrated optical device design techniques and tools developed for shorter wavelengths can easily be applied to the mid-infrared.

Bibliography

- [1] T. Komljenovic, S. Srinivasan, E. Norberg, M. L. Davenport, G. Fish, and J. E. Bowers, “Widely Tunable Narrow-Linewidth Monolithically Integrated External-Cavity Semiconductor Lasers,” *IEEE Journal of Selected Topics in Quantum Electronics* **21**, 1501909 (2015).
- [2] Y. Gu, Y. Zhang, Y. Cao, L. Zhou, X. Chen, H. Li, and S. Xi, “2.4 μm InP-based antimony-free triangular quantum well lasers in continuous-wave operation above room temperature,” *Applied Physics Express* **7**, 032701 (2014).
- [3] S. Sprengel, C. Grasse, P. Wiecha, A. Andrejew, T. Gruendl, G. Boehm, R. Meyer, and M.-C. Amann, “InP-Based Type-II Quantum-Well Lasers and LEDs,” *IEEE Journal of Selected Topics in Quantum Electronics* **19**, 1900909 (2013).
- [4] H. K. Choi, G. W. Turner, and S. J. Eglash, “High-Power GaInAsSb-AlGaAsSb Multiple-Quantum-Well Diode Lasers Emitting at 1.9 μm ,” *IEEE Photonics Technology Letters* **6**, 7–9 (1994).
- [5] K. Vizbaras and M. C. Amann, “3.6 μm GaSb-based type-I lasers with quinary barriers, operating at room temperature,” *Electronics Letters* **47**, 980–981 (2011).
- [6] K. Vizbaras and M.-C. Amann, “Room-temperature 3.73 μm GaSb-based type-I quantum-well lasers with quinary barriers,” *Semiconductor Science and Technology* **27**, 032001 (2012).
- [7] J. Scheuermann, M. von Edlinger, R. Weih, S. Becker, L. Nähle, M. Fischer, J. Koeth, M. Kamp, and S. Höfling, “Single-mode interband cascade laser sources for mid-infrared spectroscopic applications,” in “*SPIE Commercial + Scientific Sensing and Imaging*,” , M. A. Druy and R. A. Crocombe, eds. (SPIE, 2016), p. 98550G.
- [8] Y. Yao, A. J. Hoffman, and C. F. Gmachl, “Mid-infrared quantum cascade lasers,” *Nature Photonics* **6**, 432–439 (2012).
- [9] B. S. Williams, “Terahertz quantum-cascade lasers,” *Nature Photonics* **1**, 517–525 (2007).

- [10] S. D. Sifferman, H. P. Nair, R. Salas, N. T. Sheehan, S. J. Maddox, A. M. Crook, and S. R. Bank, “Highly Strained Mid-Infrared Type-I Diode Lasers on GaSb,” *IEEE Journal of Selected Topics in Quantum Electronics* **21**, 1502410 (2015).
- [11] D. Jung, S. Bank, M. L. Lee, and D. Wasserman, “Next-generation mid-infrared sources,” *Journal of Optics* **19**, 123001 (2017).
- [12] J. Faist, F. Capasso, D. L. Sivco, C. Sirtori, A. L. Hutchinson, and A. Y. Cho, “Quantum Cascade Laser,” *Science* **264**, 553–556 (1994).
- [13] Y. Bai, N. Bandyopadhyay, S. Tsao, S. Slivken, and M. Razeghi, “Room temperature quantum cascade lasers with 27% wall plug efficiency,” *Applied physics letters* **98**, 181102–4 (2011).
- [14] P. Figueiredo, M. Suttinger, R. Go, E. Tsvid, C. K. N. Patel, and A. Lyakh, “Progress in high-power continuous-wave quantum cascade lasers [Invited],” *Applied Optics* **56**, H15–H23 (2017).
- [15] I. Vurgaftman, R. Weih, M. Kamp, J. R. Meyer, C. L. Canedy, C. S. Kim, M. Kim, W. W. Bewley, C. D. Merritt, J. Abell, and S. Höfling, “Interband cascade lasers,” *Journal of Physics D: Applied Physics* **48**, 123001 (2015).
- [16] R. Q. Yang, “Infrared laser based on intersubband transitions in quantum wells,” *Superlattices and Microstructures* **17**, 77–83 (1995).
- [17] C.-H. Lin, R. Q. Yang, D. Zhang, S. J. Murry, S. S. Pei, A. A. Allerman, and S. R. Kurtz, “Type-II interband quantum cascade laser at $3.8\mu\text{m}$,” *Electronics Letters* **33**, 598–599 (1997).
- [18] M. Kim, C. L. Canedy, W. W. Bewley, C. S. Kim, J. R. Lindle, J. Abell, I. Vurgaftman, and J. R. Meyer, “Interband cascade laser emitting at $\lambda=3.75\ \mu\text{m}$ in continuous wave above room temperature,” *Applied physics letters* **92**, 191110 (2008).
- [19] J. R. Meyer, C. A. Hoffman, F. J. Bartoli, and L. R. Ram-Mohan, “Type-II quantum-well lasers for the mid-wavelength infrared,” *Applied physics letters* **67**, 757–759 (1995).
- [20] W. W. Bewley, C. L. Canedy, C. S. Kim, C. D. Merritt, M. V. Warren, I. Vurgaftman, J. R. Meyer, and M. Kim, “Room-temperature mid-infrared interband cascade vertical-cavity surface-emitting lasers,” *Applied physics letters* **109**, 151108 (2016).
- [21] I. Vurgaftman, W. W. Bewley, C. L. Canedy, C. S. Kim, M. Kim, C. D. Merritt, J. Abell, and J. R. Meyer, “Interband Cascade Lasers With Low Threshold Powers and High Output Powers,” *IEEE Journal of Selected Topics in Quantum Electronics* **19**, 1200210 (2013).

- [22] I. Vurgaftman, W. W. Bewley, C. L. Canedy, C. S. Kim, M. Kim, C. D. Merritt, J. Abell, J. R. Lindle, and J. R. Meyer, “Rebalancing of internally generated carriers for mid-infrared interband cascade lasers with very low power consumption,” *Nature Communications* **2**, 585–7 (2011).
- [23] R. A. Soref, S. J. Emelett, and W. R. Buchwald, “Silicon waveguided components for the long-wave infrared region,” *Journal of Optics A: Pure and Applied Optics* **8**, 840–848 (2006).
- [24] B. J. Eggleton, B. Luther-Davies, and K. Richardson, “Chalcogenide photonics,” *Nature Photonics* **5**, 141–148 (2011).
- [25] H. Lin, L. Li, Y. Zou, S. Danto, J. D. Musgraves, K. Richardson, S. Kozacik, M. Murakowski, D. Prather, P. T. Lin, V. Singh, A. Agarwal, L. C. Kimerling, and J. Hu, “Demonstration of high-Q mid-infrared chalcogenide glass-on-silicon resonators,” *Optics Letters* **38**, 1470–1472 (2013).
- [26] N. Hô, M. C. Phillips, H. Qiao, P. J. Allen, K. Krishnaswami, B. J. Riley, T. L. Myers, and N. C. Anheier, “Single-mode low-loss chalcogenide glass waveguides for the mid-infrared,” *Optics Letters* **31**, 1860–1862 (2006).
- [27] J. Kischkat, S. Peters, B. Gruska, M. Semtsiv, M. Chashnikova, M. Klinkmüller, O. Fedosenko, S. Machulik, A. Aleksandrova, G. Monastyrskiy, Y. Flores, and W. T. Masselink, “Mid-infrared optical properties of thin films of aluminum oxide, titanium dioxide, silicon dioxide, aluminum nitride, and silicon nitride,” *Applied Optics* **51**, 6789–6798 (2012).
- [28] D. T. Spencer, J. F. Bauters, M. J. R. Heck, and J. E. Bowers, “Integrated waveguide coupled Si₃N₄ resonators in the ultrahigh-Q regime,” *Optica* **1**, 153–157 (2014).
- [29] M.-C. Tien, J. F. Bauters, M. J. R. Heck, D. T. Spencer, D. J. Blumenthal, and J. E. Bowers, “Ultra-high quality factor planar Si₃N₄ ring resonators on Si substrates,” *Optics Express* **19**, 13551–13556 (2011).
- [30] J. F. Bauters, M. J. R. Heck, D. D. John, J. S. Barton, C. M. Bruinink, A. Leinse, R. G. Heideman, D. J. Blumenthal, and J. E. Bowers, “Planar waveguides with less than 0.1 dB/m propagation loss fabricated with wafer bonding,” *Optics Express* **19**, 24090–24101 (2011).
- [31] J. F. Bauters, M. L. Davenport, M. J. R. Heck, J. K. Doylend, A. Chen, A. W.-L. Fang, and J. E. Bowers, “Silicon on ultra-low-loss waveguide photonic integration platform,” *Optics Express* **21**, 544–555 (2013).

- [32] S. A. Miller, M. Yu, X. Ji, A. G. Griffith, J. Cardenas, A. L. Gaeta, and M. Lipson, “Low-loss silicon platform for broadband mid-infrared photonics,” *Optica* **4**, 707–712 (2017).
- [33] G. Z. Mashanovich, M. M. Milosevic, M. Nedeljkovic, N. Owens, B. Xiong, E. J. Teo, and Y. Hu, “Low loss silicon waveguides for the mid-infrared,” *Optics Express* **19**, 7112 (2011).
- [34] R. Shankar, I. Bulu, and M. Loncar, “Integrated high-quality factor silicon-on-sapphire ring resonators for the mid-infrared,” *Applied physics letters* **102**, 051108 (2013).
- [35] M. Brun, P. Labeye, G. Grand, J.-M. Hartmann, F. Boulila, M. Carras, and S. Nicoletti, “Low loss SiGe graded index waveguides for mid-IR applications,” *Optics Express* **22**, 508–518 (2014).
- [36] M. Nedeljkovic, J. S. Penades, V. Mittal, G. S. Murugan, A. Z. Khokhar, C. Littlejohns, L. G. Carpenter, C. B. E. Gawith, J. S. Wilkinson, and G. Z. Mashanovich, “Germanium-on-silicon waveguides operating at mid-infrared wavelengths up to 8.5 μm ,” *Optics Express* **25**, 27431 (2017).
- [37] S. Khan, J. Chiles, J. Ma, and S. Fathpour, “Silicon-on-nitride waveguides for mid- and near-infrared integrated photonics,” *Applied physics letters* **102**, 121104 (2013).
- [38] P. Tai Lin, V. Singh, L. Kimerling, and A. Murthy Agarwal, “Planar silicon nitride mid-infrared devices,” *Applied physics letters* **102**, 251121 (2013).
- [39] P. T. Lin, V. Singh, Y. Cai, L. C. Kimerling, and A. Agarwal, “Air-clad silicon pedestal structures for broadband mid-infrared microphotonics,” *Optics Letters* **38**, 1031–1033 (2013).
- [40] W. Li, P. Anantha, S. Bao, K. H. Lee, X. Guo, T. Hu, L. Zhang, H. Wang, R. Soref, and C. S. Tan, “Germanium-on-silicon nitride waveguides for mid-infrared integrated photonics,” *Applied physics letters* **109**, 241101 (2016).
- [41] T. Baehr-Jones, A. Spott, R. Ilic, A. Spott, B. Penkov, W. Asher, and M. Hochberg, “Silicon-on-sapphire integrated waveguides for the mid-infrared,” *Optics Express* **18**, 12127–12135 (2010).
- [42] A. Spott, Y. Liu, T. Baehr-Jones, R. Ilic, and M. Hochberg, “Silicon waveguides and ring resonators at 5.5 μm ,” *Applied Physics Letters* **97**, 213501 (2010).
- [43] N. Singh, D. D. Hudson, and B. J. Eggleton, “Silicon-on-sapphire pillar waveguides for Mid-IR supercontinuum generation,” *Optics Express* **23**, 17345 (2015).

- [44] Y. Zou, S. Chakravarty, and R. T. Chen, “Mid-infrared silicon-on-sapphire waveguide coupled photonic crystal microcavities,” *Applied physics letters* **107**, 081109 (2015).
- [45] Z. Cheng, X. Chen, C. Y. Wong, K. Xu, C. K. Y. Fung, Y. M. Chen, and H. K. Tsang, “Mid-Infrared Grating Couplers for Silicon-on-Sapphire Waveguides,” *Photonics Journal, IEEE* **4**, 104–113 (2011).
- [46] Y. Zou, H. Subbaraman, S. Chakravarty, X. Xu, A. Hosseini, W.-C. Lai, P. Wray, and R. T. Chen, “Grating-coupled silicon-on-sapphire integrated slot waveguides operating at mid-infrared wavelengths,” *Optics Letters* **39**, 3070–3073 (2014).
- [47] F. Li, S. D. Jackson, C. Grillet, E. Magi, D. Hudson, S. J. Madden, Y. Moghe, C. O’Brien, A. Read, S. G. Duvall, P. Atanackovic, B. J. Eggleton, and D. J. Moss, “Low propagation loss silicon-on-sapphire waveguides for the mid-infrared,” *Optics Express* **19**, 15212–15220 (2011).
- [48] <http://www.iqep.com/>.
- [49] Y.-C. Chang, V. Paeder, L. Hvozdar, J.-M. Hartmann, and H. P. Herzig, “Low-loss germanium strip waveguides on silicon for the mid-infrared,” *Optics Letters* **37**, 2883–2885 (2012).
- [50] A. Malik, S. Dwivedi, L. Van Landschoot, M. Muneeb, Y. Shimura, G. Lepage, J. Van Campenhout, W. Vanherle, T. Van Opstal, R. Loo, and G. Roelkens, “Ge-on-Si and Ge-on-SOI thermo-optic phase shifters for the mid-infrared,” *Optics Express* **22**, 28479 (2014).
- [51] A. Malik, M. Muneeb, S. Pathak, Y. Shimura, J. Van Campenhout, R. Loo, and G. Roelkens, “Germanium-on-Silicon Mid-Infrared Arrayed Waveguide Grating Multiplexers,” *Photonics Technology Letters, IEEE* **25**, 1805–1808 (2013).
- [52] M. Nedeljkovic, J. S. Penades, C. J. Mitchell, A. Z. Khokhar, S. Stankovic, T. D. Bucio, C. G. Littlejohns, F. Y. Gardes, and G. Z. Mashanovich, “Surface-Grating-Coupled Low-Loss Ge-on-Si Rib Waveguides and Multimode Interferometers,” *IEEE Photonics Technology Letters* **27**, 1040–1043 (2015).
- [53] L. Shen, N. Healy, C. J. Mitchell, J. S. Penades, M. Nedeljkovic, G. Z. Mashanovich, and A. C. Peacock, “Mid-infrared all-optical modulation in low-loss germanium-on-silicon waveguides,” *Optics Letters* **40**, 268–271 (2015).
- [54] B. Troia, J. S. Penades, A. Z. Khokhar, M. Nedeljkovic, C. Alonso-Ramos, V. M. N. Passaro, and G. Z. Mashanovich, “Germanium-on-silicon Vernier-effect photonic microcavities for the mid-infrared,” *Optics Letters* **41**, 610–613 (2016).

- [55] A. Malik, M. Muneeb, Y. Shimura, J. Van Campenhout, R. Loo, and G. Roelkens, “Germanium-on-silicon planar concave grating wavelength (de)multiplexers in the mid-infrared,” *Applied physics letters* **103**, 161119 (2013).
- [56] J. M. Ramirez, V. Vakarin, C. Gilles, J. Frigerio, A. Ballabio, P. Chaisakul, X. L. Roux, C. Alonso-Ramos, G. Maisons, L. Vivien, M. Carras, G. Isella, and D. Marris-Morini, “Low-loss Ge-rich $\text{Si}_{0.2}\text{Ge}_{0.8}$ waveguides for mid-infrared photonics,” *Optics Letters* **42**, 105–108 (2016).
- [57] J. M. Ramirez, V. Vakarin, J. Frigerio, P. Chaisakul, D. Chrastina, X. Le Roux, A. Ballabio, L. Vivien, G. Isella, and D. Marris-Morini, “Ge-rich graded-index $\text{Si}_{1-x}\text{Ge}_x$ waveguides with broadband tight mode confinement and flat anomalous dispersion for nonlinear mid-infrared photonics,” *Optics Express* **25**, 6561–6567 (2017).
- [58] A. W.-L. Fang, H. Park, O. Cohen, R. Jones, M. J. Paniccia, and J. E. Bowers, “Electrically pumped hybrid AlGaInAs-silicon evanescent laser,” *Optics Express* **14**, 9203–9210 (2006).
- [59] H.-H. Chang, A. W.-L. Fang, M. N. Sysak, H. Park, R. Jones, O. Cohen, O. Raday, M. J. Paniccia, and J. E. Bowers, “1310nm silicon evanescent laser,” *Optics Express* **15**, 11466–11471 (2007).
- [60] C. Zhang, S. Srinivasan, Y. Tang, M. J. R. Heck, M. L. Davenport, and J. E. Bowers, “Low threshold and high speed short cavity distributed feedback hybrid silicon lasers,” *Optics Express* **22**, 10202–10209 (2014).
- [61] S. Srinivasan, A. Arrighi, M. J. R. Heck, J. Hutchinson, E. Norberg, G. Fish, and J. E. Bowers, “Harmonically Mode-Locked Hybrid Silicon Laser With Intra-Cavity Filter to Suppress Supermode Noise,” *IEEE Journal of Selected Topics in Quantum Electronics* **20**, 1100208 (2013).
- [62] M. L. Davenport, S. Liu, and J. E. Bowers, “Integrated heterogeneous silicon/III–V mode-locked lasers,” *Photonics Research* **6**, 468–478 (2018).
- [63] J. C. Hulme, J. K. Doylend, M. J. R. Heck, J. D. Peters, M. L. Davenport, J. T. Bovington, L. A. Coldren, and J. E. Bowers, “Fully integrated hybrid silicon two dimensional beam scanner,” *Optics Express* **23**, 5861–5874 (2015).
- [64] T. Komljenovic, M. L. Davenport, J. Hulme, A. Y. Liu, C. T. Santis, A. Spott, S. Srinivasan, E. J. Stanton, C. Zhang, and J. E. Bowers, “Heterogeneous Silicon Photonic Integrated Circuits,” *Journal of Lightwave Technology* **34**, 20–35 (2015).
- [65] M. L. Davenport, S. Skendzic, N. Volet, J. C. Hulme, M. J. R. Heck, and J. E. Bowers, “Heterogeneous Silicon/III–V Semiconductor Optical Amplifiers,” *IEEE Journal of Selected Topics in Quantum Electronics* **22**, 3100111 (2016).

- [66] C. Zhang, S. Zhang, J. D. Peters, and J. E. Bowers, “ $8 \times 8 \times 40$ Gbps fully integrated silicon photonic network on chip,” *Optica* **3**, 785–786 (2016).
- [67] H.-H. Chang, Y.-h. Kuo, R. Jones, A. Barkai, and J. E. Bowers, “Integrated hybrid silicon triplexer,” *Optics Express* **18**, 23891–23899 (2010).
- [68] A. De Groote, J. D. Peters, M. L. Davenport, M. J. R. Heck, R. Baets, G. Roelkens, and J. E. Bowers, “Heterogeneously integrated III–V-on-silicon multibandgap superluminescent light-emitting diode with 290nm optical bandwidth,” *Optics Letters* **39**, 4784–4787 (2014).
- [69] J. T. Bovington, M. J. R. Heck, and J. E. Bowers, “Heterogeneous lasers and coupling to Si_3N_4 near 1060nm,” *Optics Letters* **39**, 6017–6020 (2014).
- [70] G. Roelkens, U. Dave, A. Gassenq, N. Hattasan, C. Hu, B. Kuyken, F. Leo, A. Malik, M. Muneeb, E. Ryckeboer, D. Sanchez, S. Uvin, R. Wang, Z. Hens, R. Baets, Y. Shimura, F. Gencarelli, B. Vincent, R. Loo, J. Van Campenhout, L. Cerutti, J.-B. Rodriguez, E. Tournié, X. Chen, M. Nedeljkovic, G. Mashanovich, L. Shen, N. Healy, A. C. Peacock, X. Liu, R. Osgood, and W. M. J. Green, “Silicon-Based Photonic Integration Beyond the Telecommunication Wavelength Range,” *IEEE Journal of Selected Topics in Quantum Electronics* **20**, 8201511 (2014).
- [71] A. Spott, E. J. Stanton, N. Volet, J. D. Peters, J. R. Meyer, and J. E. Bowers, “Heterogeneous Integration for Mid-infrared Silicon Photonics,” *IEEE Journal of Selected Topics in Quantum Electronics* **23**, 1–10 (2017).
- [72] A. Spott, M. L. Davenport, J. Peters, J. Bovington, M. J. R. Heck, E. J. Stanton, I. Vurgaftman, J. R. Meyer, and J. Bowers, “Heterogeneously integrated $2.0 \mu\text{m}$ CW hybrid silicon lasers at room temperature,” *Optics Letters* **40**, 1480–1483 (2015).
- [73] N. Volet, A. Spott, E. J. Stanton, M. L. Davenport, L. Chang, J. D. Peters, T. C. Briles, I. Vurgaftman, J. R. Meyer, and J. E. Bowers, “Semiconductor optical amplifiers at $2.0\text{-}\mu\text{m}$ wavelength on silicon,” *Laser & Photonics Reviews* **11**, 1600165 (2017).
- [74] R. Wang, S. Sprengel, G. Boehm, M. Muneeb, R. Baets, M.-C. Amann, and G. Roelkens, “ $2.3 \mu\text{m}$ range InP-based type-II quantum well Fabry-Perot lasers heterogeneously integrated on a silicon photonic integrated circuit,” *Optics Express* **24**, 21081–21089 (2016).
- [75] R. Wang, S. Sprengel, A. Malik, A. Vasiliev, G. Boehm, R. Baets, M.-C. Amann, and G. Roelkens, “Heterogeneously integrated III–V-on-silicon $2.3\text{x} \mu\text{m}$ distributed feedback lasers based on a type-II active region,” *Applied physics letters* **109**, 221111 (2016).

- [76] R. Wang, S. Sprengel, G. Boehm, R. Baets, M.-C. Amann, and G. Roelkens, “Broad wavelength coverage $2.3\mu\text{m}$ III-V-on-silicon DFB laser array,” *Optica* **4**, 972–975 (2017).
- [77] A. Spott, J. Peters, M. L. Davenport, E. J. Stanton, C. D. Merritt, W. W. Bewley, I. Vurgaftman, C. S. Kim, J. R. Meyer, J. Kirch, L. J. Mawst, D. Botez, and J. E. Bowers, “Quantum cascade laser on silicon,” *Optica* **3**, 545–551 (2016).
- [78] A. Spott, J. Peters, M. L. Davenport, E. J. Stanton, C. Zhang, C. Merritt, W. Bewley, I. Vurgaftman, C. S. Kim, J. R. Meyer, J. Kirch, L. Mawst, D. Botez, and J. Bowers, “Heterogeneously Integrated Distributed Feedback Quantum Cascade Lasers on Silicon,” *Photonics* **3**, 35 (2016).
- [79] A. Spott, E. J. Stanton, A. Torres, M. Davenport, C. L. Canedy, I. Vurgaftman, M. Kim, C. S. Kim, C. D. Merritt, W. W. Bewley, J. R. Meyer, and J. E. Bowers, “Interband Cascade Lasers on Silicon,” *Optica In Review* (2018).
- [80] S. Jung, J. Kirch, J. H. Kim, L. J. Mawst, D. Botez, and M. A. Belkin, “Quantum cascade lasers transfer-printed on silicon-on-sapphire,” *Applied physics letters* **111**, 211102 (2017).
- [81] A. De Groote, P. Cardile, A. Z. Subramanian, A. M. Fecioru, C. Bower, D. Delbeke, R. Baets, and G. Roelkens, “Transfer-printing-based integration of single-mode waveguide-coupled III-V-on-silicon broadband light emitters,” *Optics Express* **24**, 13754–13762 (2016).
- [82] N. Hattasan, A. Gassenq, L. Cerutti, J.-B. Rodriguez, E. Tournié, and G. Roelkens, “Heterogeneous Integration of GaInAsSb p-i-n Photodiodes on a Silicon-on-Insulator Waveguide Circuit,” *IEEE Photonics Technology Letters* **23**, 1760–1762 (2011).
- [83] R. Wang, S. Sprengel, M. Muneeb, G. Boehm, R. Baets, M.-C. Amann, and G. Roelkens, “ $2\mu\text{m}$ wavelength range InP-based type-II quantum well photodiodes heterogeneously integrated on silicon photonic integrated circuits,” *Optics Express* **23**, 26834–26841 (2015).
- [84] R. Wang, M. Muneeb, S. Sprengel, G. Boehm, A. Malik, R. Baets, M.-C. Amann, and G. Roelkens, “III-V-on-silicon $2\text{-}\mu\text{m}$ -wavelength-range wavelength demultiplexers with heterogeneously integrated InP-based type-II photodetectors,” *Optics Express* **24**, 8480–8490 (2016).
- [85] M. Muneeb, X. Chen, P. Verheyen, G. Lepage, S. Pathak, E. Ryckeboer, A. Malik, B. Kuyken, M. Nedeljkovic, J. Van Campenhout, G. Z. Mashanovich, and G. Roelkens, “Demonstration of Silicon-on-insulator mid-infrared spectrometers operating at $3.8\mu\text{m}$,” *Optics Express* **21**, 11659–11669 (2013).

- [86] M. Muneeb, A. Ruocco, A. Malik, S. Pathak, E. Ryckeboer, D. Sanchez, L. Cerutti, J. B. Rodriguez, E. Tournié, W. Bogaerts, M. K. Smit, and G. Roelkens, “Silicon-on-insulator shortwave infrared wavelength meter with integrated photodiodes for on-chip laser monitoring,” *Optics Express* **22**, 27300 (2014).
- [87] M. Muneeb, A. Vasiliev, A. Ruocco, A. Malik, H. Chen, M. Nedeljkovic, J. S. Penades, L. Cerutti, J. B. Rodriguez, G. Z. Mashanovich, M. K. Smit, E. Tourni, and G. Roelkens, “III-V-on-silicon integrated micro - spectrometer for the 3 μm wavelength range,” *Optics Express* **24**, 9465–9472 (2016).
- [88] J. Wang, J. Hu, P. Becla, A. M. Agarwal, and L. C. Kimerling, “Resonant-cavity-enhanced mid-infrared photodetector on a silicon platform,” *Optics Express* **18**, 12890 (2010).
- [89] J. Wang, T. Zens, J. Hu, P. Becla, L. C. Kimerling, and A. M. Agarwal, “Monolithically integrated, resonant-cavity-enhanced dual-band mid-infrared photodetector on silicon,” *Applied physics letters* **100**, 211106 (2012).
- [90] A. Gassenq, F. Gencarelli, J. Van Campenhout, Y. Shimura, R. Loo, G. Narcy, B. Vincent, and G. Roelkens, “GeSn/Ge heterostructure short-wave infrared photodetectors on silicon,” *Optics Express* **20**, 27297–27303 (2012).
- [91] H. Cong, C. Xue, J. Zheng, F. Yang, K. Yu, Z. Liu, X. Zhang, B. Cheng, and Q. Wang, “Silicon Based GeSn p-i-n Photodetector for SWIR Detection,” *Photonics Journal, IEEE* **8**, 1–6 (2016).
- [92] X. Wang, Z. Cheng, K. Xu, H. K. Tsang, and J.-B. Xu, “High-responsivity graphene/silicon-heterostructure waveguide photodetectors,” **7**, 888–891 (2013).
- [93] B. W. Jia, K. H. Tan, W. K. Loke, S. Wicaksono, K. H. Lee, and S. F. Yoon, “Monolithic Integration of InSb Photodetector on Silicon for Mid-Infrared Silicon Photonics,” *ACS Photonics* **5**, 1512–1520 (2018).
- [94] J. Wu, Q. Jiang, S. Chen, M. Tang, Y. I. Mazur, Y. Maidaniuk, M. Benamara, M. P. Semtsiv, W. T. Masselink, K. A. Sablon, G. J. Salamo, and H. Liu, “Monolithically Integrated InAs/GaAs Quantum Dot Mid-Infrared Photodetectors on Silicon Substrates,” *ACS Photonics* **3**, 749–753 (2016).
- [95] H. Nguyen-Van, A. N. Baranov, Z. Loghmari, L. Cerutti, J.-B. Rodriguez, J. Tournet, G. Narcy, G. Boissier, G. Patriarche, M. Bahriz, E. Tournié, and R. Teissier, “Quantum cascade lasers grown on silicon,” *Scientific Reports* **8**, 7206 (2018).
- [96] F. Kish, V. Lal, P. Evans, S. W. Corzine, M. Ziari, T. Butrie, M. Reffle, H.-S. Tsai, A. Dentai, J. Pleumeekers, M. Missey, M. Fisher, S. Murthy, R. Salvatore, P. Samra, S. Demars, N. Kim, A. James, A. Hosseini, P. Studenkov, M. Lauer-mann, R. Going, M. Lu, J. Zhang, J. Tang, J. Bostak, T. Vallaitis, M. Kuntz,

- D. Pavinski, A. Karanicolas, B. Behnia, D. Engel, O. Khayam, N. Modi, M. R. Chitgarha, P. Mertz, W. Ko, R. Maher, J. Osenbach, J. T. Rahn, H. Sun, K.-T. Wu, M. Mitchell, and D. Welch, “System-on-Chip Photonic Integrated Circuits,” *IEEE Journal of Selected Topics in Quantum Electronics* **24**, 6100120 (2018).
- [97] S. Latkowski, A. Hansel, N. Bhattacharya, T. de Vries, L. Augustin, K. Williams, M. Smit, and E. Bente, “Novel Widely Tunable Monolithically Integrated Laser Source,” *Photonics Journal, IEEE* **7**, 1–9 (2015).
- [98] S. Latkowski, A. Hänsel, P. J. van Veldhoven, D. D’Agostino, H. Rabbani-Haghighi, B. Docter, N. Bhattacharya, P. J. A. Thijs, H. P. M. M. Ambrosius, M. K. Smit, K. A. Williams, and E. A. J. M. Bente, “Monolithically integrated widely tunable laser source operating at $2\mu\text{m}$,” *Optica* **3**, 1412–1417 (2016).
- [99] C. Gilles, G. Maisons, B. Simozrag, and M. Carras, “Monolithic coupling of QCLs in evanescent waveguides on InP,” in “Quantum Sensing and Nanophotonic Devices XII,” , M. Razeghi, E. Tournié, and G. J. Brown, eds. (2015).
- [100] C. Gilles, L. J. Orbe, G. Carpintero, J. Abautret, G. Maisons, and M. Carras, “Monolithic integration of a quantum cascade laser array and an echelle grating multiplexer for widely tunable mid-infrared sources,” in “SPIE OPTO,” , A. A. Belyanin and P. M. Smowton, eds. (SPIE, 2016), pp. 97671R–7.
- [101] C. Gilles, L. J. Orbe, G. Carpintero, G. Maisons, and M. Carras, “Mid-infrared wavelength multiplexer in InGaAs/InP waveguides using a Rowland circle grating,” *Optics Express* **23**, 20288–20296 (2015).
- [102] J. Montoya, C. Wang, A. Goyal, K. Creedon, M. Connors, J. Daulton, J. Donnelly, L. Missaggia, C. Aleshire, A. Sanchez-Rubio, and W. Herzog, “Integration of quantum cascade lasers and passive waveguides,” *Applied physics letters* **107**, 031110 (2015).
- [103] B. Schwarz, P. Reininger, H. Detz, T. Zederbauer, A. Andrews, W. Schrenk, and G. Strasser, “Monolithically Integrated Mid-Infrared Quantum Cascade Laser and Detector,” *Sensors* **13**, 2196–2205 (2013).
- [104] D. Liang, J. E. Bowers, D. C. Oakley, A. Napoleone, D. C. Chapman, C. L. Chen, P. W. Juodawlkis, and O. Rada, “High-Quality 150mm InP-to-Silicon Epitaxial Transfer for Silicon Photonic Integrated Circuits,” *Electrochemical and Solid-State Letters* **12**, H101–H104 (2009).
- [105] <http://www.nlight.net/>.
- [106] D. Liang, A. W.-L. Fang, H. Park, T. E. Reynolds, K. Warner, D. C. Oakley, and J. E. Bowers, “Low-Temperature, Strong SiO₂-SiO₂ Covalent Wafer Bonding for

- III–V Compound Semiconductors-to-Silicon Photonic Integrated Circuits,” *Journal of Electronic Materials* **37**, 1552–1559 (2008).
- [107] D. Liang and J. E. Bowers, “Highly efficient vertical outgassing channels for low-temperature InP-to-silicon direct wafer bonding on the silicon-on-insulator substrate,” *Journal of Vacuum Science & Technology B: Microelectronics and Nanometer Structures* **26**, 1560–1568 (2008).
- [108] M. Asada and Y. Suematsu, “Density-matrix theory of semiconductor lasers with relaxation broadening model-gain and gain-suppression in semiconductor lasers,” *IEEE Journal of Quantum Electronics* **21**, 434–442 (1985).
- [109] A. Evans, S. R. Darvish, S. Slivken, J. Nguyen, Y. Bai, and M. Razeghi, “Buried heterostructure quantum cascade lasers with high continuous-wave wall plug efficiency,” *Applied physics letters* **91**, 071101 (2007).
- [110] K. A. Black, P. Abraham, A. Karim, J. E. Bowers, and E. L. Hu, “Improved luminescence from InGaAsP/InP MQW active regions using a wafer fused superlattice barrier,” in “Conference Proceedings. Eleventh International Conference on Indium Phosphide and Related Materials (IPRM’99) (Cat. No.99CH36362),” (IEEE, 1999), pp. 357–360.
- [111] O. K. Kim and W. A. Bonner, “Infrared reflectance and absorption of N-type InP,” *Journal of Electronic Materials* **12**, 827–836 (1983).
- [112] E. D. Palik, *Handbook of Optical Constants of Solids* (Academic, 1998).
- [113] D. Botez, C.-C. Chang, and L. J. Mawst, “Temperature sensitivity of the electro-optical characteristics for mid-infrared ($\lambda=3\text{--}16\ \mu\text{m}$)-emitting quantum cascade lasers,” *Journal of Physics D: Applied Physics* **49**, 043001 (2015).
- [114] M. N. Sysak, D. Liang, R. Jones, G. Kurczveil, M. Piels, M. Fiorentino, R. G. Beausoleil, and J. E. Bowers, “Hybrid Silicon Laser Technology: A Thermal Perspective,” *IEEE Journal of Selected Topics in Quantum Electronics* **17**, 1490–1498 (2011).
- [115] P. Werle, F. Slemr, K. Maurer, R. Kormann, R. Mücke, and B. Jänker, “Near- and mid-infrared laser-optical sensors for gas analysis,” *Optics and Lasers in Engineering* **37**, 101–114 (2002).
- [116] C. Bauer, A. K. Sharma, U. Willer, J. Burgmeier, B. Braunschweig, W. Schade, S. Blaser, L. Hvozدارa, A. Müller, and G. Holl, “Potentials and limits of mid-infrared laser spectroscopy for the detection of explosives,” *Applied Physics B* **92**, 327–333 (2008).

- [117] R. M. Briggs, C. Frez, C. E. Borgentun, and S. Forouhar, “Regrowth-free single-mode quantum cascade lasers with power consumption below 1W,” *Applied physics letters* **105**, 141117 (2014).
- [118] Q. Y. Lu, Y. Bai, N. Bandyopadhyay, S. Slivken, and M. Razeghi, “2.4 W room temperature continuous wave operation of distributed feedback quantum cascade lasers,” *Applied physics letters* **98**, 181106 (2011).
- [119] A. Wittmann, Y. Bonetti, M. Fischer, J. Faist, S. Blaser, and E. Gini, “Distributed-Feedback Quantum-Cascade Lasers at 9 μm Operating in Continuous Wave Up to 423 K,” *IEEE Photonics Technology Letters* **21**, 814–816 (2009).
- [120] L. Coldren, S. Corzine, and M. Masanovic, *Diode Lasers and Photonic Integrated Circuits* (2012).
- [121] C. J. Glassbrenner and G. A. Slack, “Thermal Conductivity of Silicon and Germanium from 3°K to the Melting Point,” *Physical Review* **134**, A1058–A1069 (1964).
- [122] J. Liu, F. Liu, L. Li, L. Wang, and Z. Wang, “A mini-staged multi-stacked quantum cascade laser for improved optical and thermal performance,” *Semiconductor Science and Technology* **24**, 075023 (2009).
- [123] A. Salhi, P. C. Chi, A. Alharbi, G. S. Petrich, A. Al-Muhanna, and L. A. Kolodziejwski, “Temperature Dependence of Optical Gain and Loss in 2- μm InP Lasers,” *IEEE Photonics Technology Letters* **23**, 1523–1525 (2011).
- [124] J. R. Meyer, I. Vurgaftman, R. Q. Yang, and L. R. Ram-Mohan, “Type-II and type-I interband cascade lasers,” *Electronics Letters* **32**, 45–46 (1996).
- [125] T. Hu, B. Dong, X. Luo, T.-Y. Liow, J. Song, C. Lee, and G.-Q. Lo, “Silicon photonic platforms for mid-infrared applications [Invited],” *Photonics Research* **5**, 417–14 (2017).
- [126] M. M. Milosevic, M. Nedeljkovic, T. M. Ben Masaud, E. Jaberansary, H. M. H. Chong, N. G. Emerson, G. T. Reed, and G. Z. Mashanovich, “Silicon waveguides and devices for the mid-infrared,” *Applied physics letters* **101**, 121105 (2012).
- [127] C. L. Canedy, J. Abell, C. D. Merritt, W. W. Bewley, C. S. Kim, M. Kim, I. Vurgaftman, and J. R. Meyer, “Pulsed and CW performance of 7-stage interband cascade lasers,” *Optics Express* **22**, 7702–7710 (2014).
- [128] D. Liang, D. C. Chapman, Y. Li, D. C. Oakley, T. Napoleone, P. W. Juodawlkis, C. Brubaker, C. Mann, H. Bar, O. Raday, and J. E. Bowers, “Uniformity study of wafer-scale InP-to-silicon hybrid integration,” *Applied Physics A* **103**, 213–218 (2010).

- [129] M. Kim, C. S. Kim, W. W. Bewley, C. D. Merritt, C. L. Canedy, J. Abell, I. Vurgaftman, and J. R. Meyer, “Interband cascade lasers with high CW power and brightness,” in “SPIE OPTO,” , M. Razeghi, E. Tournié, and G. J. Brown, eds. (SPIE, 2015), p. 937029.
- [130] J. A. Nolde, E. M. Jackson, M. F. Bennett, C. A. Affouda, E. R. Cleveland, C. L. Canedy, I. Vurgaftman, G. G. Jernigan, J. R. Meyer, and E. H. Aifer, “Reticulated shallow etch mesa isolation for controlling surface leakage in GaSb-based infrared detectors,” *Applied physics letters* **111**, 051102 (2017).
- [131] D. Liang, M. Fiorentino, T. Okumura, H.-H. Chang, D. T. Spencer, Y.-h. Kuo, A. W.-L. Fang, D. Dai, R. G. Beausoleil, and J. E. Bowers, “Electrically-pumped compact hybrid silicon microring lasers for optical interconnects,” *Optics Express* **17**, 20355–20364 (2009).
- [132] E. J. Stanton, A. Spott, M. L. Davenport, N. Volet, and J. E. Bowers, “Low-loss arrayed waveguide grating at 760nm,” *Optics Letters* **41**, 1785–1788 (2016).
- [133] J. F. Bauters, J. R. Adleman, M. J. R. Heck, and J. E. Bowers, “Design and characterization of arrayed waveguide gratings using ultra-low loss Si₃N₄ waveguides,” *Applied Physics A* **116**, 427–432 (2014).
- [134] E. J. Stanton, M. J. R. Heck, J. Bovington, A. Spott, and J. E. Bowers, “Multi-octave spectral beam combiner on ultra-broadband photonic integrated circuit platform,” *Optics Express* **23**, 11272–11283 (2015).
- [135] T. Y. Fan, “Laser Beam Combining for High-Power, High-Radiance Sources,” *IEEE Journal of Selected Topics in Quantum Electronics* **11**, 567–577 (2005).
- [136] E. J. Stanton, A. Spott, J. D. Peters, M. L. Davenport, N. Volet, A. Malik, J. Liu, C. D. Merritt, W. W. Bewley, I. Vurgaftman, C. S. Kim, J. R. Meyer, and J. E. Bowers, “Quantum cascade multi-spectral laser with integrated beam combiner on silicon,” in “Conference on Lasers and Electro-Optics,” (OSA, 2018), p. STh1B.7.
- [137] E. J. Stanton, A. Spott, J. D. Peters, M. L. Davenport, A. Malik, N. Volet, J. Liu, C. D. Merritt, W. W. Bewley, I. Vurgaftman, C. S. Kim, J. R. Meyer, and J. E. Bowers, “Multi-spectral quantum cascade lasers on silicon with integrated multiplexers,” *APL Photonics* **In Review** (2018).
- [138] C. C. Evans, A. Spott, C. D. Merritt, W. W. Bewley, I. Vurgaftman, C. S. Kim, J. R. Meyer, J. M. Hensley, J. E. Bowers, and M. B. Frish, “Gas Sensing Using Heterogeneously Integrated Quantum Cascade Lasers on Silicon,” in “Conference on Lasers and Electro-Optics,” (OSA, 2018), p. STu3N.1.